Electron and Lattice Response to Ultrafast Laser Excitation

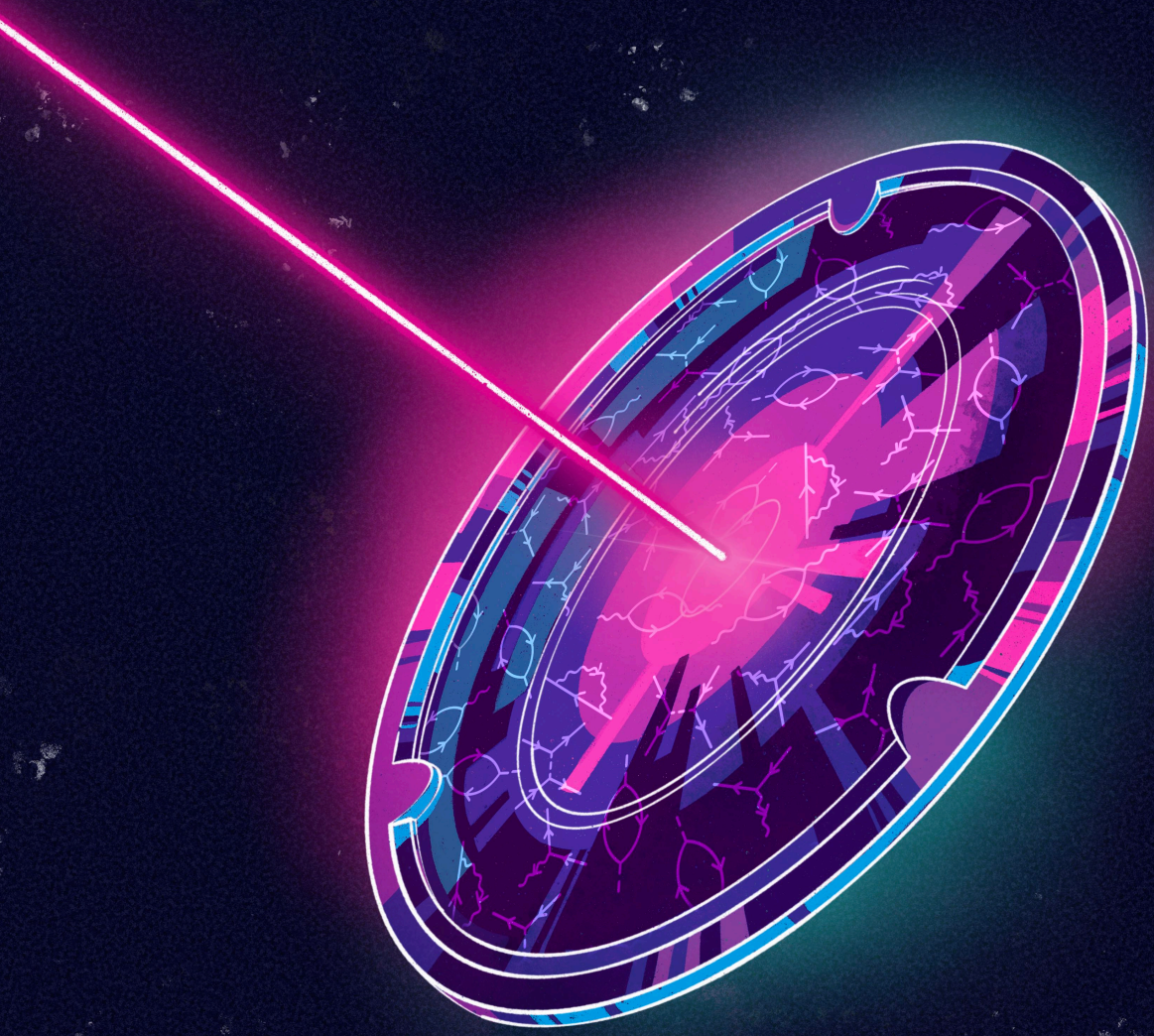

Fedor Akhmetov

Electron and lattice response to ultrafast laser excitation

Exploring temperature dynamics in transition metals

Fedor Olegovich Akhmetov

Electron and lattice response to ultrafast laser excitation

Exploring temperature dynamics in transition metals

DISSERTATION

to obtain
the degree of doctor at the University of Twente,
on the authority of the rector magnificus,
prof. dr. ir. A. Veldkamp,
on account of the decision of the Doctorate Board,
to be publicly defended
on Thursday 30 May 2024 at 16.45 hours

by

Fedor Olegovich Akhmetov

born on the 6^{th} of June 1996
in Kazan, Russia

This dissertation has been approved by:

Promotor	prof.dr. M.D. Ackermann
Co-promotors	dr.ir. I.A. Makhotkin dr. I. Milov

Acknowledgments:
The work described in this thesis was carried out in the Industrial Focus Group XUV Optics, MESA+ Institute for Nanotechnology, University of Twente, the Netherlands.
This work is part of the research program "X-tools – A thin film physics toolbox for XUV optics", funded by the Netherlands Organisation for Scientific Research NWO, with co-funding by ASML, Carl Zeiss SMT, and Malvern Panalytical (NWO Ref. No. 741.018.301).

UNIVERSITY OF TWENTE. | MESA+ INSTITUTE

ASML ZEISS Malvern Panalytical a spectris company

Cover design:	Cover art was designed by E. Etkeeva.
Printed by:	Ipskamp Printing
ISBN (print):	978-90-365-6128-0
ISBN (digital):	978-90-365-6129-7
DOI:	10.3990/1.9789036561297

Graduation Committee:

Chair / secretary:	Dean of the faculty S&T
Promotor:	prof.dr. M.D. Ackermann University of Twente, TNW
Co-promotors:	dr.ir. I.A. Makhotkin University of Twente, TNW
	dr. I. Milov University of Twente, TNW
Committee Members:	prof.dr. P.C.M. Planken University of Amsterdam
	prof.dr. J.L. Herek University of Twente, TNW
	prof.dr. C. Filippi University of Twente, TNW
	dr. G.H.L.A. Brocks University of Twente, TNW
	dr. V. Faramarzi ASML
	dr. J. Vorberger Helmholtz-Zentrum Dresden-Rossendorf e.V., Institute of Radiation Physics

List of Publications

This thesis is based on the following publications:

Chapter 2: F. Akhmetov, I. Milov, S. Semin, F. Formisano, N. Medvedev, J.M. Sturm, V.V. Zhakhovsky, I.A. Makhotkin, A. Kimel, and M. Ackermann, "Laser-induced electron dynamics and surface modification in ruthenium thin films", *Vacuum*, **212** (2023).

Chapter 3: F. Akhmetov, N. Medvedev, I.A. Makhotkin, M. Ackermann, and I. Milov, "Effect of Atomic-Temperature Dependence of the Electron–Phonon Coupling in Two-Temperature Model", *Materials*, **15**, 5193 (2022).

Chapter 4: F. Akhmetov, I. Milov, I. A. Makhotkin, M. Ackermann, and J. Vorberger, "Electron-phonon coupling in transition metals beyond Wang's approximation", *Physical Review B* **108**, 214301 (2023).

Chapter 5: F. Akhmetov, J. Vorberger, I. Milov, I. A. Makhotkin, and M. Ackermann, "*Ab initio*-simulated optical response of hot electrons in gold and ruthenium", *Optics Express* (2024).

Contents

1

Introduction

1

1.1 Ultrafast light – ultragreat physics

The 1980s were a truly remarkable decade. According to Wikipedia [1], they became an era of hip-hop, blockbusters, the first personal computers, and the end of the Cold War. Among these and many other unmentioned events, two stand out for their far-reaching consequences for fundamental and applied science. In 1985, Donna Strickland and Gérard Mourou developed a method of chirped pulse amplification (CPA) [2], allowing for the generation of high-power ultrashort laser pulses and creating a new field of femtosecond ($1\,\mathrm{fs} = 10^{-15}\,\mathrm{s}$) laser science. Just two years later, in 1987, Anne L'Huillier with co-workers observed that the interaction of short infrared pulses with argon atoms causes the high-harmonic generation (HHG) process [3], resulting in extreme ultraviolet (EUV) radiation with an even shorter few-hundred-attosecond ($1\,\mathrm{as} = 10^{-18}\,\mathrm{s}$) duration. Both of these discoveries were awarded the Nobel Prize in Physics: 2018 was the year of femtosecond lasers [4], whereas the just-passed 2023 became the year of attosecond physics [5].

These discoveries allowed physicists to push the boundaries of experimentally achievable temporal resolution to an unprecedented level. Almost immediately after the advent of CPA, the first femtosecond lasers provided a way to measure in real-time how atoms move in a single molecule [6] or how electrons in a solid are heated and transfer the heat to the lattice [7]. Way more time was required for attosecond HHG sources to become a real in-lab tool, but eventually, they were successfully used to "film" EUV-induced chemical reactions in molecules [8], or even the photoemission of single electrons from atoms [9] – a process people considered before as instantaneous.

Nowadays, ultrafast light sources have found applications in a wide range of fields. It is difficult to count all of them; we can only mention the notable ones. In manufacturing, high-power femtosecond lasers are often applied for 3D micro- and nanostructuring of device surfaces [10] or for pulsed laser deposition of thin films [11]. In medicine, pulsed lasers are used in laser surgery [12]. Ultrafast light sources are at the core of state-of-the-art metrology and imaging setups for the semiconductor industry [13, 14]; just recently, imec opened the Attolab facility aiming to characterize nanoscale features in Si wafers and photoresists.

Apart from various industrial applications, femto- and attosecond sources are routinely applied in pump-probe setups. In these setups, an ultrashort high-intensity pump pulse excites a particular degree of freedom (DOF) in a studied material (e.g. electrons, phonons, spins in correlated materials, excitons in insulators, etc.), followed by a weak probe pulse that measures the response of the excited DOF. By changing the delay between the pump and probe pulses, one can capture a movie of the time-resolved evolution of the excitation. The pump-probe technique allows for the study of fine effects, such as ultrafast magnetic switching in correlated materials [15], topological signatures in the band structure [16], as well as the response of extremely excited states of matter [17]. In the latter case, there is often interest in the temperature and structural dynamics of the studied material at ultrashort timescales to better understand the complex mixture of processes distributing energy over DOF within the material and out of it.

One of the simplest yet accurate approaches for studying the temperature dy-

namics in a solid target is through pump-probe transient optical response measurements. In this type of measurement, one registers the fraction of the probe pulse that is reflected, absorbed, or undergoes a change in polarization [18, 19]. The change in this fraction before and after the pump pulse income provides information on how optical constants change and, eventually, in what way the electronic and lattice DOF are excited. The main fundamental challenge arises at this point because one ultimately needs to know the dynamics of each DOF *separately*. However, the probed optical response is rather integral over *all* DOF. While their experimental disentanglement is virtually impossible (although Tobias Dornheim and co-workers [20] recently made a significant step in this direction by proposing an elegant way to extract temperature dynamics from dynamic structure factor measurements), a large effort has been put into the development of the finest models aiming to match the theoretically predicted dynamics of disentangled DOF with experimentally measured responses. Among them, first-principles quantum mechanical approaches provide high quantitative accuracy but are severely limited in spatial and temporal scales, whereas stochastic or continual methods without strict dimensional limitations strongly depend on the quality of input parameterization.

The research forming the basis of this thesis started with a rather applied question about the ultimate damage threshold of ruthenium (Ru) thin films under ultrafast laser irradiation. At that point, thanks to the extensive work conducted by Igor Milov [21], we considered the problem of ultrafast temperature dynamics in Ru to be greatly understood. We carried out a pump-probe experiment designed to measure both the dynamics and the onset of damage to find a correlation between them. During the analysis, we quickly realized that with the available knowledge, we had not been able to fully explain the observed dynamics or propose precise mechanisms of damage. Without such mechanisms, any attempts to predict damage would require an experimental confirmation at specific measurement conditions. To address this inconsistency, we needed to refine our understanding of the heating mechanisms potentially leading to further damage. Eventually, we moved deeper into the fundamentals of ultrafast light-metal interactions.

The present thesis explores the application of a combined first-principles and continual approach to describing the temperature dynamics in transition metals induced by femtosecond optical laser irradiation, with a special focus on Ru. In the pursuit of understanding the processes leading to measurable optical responses, it reveals limitations in *both* theoretical and experimental approaches to the problem. In a sense, it challenges the common perception of how electronic and lattice degrees of freedom evolve. In the following section, we outline the main models and assumptions applied throughout the work that helped us deepen our understanding of ultrafast light-metal interaction.

1.2 Modeling ultrafast light-metal interaction

Photons, quanta of electromagnetic radiation, across a wide range of energies, from visible light to hard X-rays, interact only with with electrons of matter. In most cases, this interaction involves the absorption of a photon by a target electron, causing immediate excitation from its ground state to one of the excited states.

The scattering with surrounding electrons or lattice vibrations (phonons) allows the excited electron to distribute the gained energy throughout the target, leading to its heating. When the timescale of light irradiation is larger than the characteristic times of electron-electron interactions (on the order of $\sim 1\,\mathrm{fs}$) and electron-phonon scattering (on the order of $\sim 1\,\mathrm{ps} = 10^3\,\mathrm{fs}$), processes of absorption, excitation, and relaxation occur simultaneously with pulse duration. As a result, one observes the material being heated. This scenario is common for any light sources, ranging from household light bulbs to nanosecond laser pulses.

The picture changes significantly when dealing with ultrafast light pulses. In this case, the entire light pulse is absorbed before excited electrons have time to scatter. This results in a high nonequilibrium state between excited and ground-state electrons, as well as between electrons and the lattice. To accurately describe this scenario, it is crucial to trace the dynamics of every separate electronic DOF. Perhaps the most accurate and parameter-independent method for this is time-dependent density functional theory (TD-DFT) [22], which allows for the description of the temporal evolution of single-particle quantum mechanical states with attosecond resolution and accounts for their interaction with each other in a mean-field sense. However, great capabilities usually come with great limitations: TD-DFT can handle systems of only several tens of atoms for a few hundred femtoseconds after excitation [23]. While this is typically sufficient for accurately simulating attosecond irradiation of single atoms, molecules, or small clusters, it is not suitable for femtosecond pulses and solid-state systems.

In this domain, methods based on kinetic theory have gained much popularity. The interaction of EUV and X-ray ultrafast irradiation with matter is successfully described by radiation transport Monte Carlo [24]—a stochastic formulation of the transport equation. By design, it samples binary collisions between classical point-like particles, neglecting many-body effects such as changes in electron energy levels due to electron excitation or collective excitations of quasiparticles. It usually accounts only for electron relaxation kinetics, while the lattice response is treated separately by means of molecular dynamics simulations. Additionally, the Monte Carlo approach is not capable of describing the interaction of laser pulses with wavelengths up to the deep ultraviolet range. In this regime, conduction band electrons absorb photons, merely exciting to higher-lying energy levels, and the assumption of fully ionized point-like charges traveling through a target is not valid.

Everything simplifies when considering a long-wavelength laser pulse with a width of $\sim 10 - 100\,\mathrm{fs}$. During the pulse duration, excited electrons have time to scatter with electrons in the ground state. It is convenient to assume that electron-electron scattering leads to the instantaneous relaxation of the electronic DOF to the equilibrium Fermi distribution at a high electron temperature, while the lattice remains cold until the first picosecond after pulse arrival [25]. Such a transient state of matter is referred to as a two-temperature state. The standard way to describe it is the two-temperature model (TTM), developed in a series of works initiated around 70 years ago [26, 27]. TTM assumes that electronic and lattice DOF are thermalized to equilibrium distributions, and the only weak nonequilibrium heat flow is governed by electron-electron (electron heat conduction) and electron-phonon scattering.

Mathematically, TTM is a set of two coupled heat equations describing the tem-

poral evolution of electron T_e and lattice T_l temperatures in response to external excitation:

$$\begin{aligned} C_e \partial_t T_e &= \nabla \left(\kappa_e \nabla T_e \right) - G_{e-ph}(T_e - T_l) + S, \\ C_l \partial_t T_l &= G_{e-ph}(T_e - T_l). \end{aligned} \tag{1.1}$$

In the first equation, C_e is an electron heat capacity, κ_e entering the gradient term is an electron heat conductivity, G_{e-ph} is an electron-phonon coupling allowing for energy exchange between electron and phonon heat baths, and S is an external laser source. In the second equation, C_l is a lattice heat capacity; the heat conduction term is neglected because in metals the lattice heat conduction is small compared to the electron one. In general, C_e, C_l, κ_e and G_{e-ph} are external parameters of TTM, and they are *a priori* unknown functions of both T_e and T_l, requiring derivation from microscopic considerations. While C_e and C_l are easily calculated from electron and phonon densities of states, the determination κ_e and G_{e-ph} requires the knowledge of momentum-dependent scattering rates. Practically, *ab initio* simulations are employed to acquire knowledge of accurate scattering rates. Thus, the predictive power of TTM is heavily dependent on the accuracy of the carried-out first-principles simulations.

While TTM can quantitatively describe temperature dynamics in light-metal interactions with proper parameterization, it remains unclear how to align its predictions with experimentally observed transient optical responses. Understanding how optical properties depend on transient T_e and T_l is crucial to translating TTM into measurements. At low pulse energies (and thus low temperatures), a linear relation between optical constants and TTM is often assumed, and the model is simply fitted to the measured signal. However, with arbitrarily high pulse energies, such a linear relation might not hold. An accurate model for optical constants in the two-temperature regime ($T_e > T_l$) is then needed, and once again, this falls within the scope of first-principles simulations. In the following section, we will briefly outline the underlying idea of such simulations.

1.3 Thermal density functional theory

Modeling precise temperature-dependent scattering rates, as well as optical properties of metals, from first principles requires detailed knowledge of how the electronic structure of a metal changes with electron and lattice temperatures. To acquire this knowledge, one must somehow solve the quantum many-body problem and obtain the many-particle wavefunction, which formally contains all information about the system. However, the exact solution to this problem is, in most cases, inaccessible. The first step in addressing this issue is to apply the Born-Oppenheimer approximation, allowing the uncoupling of lattice ions from the quantum mechanical description, treating them as classical particles surrounded by electrons instantly adjusted to ion positions. Nevertheless, even with the reduction to a many-electron quantum system, this problem still does not have an exact solution, and one needs to rely on approximated methods.

Arguably, the most popular and certainly the most developed method among those used for electronic structure calculation is density functional theory (DFT). The central idea of DFT is that the total energy of any many-particle quantum

1

system is solely defined by its particle density. DFT was originally developed by Hohenberg and Kohn in 1964 as a variational problem for ground state energy [28], and immediately extended by Mermin to statistical ensembles at finite temperatures [29]. Both ground-state and finite-temperature problems were translated by Kohn and Sham in 1965 into the language of a Schrödinger-like equation for non-interacting particles moving in a mean-field potential [30]. All many-body interaction effects are implicitly included in a so-called exchange-correlational potential – the difference between the exact many-particle energy and the energy of a single particle moving in an external electrostatic potential. In these formulations, DFT provides a convenient framework for the formally exact description of a many-body quantum system if one knows the exact exchange-correlational potential. In practice, such a potential is unknown, but existing approximated potentials provide highly accurate electronic structures.

The finite-temperature version of the Kohn-Sham equation is

$$\begin{aligned} \left(-\frac{1}{2}\nabla^2 + v_{KS}(\mathbf{r}) - \mu\right)|\phi_i\rangle &= \epsilon_i\,|\phi_i\rangle\,, \\ v_{KS}(\mathbf{r}) = v(\mathbf{r}) + \int \frac{n(\mathbf{r}')}{|\mathbf{r}-\mathbf{r}'|}d\mathbf{r}' &+ v_{xc}[n(\mathbf{r})], \\ n(\mathbf{r}) = \sum_i f(\epsilon_i - \mu)\,&\langle\phi_i|\phi_i\rangle\,, \end{aligned} \tag{1.2}$$

where $|\phi_i\rangle$ and ϵ_i are Kohn-Sham eigenstates and their eigenvalues, μ is the chemical potential of an ensemble, $v_{KS}(\mathbf{r})$ is an effective potential consisting of an interaction with lattice ions $v(\mathbf{r})$, mean-field electrostatic interaction with surrounding electrons, and the exchange-correlational potential $v_{xc}[n(\mathbf{r})]$ depending on the electron density $n(\mathbf{r})$. $f(\epsilon)$ is the Fermi distribution function controlling the temperature of the ensemble. Since the effective potential depends on eigenstates through the density, this equation has to be solved in a self-consistent manner, starting from some initial guess for single-particle wavefunctions.

The solution of the Kohn-Sham equation provides access to $|\phi_i\rangle$ and ϵ_i at any finite electron temperature. While DFT solves the many-electron problem, the inclusion of lattice temperature is typically achieved through the molecular dynamics evolution of ion positions, altering the potential $v(\mathbf{r})$ in Eq. (1.2). Furthermore, the linear response theory and many-body perturbation theory come into play. The linear response theory calculates temperature-dependent optical properties on top of Kohn-Sham states, while perturbation theory provides scattering rates through the evaluation of a particle self-energy. The description of these two methods, as well as their application to hot electrons in transition metals, is covered in Chapters 4 and 5.

1.4 Structure of this thesis

The structure of this thesis follows the evolution of the Author's perception of the fundamental phenomena behind ultrafast light-metal interaction. While the first chapters utilize relatively simple concepts to establish a principal understanding

of observable dynamics, the later chapters explore distinct aspects of light-metal interaction at a full *ab initio* microscopic level.

Chapter 2 describes the optical pump-probe experiment with Ru thin films, aiming to measure heat dynamics as well as the onset of surface damage. A thorough *post mortem* analysis of surface morphology was performed, revealing that heat-induced surface cracking is responsible for the damage. On the theoretical side, the combination of TTM with molecular dynamics was applied to explain the observed damage. Although it could not reproduce the measured damage thresholds due to their essentially multishot nature, it allowed us to associate surface cracking with heat-induced tensile stress waves propagating in a film and accumulating on the defect boundaries. This chapter is pivotal for the thesis. Aiming to unravel the temperature evolution encoded into the measured pump-probe signal, in further chapters, we developed a fine parameterization for Ru in a two-temperature regime.

Chapter 3 covers the first attempt to understand how the electron-phonon coupling parameter affects the measured heating dynamics in Chapter 2. It studies the role of lattice temperature dependence of the electron-phonon coupling in the TTM framework with respect to initial excitation. It was found that in the considered cases of transition metals, stronger excitation leads to faster electron-lattice thermalization. The lattice temperature dependence significantly boosts the relaxation speed, resulting in sub-picosecond thermalization at certain initial conditions.

Chapter 4 focuses on the fundamentals of electron-phonon interaction in transition metals, which occurs immediately after femtosecond heating of electrons. Utilizing state-of-the-art DFT simulations of the electron-phonon spectral function in ruthenium, palladium, and gold, it demonstrates that the electron-phonon coupling at high electron temperatures is significantly dependent on the specific electron state—a factor often overlooked in the light-matter interaction community. The refined model for electron-phonon coupling in Ru developed here is subsequently implemented in TTM in the next chapter, representing a new attempt to understand the mechanisms of temperature evolution in ruthenium thin films.

Chapter 5 explores the optical response of a heated electron system in gold and ruthenium to an external electromagnetic field using DFT simulations. First, it discusses the importance of different scattering mechanisms in describing the long-wavelength regime relevant for optical laser irradiation. Second, it provides optical constants of Ru at elevated electron temperatures. This step allows us to map simulated two-temperature dynamics to the pump-probe signal measured in Chapter 2. At this point, we have achieved a fundamental understanding of the mechanisms of ultrafast heating in Ru, which diverges from the preconditions and expectations set before the experiment was designed. It turns out that, due to a very strong electron-phonon coupling, the observed dynamics are best described by equilibrium temperature evolution. However, additional experiments and first-principles simulations are required to confirm our findings.

1

References

[1] *1980s – Wikipedia, The Free Encyclopedia,* https://en.wikipedia.org/wiki/1980s.

[2] D. Strickland and G. Mourou, *Compression of amplified chirped optical pulses,* Optics Communications **55**, 447 (1985).

[3] M. Ferray, A. L'Huillier, X. F. Li, L. A. Lompre, G. Mainfray, and C. Manus, *Multiple-harmonic conversion of 1064 nm radiation in rare gases,* Journal of Physics B: Atomic, Molecular and Optical Physics **21** (1988), 10.1088/0953-4075/21/3/001.

[4] *The Nobel Prize in Physics 2018 – NobelPrize.org,* https://www.nobelprize.org/prizes/physics/2018/summary.

[5] *The Nobel Prize in Physics 2023 – NobelPrize.org,* https://www.nobelprize.org/prizes/physics/2023/summary.

[6] A. H. Zewail, *Laser Femtochemistry,* Science **242**, 1645 (1988).

[7] D. von der Linde, K. Sokolowski-Tinten, and J. Bialkowski, *Laser–solid interaction in the femtosecond time regime,* Applied Surface Science **109-110**, 1 (1997).

[8] M. Lara-Astiaso, M. Galli, A. Trabattoni, A. Palacios, D. Ayuso, F. Frassetto, L. Poletto, S. De Camillis, J. Greenwood, P. Decleva, I. Tavernelli, F. Calegari, M. Nisoli, and F. Martín, *Attosecond Pump-Probe Spectroscopy of Charge Dynamics in Tryptophan,* Journal of Physical Chemistry Letters **9**, 4570 (2018).

[9] P. Eckle, A. N. Pfeiffer, C. Cirelli, A. Staudte, R. Dörner, H. G. Muller, M. Büttiker, and U. Keller, *Attosecond ionization and tunneling delay time measurements in helium,* Science **322**, 1525 (2008).

[10] R. R. Gattass and E. Mazur, *Femtosecond laser micromachining in transparent materials,* Nature Photonics **2**, 219 (2008).

[11] D. H. Lowndes, D. B. Geohegan, A. A. Puretzky, D. P. Norton, and C. M. Rouleau, *Synthesis of Novel Thin-Film Materials by Pulsed Laser Deposition,* Science **273**, 898 (1996).

[12] S. H. Chung and E. Mazur, *Surgical applications of femtosecond lasers,* (2009).

[13] J. S. Oh and S.-W. Kim, *Femtosecond laser pulses for surface-profile metrology,* Optics Letters **30**, 2650 (2005).

[14] R. Manser, *EUV Microscopy: A Unique Approach for Materials Characterization,* PhotonicsViews **16**, 42 (2019).

[15] A. Kirilyuk, A. V. Kimel, and T. Rasing, *Ultrafast optical manipulation of magnetic order,* Reviews of Modern Physics **82**, 2731 (2010).

[16] H. Ito, Y. Otaki, Y. Tomohiro, Y. Ishida, R. Akiyama, A. Kimura, S. Shin, and S. Kuroda, *Observation of unoccupied states of SnTe(111) using pump-probe ARPES measurement,* Physical Review Research **2**, 1 (2020).

[17] L. B. Fletcher, H. J. Lee, T. Döppner, E. Galtier, B. Nagler, P. Heimann, C. Fortmann, S. LePape, T. Ma, M. Millot, A. Pak, D. Turnbull, D. A. Chapman, D. O. Gericke, J. Vorberger, T. White, G. Gregori, M. Wei, B. Barbrel, R. W. Falcone, C. C. Kao, H. Nuhn, J. Welch, U. Zastrau, P. Neumayer, J. B. Hastings, and S. H. Glenzer, *Ultrabright X-ray laser scattering for dynamic warm dense matter physics,* Nature Photonics **9**, 274 (2015).

[18] M. Maiuri, M. Garavelli, and G. Cerullo, *Ultrafast Spectroscopy: State of the Art and Open Challenges,* Journal of the American Chemical Society **142**, 3 (2020).

[19] Y. Zhang, J. Dai, X. Zhong, D. Zhang, G. Zhong, and J. Li, *Probing Ultrafast Dynamics of Ferroelectrics by Time-Resolved Pump-Probe Spectroscopy,* (2021).

[20] T. Dornheim, M. Böhme, D. Kraus, T. Döppner, T. R. Preston, Z. A. Moldabekov, and J. Vorberger, *Accurate temperature diagnostics for matter under extreme conditions,* Nature Communications **13**, 1 (2022).

[21] I. Milov, *Damage processes in ruthenium thin films induced by ultrashort laser pulses*, Ph.D. thesis, University of Twente (2020).

[22] E. Runge and E. K. U. Gross, *Density-Functional Theory for Time-Dependent Systems,* Physical Review Letters **52**, 997 (1984).

[23] J. Lloyd-Hughes, P. M. Oppeneer, T. Pereira Dos Santos, A. Schleife, S. Meng, M. A. Sentef, M. Ruggenthaler, A. Rubio, I. Radu, M. Murnane, X. Shi, H. Kapteyn, B. Stadtmüller, K. M. Dani, F. H. Da Jornada, E. Prinz, M. Aeschlimann, R. L. Milot, M. Burdanova, J. Boland, T. Cocker, and F. Hegmann, *The 2021 ultrafast spectroscopic probes of condensed matter roadmap,* Journal of Physics Condensed Matter **33** (2021), 10.1088/1361-648X/abfe21.

[24] B. Ziaja and N. Medvedev, *Modelling ultrafast transitions within laser-irradiated solids,* (2012).

[25] B. Rethfeld, K. Sokolowski-Tinten, D. Von Der Linde, and S. I. Anisimov, *Timescales in the response of materials to femtosecond laser excitation,* Applied Physics A: Materials Science and Processing **79**, 767 (2004).

[26] M. I. Kaganov, I. M. Lifshitz, and L. V. Tanatarov, *Relaxation between electrons and crystalline lattice,* Sov. Phys. JETP **4**, 173 (1957).

[27] S. Anisimov, B. Kapeliovich, and T. Perel-man, *Electron emission from metal surfaces exposed to ultrashort laser pulses,* Journal of Experimental and Theoretical Physics (1974).

[28] P. Hohenberg and W. Kohn, *Inhomogeneous Electron Gas,* Physical Review **136**, B864 (1964).

[29] N. D. Mermin, *Thermal Properties of the Inhomogeneous Electron Gas,* Physical Review **137**, A1441 (1965).

[30] W. Kohn and L. J. Sham, *Self-consistent equations including exchange and correlation effects,* Physical Review **140** (1965), 10.1103/PhysRev.140.A1133.

2

Laser-induced electron dynamics and surface modification in ruthenium thin films

We performed the experimental and theoretical study of the heating and damaging of ruthenium thin films induced by femtosecond laser irradiation. We present the results of an optical pump-probe thermoreflectance experiment with rotating sample allowing to significantly reduce heat accumulation in irradiated spot. We show the evolution of surface morphology from growth of a heat-induced oxide layer at low and intermediate laser fluences to cracking and grooving at high fluences. Theoretical analysis of thermoreflectance in our pump-probe experiment allows us to relate behavior of hot electrons in ruthenium to the Fermi smearing mechanism. This conclusion invites more research on Fermi smearing of transition metals. The analysis of heating is performed with the two-temperature modeling and molecular dynamics simulation, results of which demonstrate that the calculated single-shot melting threshold is higher than experimental damage threshold. We suggest that the onset of Ru film damage is caused by the heat-induced stresses that lead to cracking of the Ru film. Such damage accumulates during repetitive exposure to light.

2.1 Introduction

2

Ultrashort lasers have become versatile tools for the manipulation of material properties at the nanoscale. The unique ability of such lasers to deliver an enormous amount of energy into a sample on a femtosecond timescale creates extreme strongly non-equilibrium states which upon relaxation lead to altered material properties. Ultrashort lasers are used for surface nanostructuring [1] and nanofabrication [2–4], as well as for reversible switching of material structure between crystal and amorphous phases for applications in data storage [5]. Alternatively to these high-intensity laser applications, ultrashort lasers with relatively low intensity are used in various metrology and probing techniques [6–8]. In this context, contrary to the previous examples, laser-induced damage must be avoided. In both scenarios of desired and undesired material modifications, precise control of the output of laser-matter interaction is crucial, and can only be achieved with a deep understanding of the fundamental physical processes involved. This work aims at such understanding on an example of ruthenium (Ru) thin films exposed to optical femtosecond laser pulses.

Ru and Ru oxides are indispensable materials for various catalysis applications [9, 10]. Controlling the surface properties of Ru such as oxidation state, as well as the shape and structure of Ru nanocrystals, provides additional efficient functionalities [11]. Ultrathin films of Ru are used as protective capping layers in extreme ultraviolet optics, due to high transmissivity in EUV range and low surface oxidation [12]. Ru is also considered as a high Z material for grazing incidence hard X-ray optics [13].

In our previous studies, we focused on severe damage of Ru thin films at high vacuum conditions in single- [14–16] and multi-shot regimes [17], as well as on long-term exposure of Ru at fluences significantly below the single-shot ablation threshold [18]. Such sub-threshold investigation of material degradation is challenging since the processes involved are elusive to be detected *post mortem*. Dynamical data must be collected to provide insights into how laser-induced evolution of Ru results in the final damage. Therefore, in this work, we continue investigating Ru interaction with ultrashort laser pulses in an all-optical pump-probe scheme with rotating samples to reduce heat accumulation effects. The analysis of measured in pump-probe experiment thermoreflectance data aimed to find a connection between optical response and light-induced damage of a film.

The character of damage may depend on certain environmental conditions. For example, the single- and multi-pulse damage thresholds of optical coatings may alter depending whether the experiments are carried out at vacuum or ambient conditions [19]. The presence of oxygen in the environment enhances the darkening of a metal surface during the ultrafast laser ablation [20]. The influence of environment on surface nanopattering does not demonstrate any systematic behavior. In some experimental configurations, the pressure of gas plays a major role whereas the chemical altering of surface has minor impact [21]. In others, the chemical composition of gas determines the morphology of nanostructures [22].

We performed present experiment under ambient conditions. After the irradiation, Ru surfaces are examined with various surface-sensitive characterization

techniques, namely Atomic Force Microscopy (AFM), Auger- and X-ray photoelectron spectroscopies (AES and XPS) and Scanning Electron Microscopy (SEM). Determination of Ru thin film damage threshold was based on a SEM analysis of exposed samples. The analysis of pristine and irradiated surface revealed only a minor effect of environment on detected damage. This indicates that at given irradiation parameters similar character of damage can be expected under vacuum conditions.

To interpret pump-probe data we perform theoretical analysis of Ru optical response to ultrashort laser irradiation. When an ultrafast laser pulse illuminates a metallic target, its energy is absorbed by the conduction band electrons, which leads to the evolution of initially equilibrium electron distribution to a non-equilibrium one. It is often assumed that the thermalization of an electron gas to an equilibrium Fermi distribution occurs on a timescale of ~ 100 fs, which is comparable to our pulse duration [23–26]. Thus, it is convenient to consider the probed optical response of a metallic target in terms of the electron temperature T_e elevated with respect to the lattice one T_l. However, a reliable model for T_e-dependent optical constants is required for direct analysis of optical pump-probe experiments. The widely used Drude model is limited in applicability to the case of simple metals [27]. In the case of noble metals, the optical response can be successfully described by Fermi smearing mechanism, assuming that change of reflection signal is proportional to the derivative of the Fermi distribution with respect to the electron temperature [28–30].

In contrast, in a transition metal with a complex band structure such as Ru, the optical constants are formed by a sum of *inter-* and *intraband* contributions within a combined d-s/p conduction band and to date could not be reasonably approximated with a simple analytical model. Instead, T_e-dependence may be extracted from first-principles simulations of the complex dielectric function of a material in, e.g., random-phase approximation (RPA) [31–34]. However, such simulations are computationally heavy.

We test to what extent a simple Fermi smearing analysis can be applied to Ru. We also model the absorption of the laser energy by the electrons and coupling of electrons to the lattice with the two-temperature model (TTM) and with a combination of the TTM with classical molecular dynamics. The calculated single-shot melting threshold is compared with the experimental surface modification observations.

2.2 Experimental setup

For the pump-probe thermoreflectance experiments, we employed pump-probe setup based on ultrafast 1 kHz repetition rate Ti:Sapphire laser, Fig. 2.1. The experiment was carried out under atmospheric conditions. The angles of incidence (AOI) were set close to normal ($\sim 5 \pm 2^\circ$ and $\sim 8 \pm 2^\circ$ off-sample normal for pump and probe pulses, respectively). The beam profile was characterized by a knife-edge method along the horizontal direction. Additional *post mortem* analysis of Ru ablation craters revealed an ellipticity of a Gaussian profile which is not associated with a small off-normal AOI only. The value of the semi-major axis was $\sim 115\,\mu$m

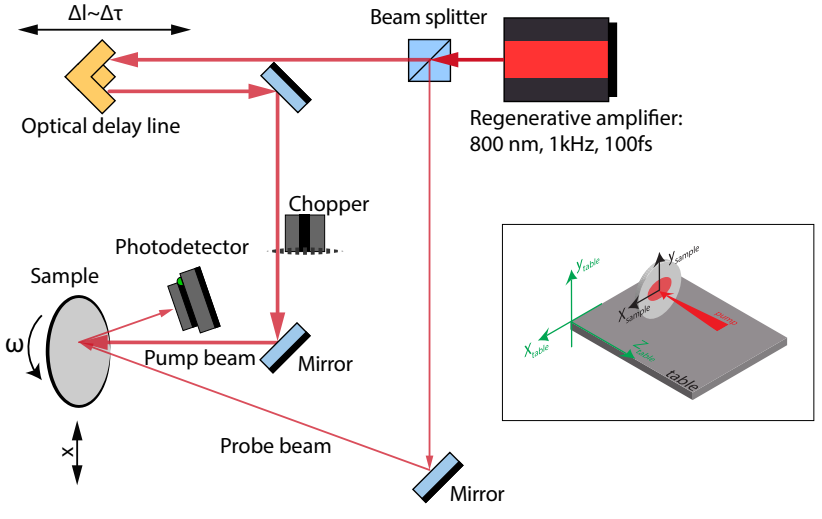

Figure 2.1: Scheme of experimental set-up used for optical pump-probe thermoreflectance measurements. The laser beam coming out of regenerative amplifier (Spitfire), which generates the near transform-limited 100 fs FWHM pulses with 800 nm wavelength ($\hbar\omega = 1.55\,\mathrm{eV}$) and 1 kHz repetition rate. Laser beam is split into a high-intensity pump and a low-intensity probe pulses. The pump pulse is chopped to a 500 Hz repetition rate. The probe pulse at 1 kHz arrives to the sample with a time delay controlled with an optical delay line to measure the reflection change induced by the pump pulse. Inset: configuration of polarisation of incident beams and convention on axes.

(@ $1/e^2$) whereas the value of the semi-minor axis was 1.4 times smaller. The peak incident fluence was calculated as follows:

$$F = \frac{2E_{pulse}}{\pi w_x w_y} \tag{2.1}$$

Here E_{pulse} is an energy value of pump pulse, w_x and w_y are values of semi-major and semi-minor axes of ellipse, respectively. The sample was positioned slightly before the focal spot to avoid air ionization and consequent aberration of the beam quality at the sample. To continuously control the laser fluence we used an attenuator consisting of a half-wave plate and a polarizer located in the pump path. We characterized the laser pulse duration by placing an autocorrelator just before the sample with typical measured values to be $\sim$ 85 fs (FWHM). P- and s-polarizations with respect to the optical bench were used for the pump and the probe pulse, respectively.

As a studied material, we used ruthenium (Ru) polycrystalline thin metal film. The Ru films of various thickness between 17 and 125 nm were deposited by magnetron sputtering on top of (100) single-crystal Si wafers with 3-inch diameter. Ru thickness was measured using X-ray reflectometry. To reduce the effect of heat accumulation, samples were mounted on a rotational stage. The rotational frequency was set to $\omega = 90\,\mathrm{Hz}$. Such a scheme ensured an effective reduction of the

repetition rate, without changes of the laser source. However, after several rotations laser pulses start hitting previously exposed surface, therefore accumulation of irreversible changes induced by pump pulses is expected at high pump fluences. For each sample we measured transient thermoreflectance change induced by pump pulses of various fluences. For each fluence value a different position on a sample was measured. For every sample, the measurements were carried out at distances in the range of 17–32 mm from a sample center. Since the position variation was small compared to the radius at which the set of measurements was performed, a slightly different level of accumulation of irreversible changes for different fluences within each sample can be neglected.

Before the actual measurement of thermoreflectance curve, several pump and probe pulses arrive to the sample surface at negative delays between the pump and the probe resulting in a weak signal. We have a pronounced step in this signal at negative delays from -20 to 0 ps (see Fig. 2.2(a)). We explain it by a partial split of the probe signal in the beamsplitter leading to a delay between the main fraction of probe and a small trailing probe. The latter overlaps with the retarding pump pulse and delivers a small signal to the photo-detector. Analyzing thermoreflectance data, we aligned the signal to the values taken from delays $t < -20\,\mathrm{ps}$.

2.3 Experimental results

2.3.1 Fluence-dependent transient thermoreflectance

A set of pump-probe transient thermoreflectance data for a 37 nm thick Ru film is shown in Fig. 2.2(a). It demonstrates that in all measured curves the reflected probe intensity sharply increases during the first few ps resulting in a pronounced peak followed by slow decay. The very sharp increase at < 1 ps timescales is primarily associated with the increase of the electron temperature induced by the absorbed pump pulse. At $\sim 1 - 3$ ps timescale, a slower signal increase can be attributed to the coupling of the electrons to the lattice and thereby induced lattice heating. A slow decay over tens of picoseconds corresponds to heat diffusion from the surface region deeper into the sample [35]. This is confirmed by the TTM simulations of the surface electron and lattice temperatures shown in Fig. 2.2(b).

At high pump pulse fluences above $\sim 50\,\mathrm{mJ/cm^2}$ we observe qualitatively different behavior of $\Delta R/R_0$ signal at $\Delta t > 20\,\mathrm{ps}$ time delay compared to lower fluences. We see the change of trend from a slow decay to an increase. For every thickness, we were able to extract the time when the signal starts to increase by calculating the time derivative of a signal using a regularization algorithm for noisy signals [36]. We determined the time and fluence values when a derivative of a signal changes its sign from negative to positive, and report them in Table 2.1. For 17 nm Ru film, we could not extract any values, because the pump-probe curves exhibit strong oscillations for high fluence values. For 125 nm Ru film, we did not observe an increase of the signal within the fluence and time delay ranges considered, and thus put the highest measured fluence into the table. We use these data later in Section 2.4.3 when discussing the thickness-dependent damage threshold in Ru.

The measured data in Fig. 2.2(b) show that the peak thermoreflectance change

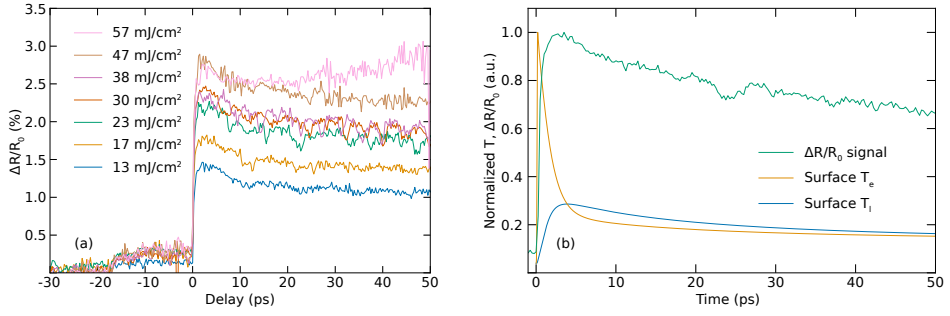

Figure 2.2: (a) Transient changes of reflectance of a 37 nm Ru film measured for various incident fluences. (b) Normalized pump-probe thermoflectance signal (green) compared with normalized profiles of electron (orange) and lattice (blue) temperatures.

Thickness (nm)	Incident fluence (mJ/cm^2)	Absorbed fluence (mJ/cm^2)	Delay (ps)
17	-	-	-
30	51.2 ± 3.8	14.1 ± 1.0	25.5
37	54.6 ± 4.0	16.7 ± 1.2	36.0
50	60.9 ± 4.5	21.7 ± 1.6	21.5
75	67.2 ± 4.9	25.9 ± 1.9	21.8
125	77.0 ± 5.7	29.9 ± 2.2	-

Table 2.1: Measured fluence and time delay values related to change of signal trend from slow decay to sharp increase at high fluence.

reached at ~ 3ps for each curve increases with the fluence and saturates at a certain fluence value. Similar sets of pump-probe thermoreflectance curves were obtained for various thicknesses of Ru films. The overview of measured data for all film thicknesses is reported in the supplementary materials.

In Fig. 2.3 we provide the peak values of $\Delta R/R_0$ as a function of the pump fluence for three different thicknesses of Ru corresponding to three absorption regimes (see more details in Fig. 2.4). The optical penetration depth in Ru for 800 nm light is 16 nm. Therefore, for 17 nm film, multiple reflections of absorbed light at a Ru-Si and Ru-air interfaces change the absorption profile considerably compared to the Lambert-Beer law. For 37 nm, deviations from the Lambert-Beer profile are visible but not dramatic, whereas 125 nm film optically behaves like a bulk material, see Fig. 2.4. We see that with increasing fluence the peak of reflectance linearly increases and saturates at a particular value for each Ru thickness.

In the case of 37 nm Ru, we see a jump in the peak values of thermoreflectance around 45 mJ/cm^2. The further analysis does not reveal any sharp changes at this fluence, and such a jump is not present in the data obtained from other samples, the peak reflectance changes continuously. Therefore, we consider it to be a measurement artefact. In the case of 125 nm Ru, we observe a drop of reflectance peak at the highest fluences. We also detected a similar drop at another thickness,

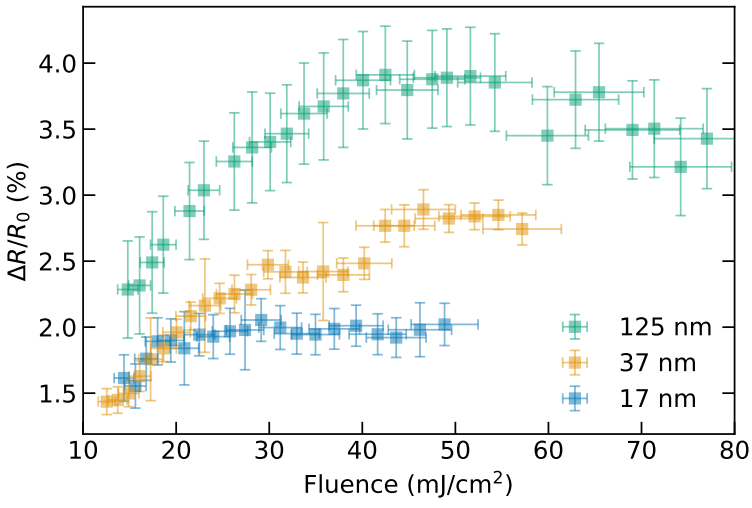

Figure 2.3: Peak values of thermoreflectance change as a function of pump fluence for 17 nm, 37 nm, and 125 nm Ru films.

75 nm. We attribute these drops to strong accumulated damage of a film at high fluences. This is confirmed by SEM observations presented in Section 2.3.2, where we observed strong damage of sample surfaces at high fluences.

2.3.2 Analysis of the surface morphology.

Since the experiment is carried out with rotation of samples, having rotation frequency and laser repetition rate unsynchronized, the pump laser generates not individual spots, but almost continuous lines. Every line corresponds to a particular laser fluence, so we can easily trace possible morphology changes caused by the pump using *post mortem* SEM analysis.

In Fig. 2.5 we show SEM images of a 37 nm thick Ru film surface after laser exposure. Fig. 2.5(a) shows the overview SEM image of exposed lines. The line 1 corresponds to the highest peak fluence of 57 mJ/cm^2, the last visible line (line 10) corresponds to the peak fluence of 36 mJ/cm^2). Note that before actual damage of the surface, several lines look darker compared to unexposed area. In Fig. 2.5(b) we show the magnified view of line 4 (peak fluence is 49 mJ/cm^2). At those irradiation conditions, SEM was not able to resolve any morphological changes of the surface. Starting from line 3 we see a clear indication of damage: the film is covered with cracks (Fig. 2.5(c)). Further increase of the peak fluence leads to severe damage of the surface having a shape of periodic grooves, see Fig. 2.5(d).

To investigate in more details the onset of damage, we also performed cross-sectional SEM scans of cracked area, see Fig. 2.6. They revealed that the cracks are formed over the entire film depth. We will discuss possible mechanisms of crack formation below in Section 2.4.3.

For the analysis of a dark region on line 4, we performed an additional com-

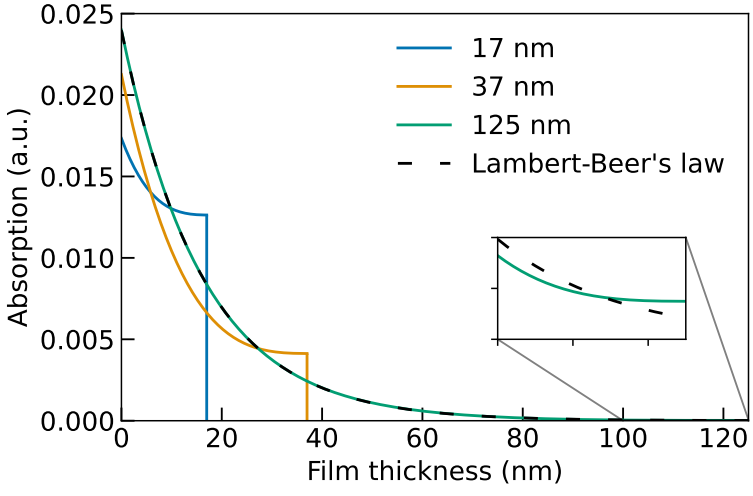

Figure 2.4: Absorbed energy density profiles for Ru films of 17, 37, and 125 nm thicknesses on Si substrates calculated with the transfer-matrix approach [37]. Inset: deviation of transfer-matrix from Lambert-Beer profile at Ru-Si interface.

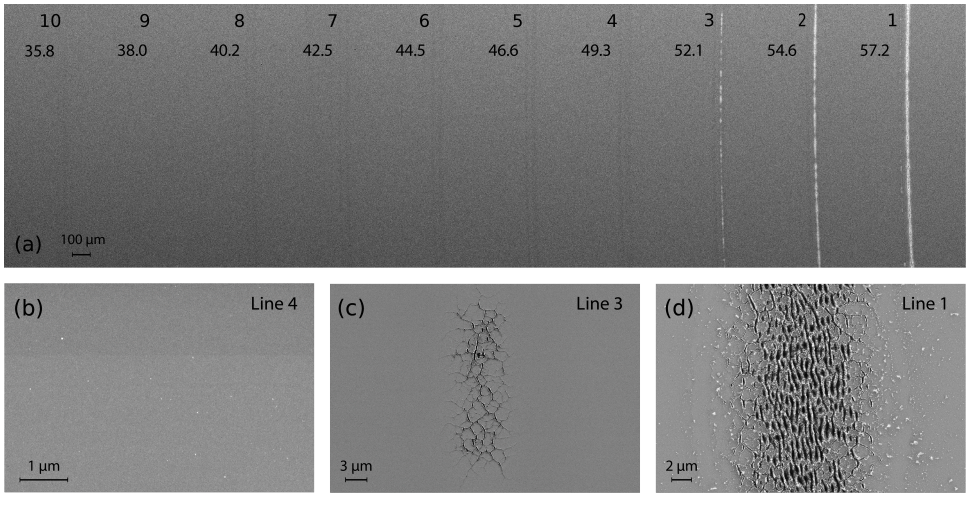

Figure 2.5: (a) SEM image of a 37 nm thick Ru surface after laser irradiation. Numbered lines correspond to irradiation conditions ranging from the regime of intermediate fluences (lines 10-4, darkening along irradiation path) to high (lines 3-1, the surface is damaged), and the values below the line numbers are pulse fluences in $\mathrm{mJ/cm^2}$. (b) Zoomed-in SEM image of line 4, no surface damage is present. (c) The same for line 3. The line consists of separate spots of cracks along the irradiation path. (d) The same for line 1. Damage morphology is represented by continuous grooves along the irradiation path.

bination of Auger electron spectroscopy (AES), X-ray photoelectron spectroscopy (XPS), and atomic force microscopy (AFM) characterization techniques. AES indi-

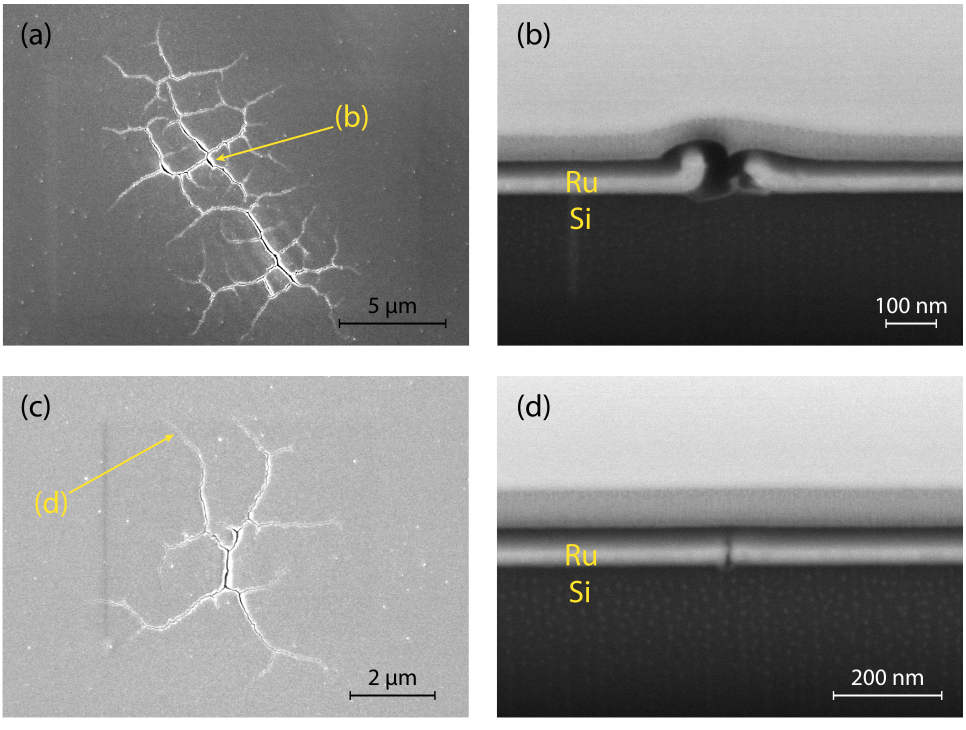

Figure 2.6: (a) SEM image of a separate crack spot found at irradiated line 4, see Fig. 2.5 (a). Yellow line indicates intense crack which depth was measured by FIB-SEM technique. (b) FIB-SEM image of the crack. The crack depth is equal to the entire film thickness. (c) SEM image similar to (a), but for a smaller crack spot. Yellow line indicates the edge of the crack characterized by FIB-SEM. (d) FIB-SEM image of the crack edge. The crack formation along the entire film thickness can be seen.

cated ~ 2 times increase of oxygen concentration on the dark regions, compared to the reference area outside the exposure zones. A more detailed measurement of the oxide thickness done with angle-resolved XPS indicated only 0.4 nm growth of the oxide layer above the thickness of a native oxide of 0.8 nm. Such a small increase of oxygen content after irradiation at relatively high incident fluence means that the oxidation is not responsible for film damage. Under given irradiation parameters, one can expect similar behavior at vacuum conditions.

The AFM indicated ~ 1.5 times increased RMS roughness in these exposed areas from 0.187 nm to 0.280 nm. It is unlikely that such small structural changes can explain the formation of dark lines on the SEM image. We can assume possible light-induced carbon growth that could explain such darkening. However, the growth of small amounts of C on Ru cannot be reliably quantified by AES and XPS, because carbon and ruthenium emission spectra overlap on Auger electron/X-ray photo-emission spectra. The XPS spectra in the exposed spot showed an increase of the intensity at the energy of the $\mathrm{Ru3d}_{3/2}$ peak relative to the $\mathrm{Ru3d}_{5/2}$ intensity (compared to outside the exposed area). This is a qualitative indication of increased

carbon content, but the difference compared to the unexposed area is too small for a reliable quantification by peak fitting. Detailed description of XPS analysis is provided in Section 2.6.

We can claim that the darkening of an irradiated path is a result of heat-induced surface chemistry. We found that the darkening is a result of a minor increase of the oxide thickness as well as slight carbonization. However, we could not resolve the exact stoichiometry of the compound since the carbon signal was too weak to quantify.

2.4 Theoretical analysis

2.4.1 Two-temperature modeling

For the analysis of laser-induced ultrafast heating and melting of Ru thin films, we applied the two-temperature model (TTM) [38]. The TTM equations that govern heat dynamics of electron and lattice subsystems are:

$$\begin{cases} C_e(T_e)\frac{\partial T_e}{\partial t} = \frac{\partial}{\partial z}\left(k_e(T_e,T_l)\frac{\partial T_e}{\partial z}\right) - G(T_e,T_l)(T_e - T_l) + S(t,z), \\ (C_l(T_l) + H_m\delta(T_l - T_m))\,\frac{\partial T_l}{\partial t} = G(T_e,T_l)(T_e - T_l) \end{cases} \tag{2.2}$$

Here T, C and k are the temperature, heat capacity and thermal conductivity of Ru electrons (subscript e) and lattice (subscript l), respectively; G is the temperature-dependent electron-phonon coupling factor, and S is the heat source representing a laser pulse. Lattice thermal conductivity is considered to be negligible compared to the electron one. The electron heat capacity and electron-phonon coupling were taken from XTANT simulations based on the non-adiabatic tight-binding molecular dynamics approach [39]. The electron thermal conductivity $k_e(T_e, T_l)$ was taken from *ab initio* calculations [40], and that is the most accurate data available to the best of our knowledge.

To account for solid-liquid phase transition at the melting temperature T_m, we used an effective lattice heat capacity containing a delta-function term corresponding to the latent heat of fusion H_m, as was initially proposed in [41] for ns-laser heating, and latter extended in [42] to TTM approach and fs pulses. The melting threshold was considered to be reached when at least one computational cell came to a liquid state ($T_l > T_m$).

The heat source $S(t,z)$ is a product of a temporal Gaussian pulse and in-depth absorbed energy profile as follows:

$$S(t,z) = F\sqrt{\frac{4\ln 2}{\pi\tau_p^2}}e^{-4\ln 2(t/\tau_p)^2}A(z) \tag{2.3}$$

Here F is an incident fluence, τ_p is a pulse duration, and $A(z)$ is an absorbed energy profile. For bulk materials and films much thicker than the photons absorption length, $A(z)$ can be described by the Lambert-Beer absorption law. However, in the case of multilayer structures and thin films with the thickness comparable to the absorption length of photons, Lambert-Beer law breaks down (see Fig. 2.4). To account for the deviations of the absorption profile from the Lambert-Beer's law in

the heat source, in our code we implemented the matrix algorithm (transfer-matrix approach) for the fields calculation [37].

2.4.2 Fermi smearing mechanism in Ru

To relate experimentally measured change of thermoreflectance signal $\Delta R(t)/R_0$ and TTM-calculated temperatures $T_e(t)$, $T_l(t)$, one needs to know how optical constants depend on temperatures in two-temperature regime. T_l-dependence of optical properties is often neglected as far as heating of lattice subsystem does not cause any significant changes in electronic structure. In this work, we assume that the transient optical response of the electron system in Ru can be described in terms of the electron temperature T_e, same as in other transition metals [35, 43]. However, finding an approximate form of T_e-dependence of Ru optical constants is a challenging task. Due to the complexity of Ru band structure near the Fermi level, a simple but widely accepted Drude model would not provide reliable results, whereas accurate DFT-based optical constants would require a set of computationally heavy calculations. Nevertheless, some qualitative information about optical response in Ru can be obtained if one recognizes a similarity in band structures of Ru and gold in the vicinity of the Fermi level.

We noticed that the electron density of states (DOS) of Ru (Fig. 2.7 (a)) has a pseudo-gap near the Fermi level ranging from -1.5 to 1 eV, similarly to the gap between the majority of the d-band and the Fermi level in gold (Fig. 2.7 (b)). As was pointed out in [44], for photon energies within this pseudo-gap area, the interband contribution to the optical transitions is weak, and at a qualitative level, a temperature dependence of the reflectance change in Ru may be explained via the Fermi smearing mechanism like in noble metals.

The Fermi smearing mechanism assumes that the change of reflectance is proportional to the change of Fermi distribution with increasing electron temperature, Eq. (2.4) [28, 29].

$$\frac{\Delta R(\hbar\omega, T_e)}{R_0} \sim f(\hbar\omega, T_e) - f(\hbar\omega, T_0), \tag{2.4}$$

$$f(\hbar\omega, T_e) = \frac{1}{\exp\left(\frac{\hbar\omega+\Delta\varepsilon}{k_B T_e}\right) + 1}. \tag{2.5}$$

Here $\hbar\omega$ is the energy of incident photons equal to 1.55 eV, $\Delta\varepsilon = \varepsilon - \varepsilon_F$ is the difference between the energy level from which an electron is excited and the Fermi level of Ru, T_e and T_0 are the elevated and the initial electron temperatures, respectively. In our case, $\Delta\varepsilon$ is a priory unknown free parameter assumed to be constant for all temperatures, so ε has a meaning of an averaged energy level participating in optical transition.

The Fermi smearing mechanism works in the regime when the photon energy is close to the interband transition energy $\Delta\varepsilon$, which in the case of Ru we attribute to the lower boundary of the pseudo-gap. If we have fixed value $\hbar\omega = 1.55\,\text{eV}$ and variable parameter $\Delta\varepsilon$, we can try to fit temperature-dependent reflectance points by Eq. (2.4) with respect to $\Delta\varepsilon$. Then comparing the fitted value with the lower pseudo-gap boundary taken from Ru DOS will allow us to estimate to what extent

the Fermi smearing is valid in Ru.

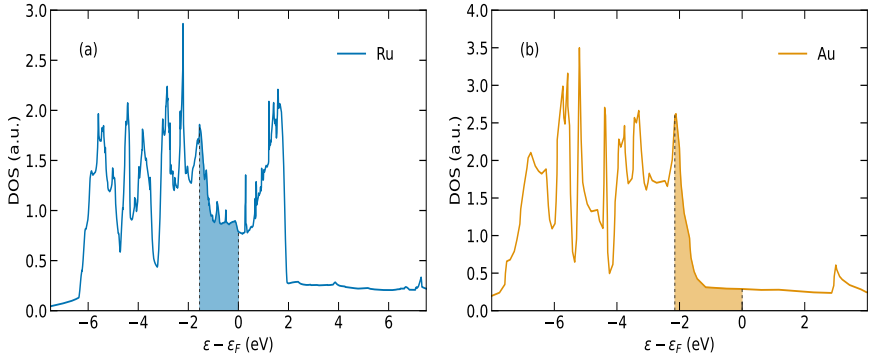

Figure 2.7: (a) DOS of Ru taken from [40] and (b) Au from [45]. Blue fill in Ru DOS represents energy states allowing optical transitions for photons with energies $\hbar\omega = 1.55\,\text{eV}$, orange fill in Au DOS – photons with energies equal to d-band transition threshold.

The T_e-dependence of the peak reflectance changes in Ru (Fig. 2.3) can be taken from the TTM model (Eq. (2.2)) with given incident fluence. For every fluence point, we got two electron temperature values: one is the highest surface temperature reached, and the other value is the temperature at ~ 2 ps after the laser pulse. The first value corresponds to an assumption that the peak change of reflectance corresponds to the maximal heating of the electronic system, and the second value assumes that the peak reflectance change corresponds to the process of electron-lattice equilibration. The result of fitting for 37 nm Ru film is shown in Fig. 2.8.

The fitted averaged energy level $\Delta\varepsilon$ is $-1.20\,\text{eV}$ for T_e at 2 ps. This value is close to the expected -1.5 eV, and thus indicates the validity of the Fermi smearing explanation of the electron temperature dependence of Ru optical properties. For the max T_e, the $\Delta\varepsilon$ value is $-0.97\,\text{eV}$, which is far from the lower boundary of the pseudo-gap. This deviation confirms our suggestion to attribute the peak reflectance to the electron-lattice equilibration (reaching maximal lattice temperature, see Fig. 2.2(b)). Similar results were obtained for other Ru thicknesses. Nevertheless, the applicability of the Fermi smearing mechanism to Ru seems to be limited since the interband contribution to optical transitions is weak but non-vanishing. A more accurate quantitative explanation requires first-principles simulations of Ru in a similar manner to the work [44] and may be provided in our future works.

2.4.3 Damage threshold in Ru

In this section, we investigate the thickness-dependent damage thresholds. Having the SEM images (similar to Fig. 2.5) for all of the samples, we extract thickness-dependent data by attributing the onset of damage to surface cracking. To elaborate on the mechanism of damage we start our analysis with the calculations of the laser-induced melting thresholds.

We provide the calculation of melting thresholds in Ru irradiated by fs laser

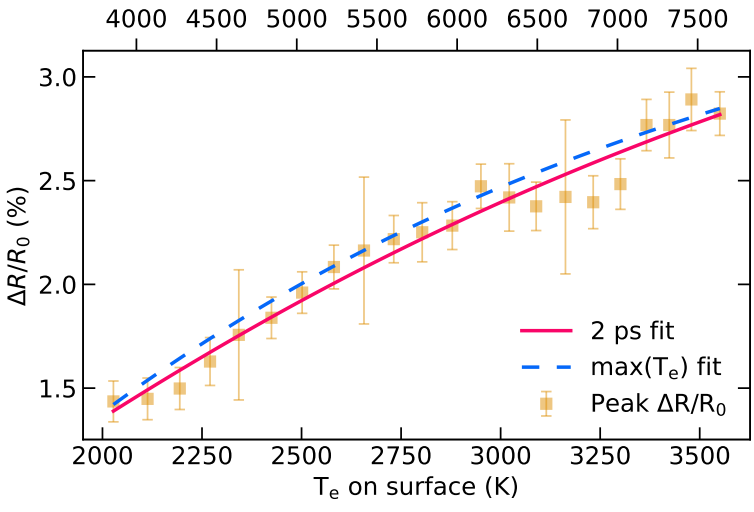

Figure 2.8: Peak reflectance change $\Delta R/R_0$ as a function of electron temperature T_e (orange markers). Red line represents fitting by Fermi smearing function (2.1) for T_e at 2 ps, and blue dashed line is the same for max T_e value. The ticks on the lower horizontal axis indicate surface temperature values at 2 ps. For the upper axis, ticks correspond to the maximal values of electron temperature.

using two approaches. The first is a series of the TTM simulations (Section 2.4.1) for the different Ru thicknesses. The second is the two-temperature – molecular dynamics (TTM-MD) simulations for 75, 100 and 120 nm Ru films. We consider large thicknesses to avoid the effects of multiple reflections of light at the interfaces on the absorption profile and, hence, the necessity to include Si substrate into simulations. The TTM-MD simulations were based on the in-house MD code with the highly adaptive load balancing algorithm [46, 47] allowing to simulate very large systems with a highly non-uniform mass distribution. In both performed approaches, the melting threshold was determined as fluence at which a surface layer of ~ 1 nm becomes liquid. We trace a modified centrosymmetric parameter C_s [48] averaged for atoms within the surface layer. It is known that the perfect hcp crystal has $C_s = 3$, whereas melting happens when C_s drops below 2.5, which is assumed to be a threshold for disordered atom configurations in a liquid phase. In the TTM simulations a layer is considered to be liquid when its lattice temperature overcomes the equilibrium melting temperature $T_l > T_m$, $T_m = 2607$ K. The results of the simulations and their comparison with the SEM-thresholds are shown in Fig. 2.9.

The discrepancy between thresholds taken from SEM and the fluences at which the pump-probe signal starts to increase (dR/dt) indicates that the pump-probe signal stays stable under minor surface changes such as cracks formation. Meanwhile, a factor two difference between experimentally determined thresholds and theoretically predicted melting thresholds most likely indicates that cracking occurs at lower fluences than melting. We suppose that one of the possible origins of

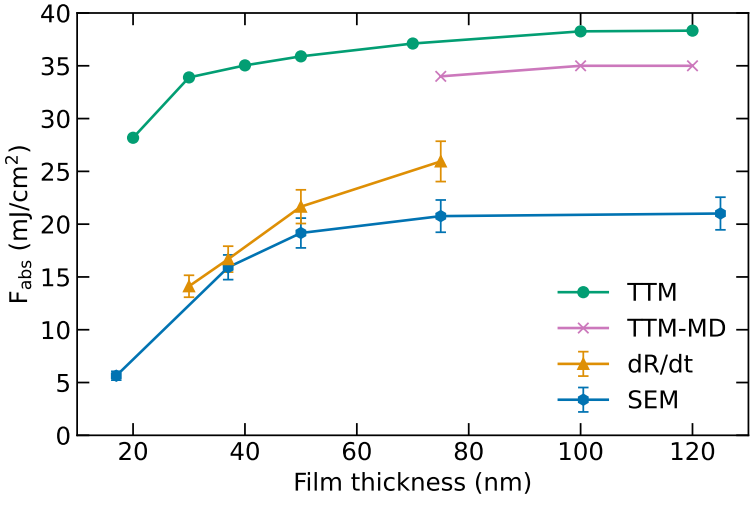

Figure 2.9: Thickness-dependent threshold fluences of Ru films. Blue hexagons are values corresponding to the onset of the SEM-observed cracks, orange triangles correspond to the fluences at which pump-probe curves exhibit increase at long timescales (Table 2.1), green circles are the surface melting thresholds provided by the TTM simulations, and purple crosses are the thresholds taken from the TTM-MD simulations of thick Ru films.

cracking can be fast lateral expansion of a film during laser-induced heating followed by slow cooling due to dissipation of heat from the Ru film into the Si substrate. This leads to a generation of thermo-mechanical stresses accumulating on defects (e.g., grain boundaries or pores). When the stress amplitude reaches critical value, stress tears a film apart forming a crack propagating along the boundaries of defects. Our assumption is confirmed by the results of focused ion beam – scanning electron microscopy (FIB-SEM) analysis shown in Fig. 2.6. FIB-SEM allows to estimate the cracks depth. As one can see in Fig. 2.6(b) and (d), the entire Ru film is torn along the crack path. Most likely, it means that the centers of crack nucleation are not concentrated near film surface but most likely are uniformly distributed in the film.

Additional stresses in a film are generated due to the rotation of the sample. Their contribution can be estimated according to Eq. (55) from [49] for the radial and angular stress tensor components:

$$\sigma_r = \frac{3+\nu}{8}\rho\omega^2(R^2 - r^2),$$
$$\sigma_\theta = \frac{3+\nu}{8}\rho\omega^2 R^2 - \frac{1+3\nu}{8}\rho\omega^2 r^2$$

Here ν is the Poisson ratio of the material, ρ is the material density, ω is an angular velocity, R is the disk radius and r is a considered distance from the center of the disk. Using known parameters for solid Ru $\nu = 0.3$ and $\rho = 12.4\,\mathrm{g/cm^3}$, having $R = 3.8\,\mathrm{cm}$ and typical position of the trace $r = 2\,\mathrm{cm}$, we get an estimation for additional stress $\sigma_r \approx \sigma_\theta \approx 2\,\mathrm{MPa}$. These values are at least three orders of magnitude lower than the tensile strength of hot Ru being 5-20 GPa depending on

temperature and phase [16]. Thus, their influence on the formation of cracks seems to be negligible.

Albeit the theoretically predicted and experimentally observed thickness-dependent thresholds seem to attribute to different damaging mechanisms, they follow a common trend. Thresholds increase together with an increasing thickness of a film until some critical value around 75 nm after which they saturate. This critical thickness is associated with change of absorption from thin-film regime to bulk described by Lambert-Beer's law.

Higher threshold values in the TTM than in the TTM-MD can be explained by the absence of the real surface in the TTM. The latent heat of fusion used in the TTM is taken for the bulk material, and thus does not reproduce the properties of the surface. In contrary, molecular dynamics natively takes into account the weaker bonding of surface atoms and thus describes the process of surface melting in a more natural way. It uses the EAM potential constructed specifically for Ru under intense ultrafast laser excitation and successfully applied to describe laser-induced ablation [16]. The melting temperature predicted by this potential is 2787 K, which is 7 % higher than the experimental value being 2607 K and used in the TTM analysis. This leads to a few percent higher threshold values than one would expect from the experiment, but does not have a major impact on the obtained results.

2.5 Conclusion

We presented measurements of transient pump-probe thermoreflectance in Ru thin films as a function of incident fluence and Ru layer thickness in near-threshold regime. We applied rotational scheme to reduce heat accumulation in a target. An analysis of the measured thermoreflectance signal allowed us to extract information about behavior of hot electrons. However, we could not directly correlate the behavior of thermoreflectance curve to the threshold of irreversible changes in thin Ru films.

The results of hot electrons analysis indicated similarity of electron system response to laser irradiation for noble metals with fully occupied d-bands and Ru with half-filled d-band. We attributed this result to the presence of a pseudo-gap in Ru DOS around the energy of incident photons. Inside this pseudo-gap, interband transitions are weak, and Ru response may be qualitatively described via Fermi smearing mechanism. A similar effect is expected for other metals with pseudo-gap in d-band (e.g. Cr, W) and may be a scope for a dedicated research.

We demonstrated occurrence of three well-separated stages of surface changes during ultrafast laser heating of Ru film: darkening of an irradiation line, surface cracking and grooves formation. Our *post mortem* surface analysis associated appearance of the dark regions with increasing oxidation of the surface or growth of carbon layer.

We compared the cracks formation threshold to the two-temperature and molecular dynamics simulations of the melting threshold. We found that the crack formation threshold is two times lower than theoretical predictions for single-shot melting threshold. This led us to the conclusion that the basic mechanism of cracking is formation of heat-induced stresses in a thin film leading to film tearing. Our results

may serve as the upper limit of operational conditions for optic devices based on Ru thin films.

Acknowledgements

Author is grateful to H. van der Velde for fruitful discussions and technical assistance.
For XTANT calculations, computational resources were supplied by the project "e-Infrastruktura CZ" (e-INFRA LM2018140) provided within the program Projects of Large Research, Development and Innovations Infra-structures.

2.6 Appendix A: XPS analysis

2.6.1 Experimental details

X-ray Photoelectron Spectroscopy (XPS) and Auger Electron Spectroscopy (AES) were performed with a Thermo Scientific Theta Probe instrument at a base pressure below 10^{-9} mbar. This instrument is equipped with a field emission gun for secondary electron imaging, which can be used to obtain AES spectra at a specific spot in a secondary electron microscopy image. AES was initially used to confirm that a higher oxygen concentration could be found in the optically exposed area. After this, XPS was used for more precise quantification of the Ru oxidation.

Monochromatic Al-Kα radiation was used for XPS analysis with an X-ray spot of 20 μm. The instrument collects photoelectrons in a range of $\pm 30°$ around an average take-off angle of 53° with respect to the surface normal and can measure either angle-integrated or in parallel angle-resolved mode (AR-XPS). The binding energy scale of the instrument is calibrated based on reference measurements on sputter cleaned Au, Ag, and Cu foils, such that the binding energy of $Au4f_{7/2}$ is 84.0 eV, that of $Ag3d_{5/2}$ is 368.2 eV, and that of $Cu2p_{3/2}$ is 932.6 eV [50]. To ensure reliable XPS analysis, charge referencing is generally necessary to accurately align the energy scale [51, 52]. However, in our specific case, the metallic Ru3d peak position is reproducible from sample to sample within 0.1 eV margin. We explain it by the good electrical conductivity of native ruthenium oxide [53, 54] that preserves the charge neutrality of the sample surface. Therefore, we did not apply further referencing to the binding energy scale for this particular sample.

The centre of the exposed (circular) line was found by performing an XPS line scan measurement across the exposed line with a step size of 10 μm, measuring the O1s and Ru3d signals. After this, the oxide thickness was determined by AR-XPS measurements at the spot with highest oxygen concentration and a reference point away from the spot with elevated oxygen concentration. The oxide thicknesses were calculated with the overlayer thickness calculator in the Thermo Scientific Avantage software, based on effective attenuation lengths according to the method of Cumpson and Seah [55]. All measurements were carried out without sample pre-treatment and without charge neutralisation

2.6.2 Results

As described in the Section 2.3.2, AES was initially used for determination of the difference in oxygen signal between the optically exposed circular ring and reference spots away from the exposed area. In order to better quantify the difference in oxidation, XPS measurements were performed. Fig. A1 shows results of an XPS line scan across a line perpendicular to the circumference of the optically exposed circular ring. The O1s and Ru3d peak areas are quantified in terms of atomic % (neglecting the contribution of C1s, which is difficult to separate from the Ru3d signal). The XPS results show a slightly elevated O signal over a width of about 100 μm. In order to express the change in oxidation as oxide thickness, angle-resolved XPS measurements were performed on a reference spot (outside the exposed area) and on the exposed area, as depicted by the dashed lines in Fig. A1.

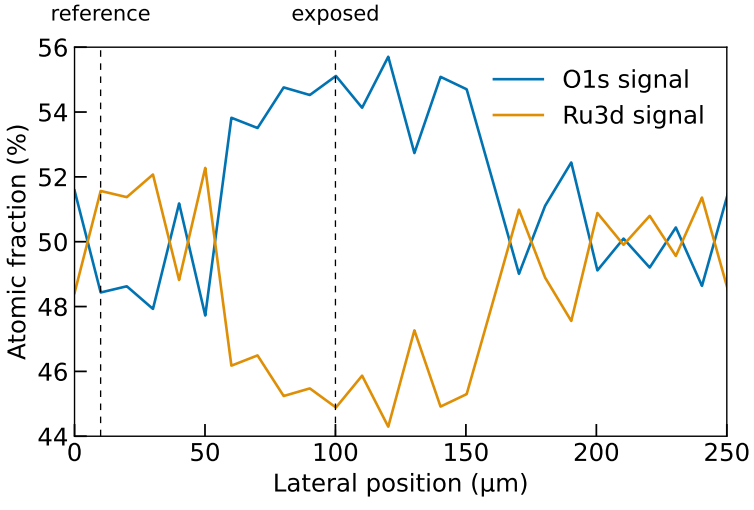

Figure A1: XPS O and Ru signals along a line scan perpendicular to the optically irradiated line on the sample. The vertical dashed lines 'reference' and 'exposed' indicate the positions where angle-resolved XPS measurements were performed for a reference point (outside the exposed area) and the exposed area.

Fig. A2 shows the Ru3d spectra (for a photoelectron take-off angle of 34°) of the exposed (a) and reference (b) spots. Based on a separate reference measurement on sputter cleaned Ru, the spectra have been fitted with Ru3d doublets for Ru metal, Ru oxide and a peak for C1s, which overlaps with the $Ru3d_{3/2}$ peak. The increased oxidation in the exposed spot corresponds to a higher ratio of the RuO_x peak vs. Ru metal. Angle-resolved measurements of this ratio were analysed to express the Ru oxidation as thickness of a RuO_2 film on Ru (assuming bulk densities). This yields RuO_2 thicknesses of 0.8 ± 0.2 nm and 1.2 ± 0.2 nm on the reference and exposed spots, respectively.

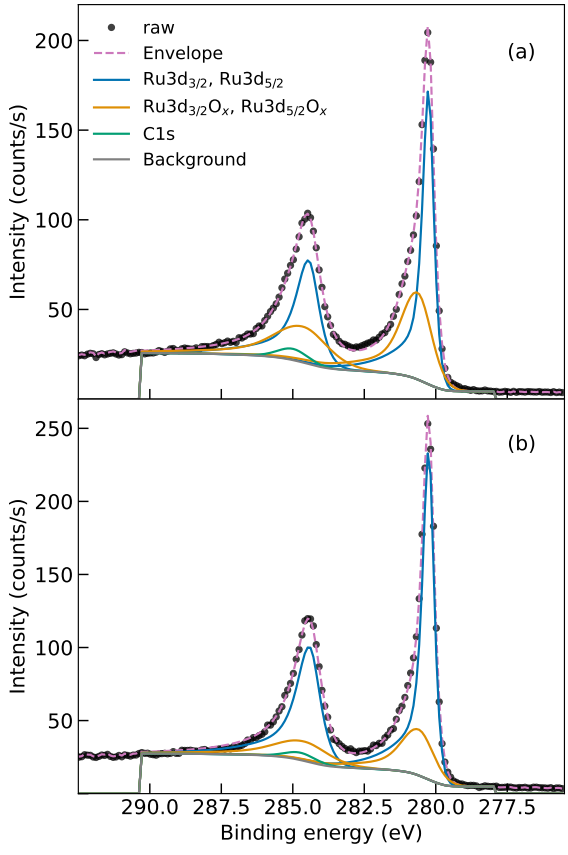

Figure A2: Ru3d XPS spectra of the optically exposed area (a) and the reference spot (b). Points indicate the measured signal, blue line – the fitted Ru metal doublet, orange line – the fitted RuO_x doublet and the green line – the fitted C1s signal. Grey line indicates the Shirley background, and lilac dashed line – envelope signal (sum of background and fitted peaks).

2.7 Appedix B: TEM-EDX analysis of damaged area

To support the results of the XPS analysis, the transmission electron microscopy (TEM) / energy-dispersive X-ray (EDX) mapping was also made. For this study, we chose a spot on line 3 (see Fig. 2.5(a)) because it consists of both areas of severe damage with cracks and areas of surface darkening, making it a suitable location to analyze both types of damage. Fig. B1 shows an overview high-angle annular dark-field (HAADF) TEM image with two well-defined cracks and the corresponding element-specific EDX maps. Interestingly, a series of small subsurface cavities is observed, resembling frozen cavities simulated with MD method in EUV-irradiated Ru film (see Fig. 3(a) in [16]). Fig. B1(c) shows the areas of high oxygen concentration in damaged regions (cracks) as well as on Ru surface and Ru-SiO_x/Si

interface. Small amount of oxygen is present in the region between the two cracks inside Ru layer due to lamella oxidation during transportation to TEM. This type of oxidation is unavoidable.

Fig. B2 shows zoomed-in TEM images of cracked area. According to Fig. B2(c), oxygen content increases significantly only on crack boundaries and inside a crack. We relate this to transiently increased temperature due to laser irradiation and increased amount of Ru surface after crack formation.

Moving further from the center of laser spot (to the left from the region shown on Fig. B1) we found a region which is similar to the left crack on Fig. B1(a). In this region, the film is also detached from the substrate but remains closed. The particular importance of this region is the well-resolved image of separate Ru crystallites with pronounced boundaries between them, see Fig. B3. We did not observe accumulation of oxygen on the grain boundaries as shown in Fig. B3(c). This finding supports our conclusion that the concentration of oxygen inside a film is very low even after high level of irradiation and is not likely responsible for the character of observed damage.

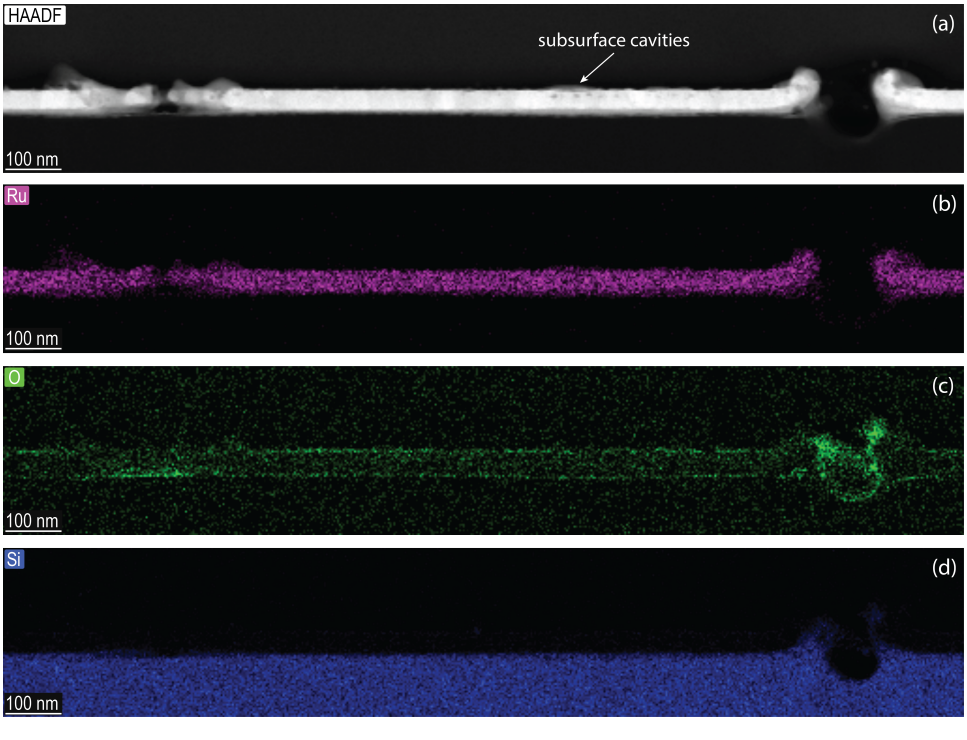

Figure B1: TEM-HAADF image of a lamella taken from laser-induced damage region (a) with EDX maps for Ru (b), O (c) and Si (c).

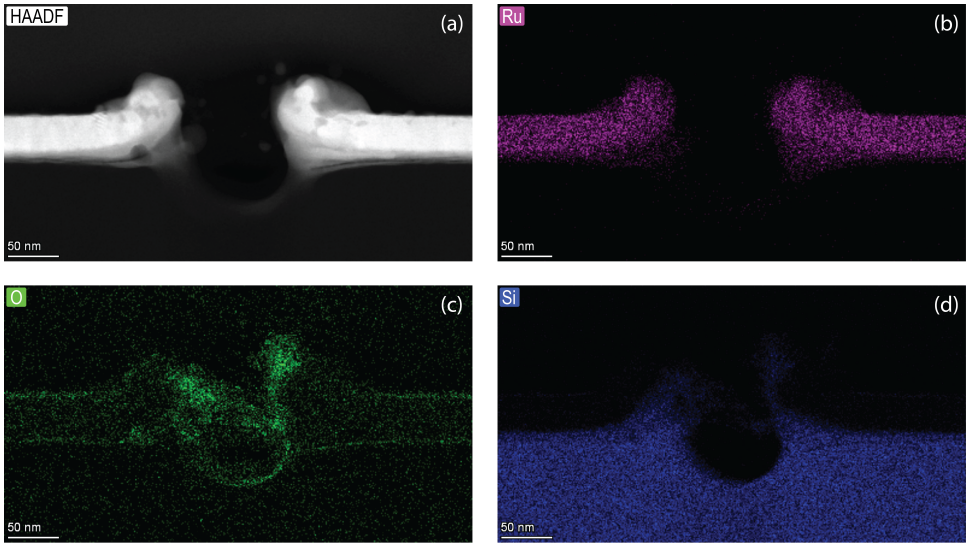

Figure B2: TEM-HAADF image of the crack region (a) with EDX maps for Ru (b), O (c) and Si (d).

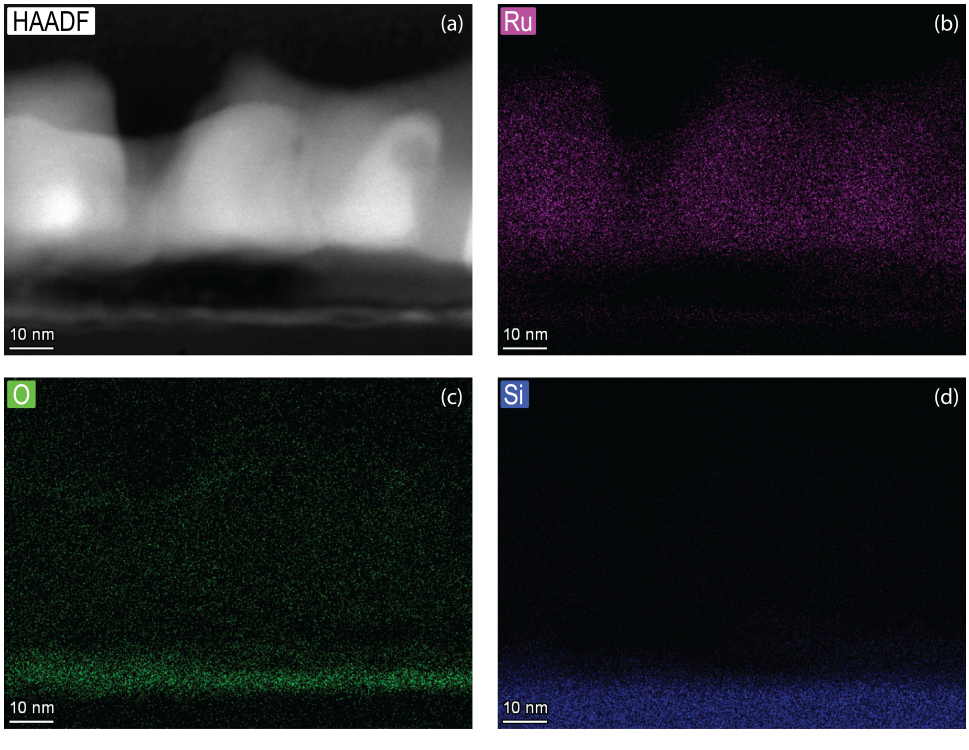

Figure B3: TEM-HAADF image of the partially stable film (a) with EDX maps for Ru (b), O (c) and Si (c).

References

[1] J. Bonse, J. Krüger, S. Höhm, and A. Rosenfeld, *Femtosecond laser-induced periodic surface structures,* Journal of Laser Applications **24**, 042006 (2012).

[2] M. Murakami, B. Liu, Z. Hu, Z. Liu, Y. Uehara, and Y. Che, *Burst-mode femtosecond pulsed laser deposition for control of thin film morphology and material ablation,* Applied Physics Express **2**, 0425011 (2009).

[3] W. Han, L. Jiang, X. Li, Q. Wang, S. Wang, J. Hu, and Y. Lu, *Controllable Plasmonic Nanostructures induced by Dual-wavelength Femtosecond Laser Irradiation,* Scientific Reports **7**, 1 (2017).

[4] D. Zhang, B. Gökce, and S. Barcikowski, *Laser Synthesis and Processing of Colloids: Fundamentals and Applications,* Chemical Reviews **117**, 3990 (2017).

[5] Q. Yang, Z. Cai, Y. Wang, H. Huang, and Y. Wu, *Controllable crystallization of Ge2Sb2Te5 phase-change memory thin films driven by multiple femtosecond laser pulses,* Materials Science and Engineering B: Solid-State Materials for Advanced Technology **193**, 189 (2015).

[6] S. Edward, H. Zhang, S. Witte, and P. C. M. Planken, *Laser-induced ultrasonics for detection of low-amplitude grating through metal layers with finite roughness,* Optics Express **28**, 23374 (2020).

[7] L. Zhao, C. Zhao, C. Xia, Z. Zhang, T. Wu, and H. Xia, *Nanometer Precision Time-Stretch Femtosecond Laser Metrology Using Phase Delay Retrieval,* Journal of Lightwave Technology **39**, 5156 (2021).

[8] J. S. Oh and S.-W. Kim, *Femtosecond laser pulses for surface-profile metrology,* Optics Letters **30**, 2650 (2005).

[9] H. Over, *Surface chemistry of ruthenium dioxide in heterogeneous catalysis and electrocatalysis: From fundamental to applied research,* Chemical Reviews **112**, 3356 (2012).

[10] D. W. Goodman, C. H. Peden, and M. S. Chen, *CO oxidation on ruthenium: The nature of the active catalytic surface,* Surface Science **601**, 18 (2007).

[11] M. R. Axet and K. Philippot, *Catalysis with Colloidal Ruthenium Nanoparticles,* Chemical Reviews **120**, 1085 (2020).

[12] S. Bajt, N. V. Edwards, and T. E. Madey, *Properties of ultrathin films appropriate for optics capping layers exposed to high energy photon irradiation,* Surface Science Reports **63**, 73 (2008).

[13] A. Aquila, R. Sobierajski, C. Ozkan, V. Hájková, T. Burian, J. Chalupský, L. Juha, M. Störmer, S. Bajt, M. T. Klepka, P. Dłużewski, K. Morawiec, H. Ohashi, T. Koyama, K. Tono, Y. Inubushi, M. Yabashi, H. Sinn, T. Tschentscher, a. P. Mancuso, and J. Gaudin, *Fluence thresholds for grazing incidence hard x-ray mirrors,* Applied Physics Letters **106**, 241905 (2015).

[14] I. Milov, I. A. Makhotkin, R. Sobierajski, N. Medvedev, V. Lipp, J. Chalupský, J. M. Sturm, K. Tiedtke, G. de Vries, M. Störmer, F. Siewert, R. van de Kruijs, E. Louis, I. Jacyna, M. Jurek, L. Juha, V. Hájková, V. Vozda, T. Burian, K. Saksl, B. Faatz, B. Keitel, E. Plönjes, S. Schreiber, S. Toleikis, R. Loch, M. Hermann, S. Strobel, H.-K. Nienhuys, G. Gwalt, T. Mey, H. Enkisch, and F. Bijkerk, *Mechanism of single-shot damage of Ru thin films irradiated by femtosecond extreme UV free-electron laser,* Optics Express **26**, 19665 (2018).

[15] I. Milov, V. Lipp, D. Ilnitsky, N. Medvedev, K. Migdal, V. Zhakhovsky, V. Khokhlov, Y. Petrov, N. Inogamov, S. Semin, A. Kimel, B. Ziaja, I. Makhotkin, E. Louis, and F. Bijkerk, *Similarity in ruthenium damage induced by photons with different energies: From vis1. I. Milov, V. Lipp, D. Ilnitsky, N. Medvedev, K. Migdal, V. Zhakhovsky, V. Khokhlov, Y. Petrov, N. Inogamov, S. Semin, A. Kimel, B. Ziaja, I. A. Makhotkin, E. Louis, and ,* Applied Surface Science **501**, 143973 (2020).

[16] I. Milov, V. Zhakhovsky, D. Ilnitsky, K. Migdal, V. Khokhlov, Y. Petrov, N. Inogamov, V. Lipp, N. Medvedev, B. Ziaja, V. Medvedev, I. A. Makhotkin, E. Louis, and F. Bijkerk, *Two-level ablation and damage morphology of Ru films under femtosecond extreme UV irradiation,* Applied Surface Science **528**, 146952 (2020).

[17] I. A. Makhotkin, I. Milov, J. Chalupský, K. Tiedtke, H. Enkisch, G. de Vries, F. Scholze, F. Siewert, J. M. Sturm, K. V. Nikolaev, R. W. E. van de Kruijs, M. A. Smithers, H. A. G. M. van Wolferen, E. G. Keim, E. Louis, I. Jacyna, M. Jurek, D. Klinger, J. B. Pelka, L. Juha, V. Hájková, V. Vozda, T. Burian, K. Saksl, B. Faatz, B. Keitel, E. Plönjes, S. Schreiber, S. Toleikis, R. Loch, M. Hermann, S. Strobel, R. Donker, T. Mey, and R. Sobierajski, *Damage accumulation in thin ruthenium films induced by repetitive exposure to femtosecond XUV pulses below the single-shot ablation threshold,* Journal of the Optical Society of America B **35**, 2799 (2018).

[18] I. A. Makhotkin, R. Sobierajski, J. Chalupský, K. Tiedtke, G. de Vries, M. Störmer, F. Scholze, F. Siewert, R. W. E. van de Kruijs, I. Milov, E. Louis, I. Jacyna, M. Jurek, D. Klinger, L. Nittler, Y. Syryanyy, L. Juha, V. Hájková, V. Vozda, T. Burian, K. Saksl, B. Faatz, B. Keitel, E. Plönjes, S. Schreiber, S. Toleikis, R. Loch, M. Hermann, S. Strobel, H.-K. Nienhuys, G. Gwalt, T. Mey, and H. Enkisch, *Experimental study of EUV mirror radiation damage resistance under long-term free-electron laser exposures below the single-shot damage threshold,* Journal of Synchrotron Radiation **25**, 77 (2018).

[19] K. R. P. Kafka, N. Talisa, G. Tempea, D. R. Austin, C. Neacsu, and E. A. Chowdhury, *Few-cycle pulse laser induced damage threshold determination of ultra-broadband optics,* Optics Express **24**, 28858 (2016).

[20] T. Smausz, T. Csizmadia, C. Tápai, J. Kopniczky, A. Oszkó, M. Ehrhardt, P. Lorenz, K. Zimmer, A. Prager, and B. Hopp, *Study on the effect of ambient gas on nanostructure formation on metal surfaces during femtosecond laser*

ablation for fabrication of low-reflective surfaces, Applied Surface Science **389**, 1113 (2016).

[21] P. Dominic, F. Bourquard, S. Reynaud, A. Weck, J. P. Colombier, and F. Garrelie, *On the insignificant role of the oxidation process on ultrafast high-spatial-frequency lipss formation on tungsten,* Nanomaterials **11**, 1 (2021).

[22] B. K. Nayak and M. C. Gupta, *Self-organized micro/nano structures in metal surfaces by ultrafast laser irradiation,* Optics and Lasers in Engineering **48**, 940 (2010).

[23] W. S. Fann, R. Storz, H. W. Tom, and J. Bokor, *Electron thermalization in gold,* Physical Review B **46**, 13592 (1992).

[24] C. K. Sun, F. Vallée, L. H. Acioli, E. P. Ippen, and J. G. Fujimoto, *Femtosecond-tunable measurement of electron thermalization in gold,* Physical Review B **50**, 15337 (1994).

[25] S.-S. Wellershoff, J. Hohlfeld, J. Gudde, and E. Matthias, *The role of electron-phonon coupling in femtosecond laser damage of metals,* Applied Physics A Materials Science & Processing **69**, S99 (1999).

[26] B. Rethfeld, K. Sokolowski-Tinten, D. Von Der Linde, and S. I. Anisimov, *Timescales in the response of materials to femtosecond laser excitation,* Applied Physics A: Materials Science and Processing **79**, 767 (2004).

[27] B. Rethfeld, D. S. Ivanov, M. E. Garcia, and S. I. Anisimov, *Modelling ultrafast laser ablation,* Journal of Physics D: Applied Physics **50** (2017), 10.1088/1361-6463/50/19/193001.

[28] W. Lynch and R. Rosei, *Thermomodulation Spectra of Al, Au, and Cu,* Physical Review B **5**, 3883 (1972).

[29] R. W. Schoenlein, W. Z. Lin, J. G. Fujimoto, and G. L. Eesley, *Femtosecond studies of nonequilibrium electronic processes in metals,* Physical Review Letters **58**, 1680 (1987).

[30] G. de Haan, J. Hernandez-Rueda, and P. C. M. Planken, *Femtosecond time-resolved pump-probe measurements on percolating gold in the ablation regime,* Optics Express **28**, 12093 (2020).

[31] O. Gunnarsson, P. Gies, W. Hanke, and O. K. Andersen, *Ab initio method for calculating response functions in transition metals,* Physical Review B **40**, 12140 (1989).

[32] I. G. Gurtubay, J. M. Pitarke, W. Ku, A. G. Eguiluz, B. C. Larson, J. Tischler, P. Zschack, and K. D. Finkelstein, *Electron-hole and plasmon excitations in 3d transition metals: Ab initio calculations and inelastic x-ray scattering measurements,* Physical Review B - Condensed Matter and Materials Physics **72**, 1 (2005).

[33] C. Ambrosch-Draxl and J. O. Sofo, *Linear optical properties of solids within the full-potential linearized augmented planewave method,* Computer Physics Communications **175**, 1 (2006).

[34] M. Cazzaniga, L. Caramella, N. Manini, and G. Onida, *Ab initio intraband contributions to the optical properties of metals,* Physical Review B - Condensed Matter and Materials Physics **82**, 1 (2010).

[35] J. Hohlfeld, S.-S. Wellershoff, J. Güdde, U. Conrad, V. Jähnke, and E. Matthias, *Electron and lattice dynamics following optical excitation of metals,* Chemical Physics **251**, 237 (2000).

[36] R. Chartrand, *Numerical Differentiation of Noisy, Nonsmooth Data,* ISRN Applied Mathematics **2011**, 1 (2011).

[37] UDCM-Group, *AbsorptionTMM,* (2019).

[38] S. Anisimov, B. Kapeliovich, and T. Perel-man, *Electron emission from metal surfaces exposed to ultrashort laser pulses,* Journal of Experimental and Theoretical Physics (1974).

[39] F. Akhmetov, N. Medvedev, I. Makhotkin, M. Ackermann, and I. Milov, *Effect of Atomic-Temperature Dependence of the Electron–Phonon Coupling in Two-Temperature Model,* Materials **15**, 5193 (2022).

[40] Y. Petrov, K. Migdal, N. Inogamov, V. Khokhlov, D. Ilnitsky, I. Milov, N. Medvedev, V. Lipp, and V. Zhakhovsky, *Ruthenium under ultrafast laser excitation: Model and dataset for equation of state, conductivity, and electron-ion coupling,* Data in Brief **28**, 104980 (2020).

[41] S. P. Zhvavyi and G. D. Ivlev, *Influence of the Initial Temperature of Silicon on Crystallization of a Layer Melted by Nanosecond Laser Heating,* Journal of Engineering Physics and Thermophysics **69**, 790 (1997).

[42] N. M. Bulgakova, R. Stoian, A. Rosenfeld, I. V. Hertel, W. Marine, and E. E. Campbell, *A general continuum approach to describe fast electronic transport in pulsed laser irradiated materials: The problem of Coulomb explosion,* Applied Physics A: Materials Science and Processing **81**, 345 (2005).

[43] P. M. Norris, A. P. Caffrey, R. J. Stevens, J. M. Klopf, J. T. McLeskey, and A. N. Smith, *Femtosecond pump-probe nondestructive examination of materials (invited),* Review of Scientific Instruments **74**, 400 (2003).

[44] E. Bévillon, R. Stoian, and J. P. Colombier, *Nonequilibrium optical properties of transition metals upon ultrafast electron heating,* Journal of Physics Condensed Matter **30** (2018), 10.1088/1361-648X/aad8e5.

[45] A. Blumenstein, E. S. Zijlstra, D. S. Ivanov, S. T. Weber, T. Zier, F. Kleinwort, B. Rethfeld, J. Ihlemann, P. Simon, and M. E. Garcia, *Transient optics of gold during laser irradiation: From first principles to experiment,* Physical Review B **101**, 1 (2020).

[46] V. Zhakhovskii, K. Nishihara, Y. Fukuda, S. Shimojo, T. Akiyama, S. Miyanaga, H. Sone, H. Kobayashi, E. Ito, Y. Seo, M. Tamura, and Y. Ueshima, *A new dynamical domain decomposition method for parallel molecular dynamics simulation,* 2005 IEEE International Symposium on Cluster Computing and the Grid, CCGrid 2005 **2**, 848 (2005).

[47] M. S. Egorova, S. A. Dyachkov, A. N. Parshikov, and V. V. Zhakhovsky, *Parallel SPH modeling using dynamic domain decomposition and load balancing displacement of Voronoi subdomains,* Computer Physics Communications **234**, 112 (2019).

[48] S. Murzov, S. Ashitkov, E. Struleva, P. Komarov, V. Zhakhovsky, V. Khokhlov, and N. Inogamov, *Elastoplastic and polymorphic transformations of iron at ultra-high strain rates in laser-driven shock waves,* Journal of Applied Physics **130** (2021), 10.1063/5.0076869.

[49] S. Timoshenko and J. N. Goodier, *Theory of Elasticity: By S. Timoshenko and JN Goodier* (McGraw-Hill, 1951).

[50] M. P. Seah, *Summary of ISO/TC 201 standard: VII ISO 15472 : 2001 - surface chemical analysis - x-ray photoelectron spectrometers - calibration of energy scales,* Surface and Interface Analysis **31**, 721 (2001).

[51] G. Greczynski and L. Hultman, *Compromising Science by Ignorant Instrument Calibration—Need to Revisit Half a Century of Published XPS Data,* Angewandte Chemie - International Edition **59**, 5002 (2020).

[52] G. Greczynski and L. Hultman, *X-ray photoelectron spectroscopy: Towards reliable binding energy referencing,* Progress in Materials Science **107**, 100591 (2020).

[53] J. Riga, C. Tenret-Noël, J. J. Pireaux, R. Caudano, J. J. Verbist, and Y. Gobillon, *Electronic Structure of Rutile Oxides TiO2, RuO2 and IrO2 Studied by X-ray Photoelectron Spectroscopy,* Physica Scripta **16**, 351 (1977).

[54] M. M. Steeves, *ProQuest Dissertations and Theses*, Ph.D. thesis, The University of Maine, United States – Maine (2011).

[55] P. J. Cumpson and M. P. Seah, *Elastic scattering corrections in AES and XPS. II. Estimating attenuation lengths and conditions required for their valid use in overlayer/substrate experiments,* Surface and Interface Analysis **25**, 430 (1997).

3

Effect of Atomic-Temperature Dependence of the Electron–Phonon Coupling in Two-Temperature Model

Ultrafast laser irradiation of metals can often be described theoretically with the two-temperature model. The energy exchange between the excited electronic system and the atomic one is governed by the electron–phonon coupling parameter. The electron–phonon coupling depends on both, the electronic and the atomic temperature. We analyze the effect of the dependence of the electron–phonon coupling parameter on the atomic temperature in ruthenium, gold, and palladium. It is shown that the dependence on the atomic temperature induces nonlinear behavior, in which a higher initial electronic temperature leads to faster electron–phonon equilibration. Analysis of the experimental measurements of the transient thermoreflectance of the laser-irradiated ruthenium thin film allows us to draw some, albeit indirect, conclusions about the limits of the applicability of the different coupling parameterizations.

3.1 Introduction

Metals irradiation with ultrashort high-intensity laser pulses is an important tool for both fundamental and applied science. Ultrafast energy deposition into matter drives it into a poorly explored nonequilibrium regime, where unusual material properties and kinetics take place [1, 2]. At the same time, it has a broad range of applications such as micromachining, nanotechnology, and materials processing [3–5].

Under ultrafast-laser irradiation, a cascade of physical effects takes place, ultimately leading to observable material modifications. Firstly, upon photon absorption, the electronic system of the target acquires a nonequilibrium distribution [2]. During this transient stage, electrons scatter among themselves, thermalizing; their distribution function relaxes to its equilibrium Fermi–Dirac one. Typically, it is assumed that this nonequilibrium stage is short-lived and the electronic ensemble thermalizes at femtosecond timescales. However, in some cases, the out-of-equilibrium state may last for a few hundred femtoseconds up to a picosecond, depending on the excitation level and particular material [6, 7].

The energy in the electronic system also dissipates via spatial diffusion outwards from the laser spot in the depth of the material. At the same time, the electrons interact with the lattice via electron–ion (or electron–phonon) scattering. This process transfers the energy absorbed from the laser pulse by electrons to the ionic system of the target.

Phonons, receiving energy from the electrons, can be out-of-equilibrium for even longer times [8]. Relaxation of electrons and phonons and the energy flow between them ultimately define the dynamics of laser-irradiated materials and their final state after irradiation.

The thermal energy flow between electrons and phonons is controlled by the electron–phonon coupling parameter. There were numerous theoretical attempts to calculate this parameter for laser-excited materials [9, 10], with the results showing large discrepancies [11]. The electron–phonon, or in a more general way, electron–ion coupling parameter, essentially depends on the current state of the excited material, meaning it is a function of material dynamical variables such as temperature, density, structure, etc. That makes it challenging to calculate and integrate into available models dedicated to simulating laser–matter interaction.

The most well-known and widely used model that takes into account electron–phonon energy exchange is the two-temperature model (TTM) [12]. In the TTM, a constant or electron-temperature-dependent coupling parameter is typically used [2]. Extensions of the TTM treating different electronic bands and/or different phonon modes separately, each with its own temperature, result in various multi-temperature approaches [13, 14]. Such approaches require even more detailed knowledge of the electron–phonon coupling parameter [15].

Apart from theoretical efforts, the tremendous recent development of experimental techniques using ultrafast electron and/or X-ray diffraction enables probing transient states of laser-excited materials with unprecedented spatial and temporal resolution [16, 17]. Such methods allow extracting the electron–phonon coupling parameter as a function of irradiation conditions, which can be translated into material

dynamical variables using an appropriate theoretical model [8, 18]. Such experimental progress stimulates further studies on the electron–phonon coupling parameter which remains one of the least known properties of laser-irradiated materials.

In the previous work, a tight-binding (TB) molecular dynamics (MD) approach to calculate the electron–phonon coupling parameter as a function of electron temperature for various metals across the Periodic Table was used. In the present work, we extend the previous research, focusing on the dependence of the coupling parameter on the atomic temperature. Such dependence was typically ignored in previous works but may be significant at high irradiation doses, as we demonstrate with basic TTM calculations for ruthenium, palladium, and gold elemental metals. We also compare calculations of the coupling parameter using two different parameterizations of the TB part of our model. Finally, we test various calculated coupling parameters on the example of ruthenium using data from our recent optical pump-probe thermoreflectance measurements [19], which allow us to draw some qualitative conclusions [19].

3.2 Model

To study the response of the metallic target to ultrafast irradiation, we employed the two-temperature model [12, 20]:

$$\begin{cases} C_e(T_e)\frac{\partial T_e}{\partial t} = \frac{\partial}{\partial x}\left(k(T_e,T_a)\frac{\partial T_e}{\partial x}\right) - G(T_e,T_a)(T_e - T_a) + S(t,x), \\ C_a\frac{\partial T_a}{\partial t} = G(T_e,T_a)(T_e - T_a). \end{cases} \tag{3.1}$$

Here T_e is the electronic temperature, and T_a is the atomic one, $C_e(T_e)$ is the volumetric electron heat capacity dependent on the electronic temperature (its independence of the atomic temperature will be justified below), $k(T_e,T_a)$ is the electron thermal conductivity dependent on both T_e and T_a, $G(T_e,T_a)$ is the electron–ion coupling, $S(t,x)$ is an external heat source [19] and C_a is the volumetric atomic heat capacity assumed to be constant according to the Dulong–Petit law in the temperature regime we are interested in here.

To study the influence of the electron–ion coupling on temperature evolution in the metals studied, in Section 3 we consider a system to be homogeneously and instantaneously heated by a delta-like laser pulse, serving as the energy source, to the elevated electron temperature $T_{e,init}$. In that way, the heat diffusion term can be neglected, and system (3.1) is solved with the initial conditions:

$$\begin{cases} T_e(0) = T_{e,init}(\text{ K}), \\ T_a(0) = 300\text{ K}. \end{cases} \tag{3.2}$$

By varying the initial electronic temperature $T_{e,init}$ we studied the electron–phonon relaxation times for equilibrium and kinetics in various metals: ruthenium, palladium, and gold.

Equations (3.1) require the knowledge of the parameters C_a, $C_e(T_e)$, $k(T_e,T_a)$ and $G(T_e,T_a)$. They need to be provided as external parameters in the model. The atomic heat capacity, C_a, and the electron thermal conductivity $k(T_e,T_a)$ may be

found in the literature, e.g., [21–23]. To calculate the electron–phonon coupling parameter and the electronic heat capacity, we employed a hybrid code XTANT-3 [24]. The methodology of calculation of the parameters was developed in [11], here we only briefly recall its most essential points. It is based on the combined model of the Boltzmann collision integrals with the TBMD. The transferable TB method allows calculating the transient band structure of the material, the electronic wave functions, and the atomic potential energy surface (interatomic forces required for MD simulations). The overlap of the electronic wave functions with the atomic translation operator provides the probabilities of the nonadiabatic transitions: electron transitions induced by atomic displacements [25, 26].

Such calculations provide the transition rates for transitions of electrons between energy levels (band structure) of the materials as a response to atomic displacements. Each atomic displacement results in the evolution of the Hamiltonian of the system, thereby allowing us to construct overlap of electronic wave functions for calculations of the nonadiabatic matrix elements [11]. The calculated matrix elements enter the Boltzmann collision integral. In turn, it enabled us to calculate the energy exchange rate between electrons and atoms, and thus the electron–ion coupling parameter.

The MD simulation traces atomic dynamics in realtime, allowing for any atomic motion—it is not restricted to harmonic oscillations in a perfect periodic structure (phononic approximation of the crystal). Thus, the used method does not imply phononic approximation. Electronic transitions in response to any atomic displacement were calculated, which included an anharmonic atomic motion, such as can be present in melted and/or nonequilibrium systems. Thus, throughout this work, we may use the terms "electron–phonon", "electron–ion" or "electron–atom" coupling interchangeably.

For the materials studied here, we employed two different transferable TB parameterizations: the Naval Research Laboratory (NRL [27, 28]) tight-binding parameterization used in our previous work, and the Density-Functional-based Tight-Binding (DFTB) parameterization [29]. These methods provide the radial functions of the hopping integrals, overlap functions, and repulsive potentials (in the case of DFTB), which allowed us to construct the tight-binding Hamiltonian and calculate interatomic forces for an arbitrary atomic configuration. Both parameterizations employ the Slater–Koster tight-binding scheme with an sp^3d^5 linear combination of atomic orbitals (LCAO) basis [27, 30]. For ruthenium, we use the DFTB parameters reported in [31], whereas for other metals matsci-0-3 set of parameters is applied [32].

For the calculation of the electronic heat capacity, we used the standard definition via the derivative of the electronic entropy with respect to the electronic temperature [33]. TB calculations provided us with the required electronic band structure. We performed a series of simulations with various atomic temperatures, T_a, to extract the electron–phonon coupling parameters as functions of T_a. As has been shown in Refs. [11, 33], the coupling parameter is nearly linearly proportional to the atomic temperature.

Thus, we approximated the dependence of the coupling on T_a with the following

relation [33]:

$$G(T_e, T_a) = G(T_e)\left(1 + \alpha\left[\frac{T_a}{300\ \mathrm{K}} - 1\right]\right), \tag{3.3}$$

where $G(T_e)$ is the coupling parameter dependent on the electronic temperature, and α is the proportionality coefficient to be determined from the TBMD calculations.

3.3 Results

3.3.1 Electron–phonon Coupling Parameter and Electron Heat Capacity

In a series of XTANT-3 calculations, we extract the electronic heat capacity and the electron–phonon coupling parameter for various electronic and atomic temperatures in ruthenium, palladium, and gold. $G(T_e)$, $C_e(T_e)$ are shown in Figs. 3.1–3.3. The parameters α scaling the coupling parameter dependence on the atomic temperature (entering Eq. (3.3)) are presented in Table 3.1.

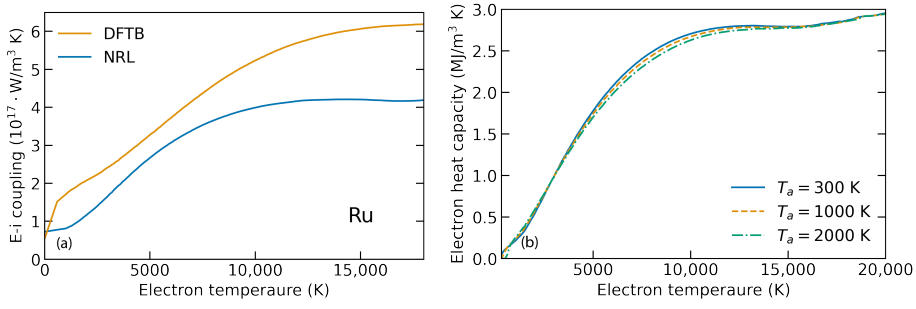

Figure 3.1: (a) Electron–ion couplings $G(T_e)$ in ruthenium calculated using NRL and DFTB parameterizations. (b) Electron heat capacity in ruthenium calculated for different atomic temperatures.

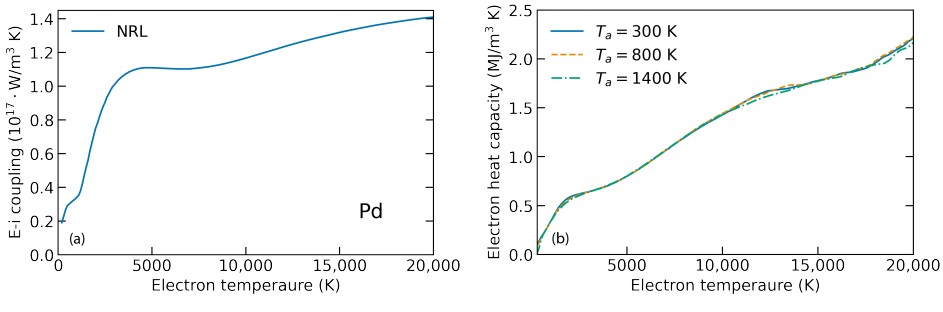

Figure 3.2: (a) Electron–ion couplings $G(T_e)$ in palladium calculated using NRL parameterization. (b) Electron heat capacity in palladium calculated for different atomic temperatures.

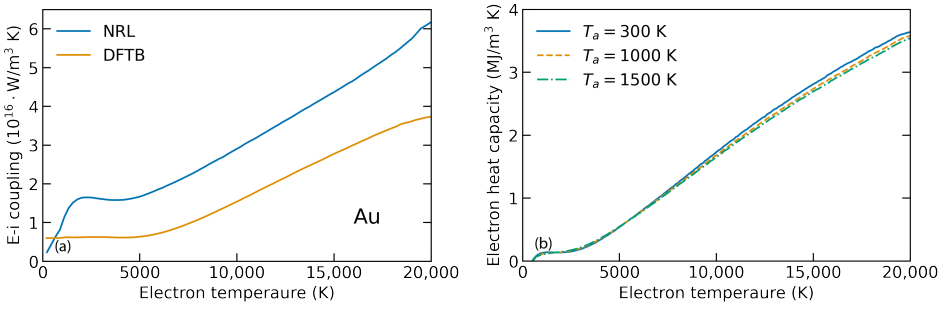

Figure 3.3: (a) Electron–ion couplings $G(T_e)$ in gold calculated using NRL and DFTB parameterizations. (b) Electron heat capacity in gold calculated for different atomic temperatures.

Material	α	
	NRL	DFTB
Ru	0.55	0.45
Pd	0.55	-
Au	0.45	0.65

Table 3.1: Parameter α of the linear dependence of the coupling on T_a in Eq. (3.3).

The electron heat capacities were calculated for different atomic temperature values below the respective melting points of the materials. Figs. 3.1-3.3 (b) show that C_e is almost independent of T_a, justifying the omittance of the dependence made above. In all studied materials, the electron heat capacities calculated agree well with other calculations, e.g., [9, 23]. This validates our methodology, demonstrating that the used tight-binding models are well capable of calculating the electronic properties of the reported metals.

The electron–phonon coupling parameters' dependencies on the electronic temperature, calculated with NRL parameterizations, were previously reported in ref. [11], where they were compared to the available experimental data and other calculations. The agreement in gold at high electronic temperatures validated the method [11]. In the current work, the main point is to extend it to the high atomic temperature and analyze its influence on the outcome of the TTM calculations (see the next section).

Additionally, in the two materials for which different TB parameterizations are available (ruthenium and gold, Figs. 3.1 and 3.3), we analyze the influence of the parameterization on $G(T_e, T_a)$. The calculated coupling parameters are noticeably different in both metals—the difference may reach up to 50%. A strong influence of parameterization on the electron–phonon coupling in unexcited materials (at room or cryogenic temperatures) is well-known [11, 34]. Here, we confirm that the difference persists in the high-electron-temperature regime. In ruthenium, the DFTB parameterization results in higher values of the coupling than the NRL one, whereas in gold it is the opposite. Thus, we cannot conclude a systematic influence

of the TB parameterization, and each material and parameterization requires a dedicated analysis.

3.3.2 The Role of Atomic Temperature Dependence in the Heat Dynamics

Let us start with the analysis of the influence of atomic temperature on heat dynamics. We consider homogeneously heated metal films with the coupling including the dependence on the atomic temperature $G(T_e, T_a)$, and excluding it for comparison, assuming only the electron-temperature-dependent coupling parameter $G(T_e) = G(T_e, T_a = 300\text{ K})$. Fig. 3.4 shows the results obtained with the electron–ion coupling calculated using the NRL parameterization. The initial electron temperatures were taken in the range 5 kK–20 kK due to the following reasons: XTANT is unable to provide accurate electron–ion coupling values for the electron temperatures below $\sim 2-3$ kK [11]; the upper limit is chosen such that the electron temperature stays far from the plasma limit ($T_e \ll E_F/k_B$) [35], and would not induce significant nonthermal effects such as phonon hardening or considerable electronic pressure [36, 37]. Such effects could alter the interatomic potential, and thereby influence parameters of the atomic system, making, e.g., atomic heat capacity and heat conductivity dependent on the electronic temperature. Since these effects play a role only at higher electronic temperatures, it justifies the approximations used for the atomic heat capacity.

Fig. 3.4 (a),(c),(e) show the electron–ion relaxation times in three considered metals, defined as the moment when the difference between the electronic and the atomic temperatures drops to $1/e$ from the maximal value. $G(T_e)$ results in a much slower equilibration of the electronic and ionic temperatures, as seen in Fig. 3.4.

As follows from Equations (3.1)-(3.3), at $t = 0$ ($T_a(0) = 300\,\text{K}$) the starting energy exchange between electrons and ions is the same in both cases, with or without the dependence on T_a. After a non-negligible amount of energy is transferred to the ionic system and its temperature increases, the linear term in Eq. (3.3) makes the electron–ion relaxation up to five times faster (e.g., Fig. 3.4 (a)). At high T_e values, $G(T_e)$ in Ru and Pd vary slowly and result in the almost constant electron–ion (e–i) relaxation time if the dependence on T_a is excluded, see Fig. 3.4 (a),(c).

The electron–ion relaxation times in gold (Fig. 3.4 (e)) have a pronounced peak at $T_{e,init}$ around 12 kK (7.5 kK for the case $G = G(T_e, T_a)$). This peak can be partially attributed to the minimum of $G(T_e)$ around $T_e = 5$ kK (see Fig. 3.3). When T_e decreases from 12 kK to 5 kK, coupling weakens, and energy transfer from electrons to ions slows down resulting in a longer relaxation time. However, at higher initial temperatures two systems exchange a large amount of energy before T_e reaches 5 kK and coupling weakening does not play a significant role. A similar mechanism works in Pd (Fig. 3.4 (c)), but instead of a peak it results in a plateau at $T_{e,init} \geq 15$ kK due to a very slow increase of $G(T_e)$ after the minimum.

In contrast, T_a-dependence of the coupling leads to decreasing relaxation with increasing $T_{e,init}$ for all of the considered metals. Fig. 3.4 (b),(d) clearly demonstrate that with an increase in the initial electronic temperature, the equilibrium is reached faster. In Fig. 3.4 (f) this effect is less pronounced due to the above-

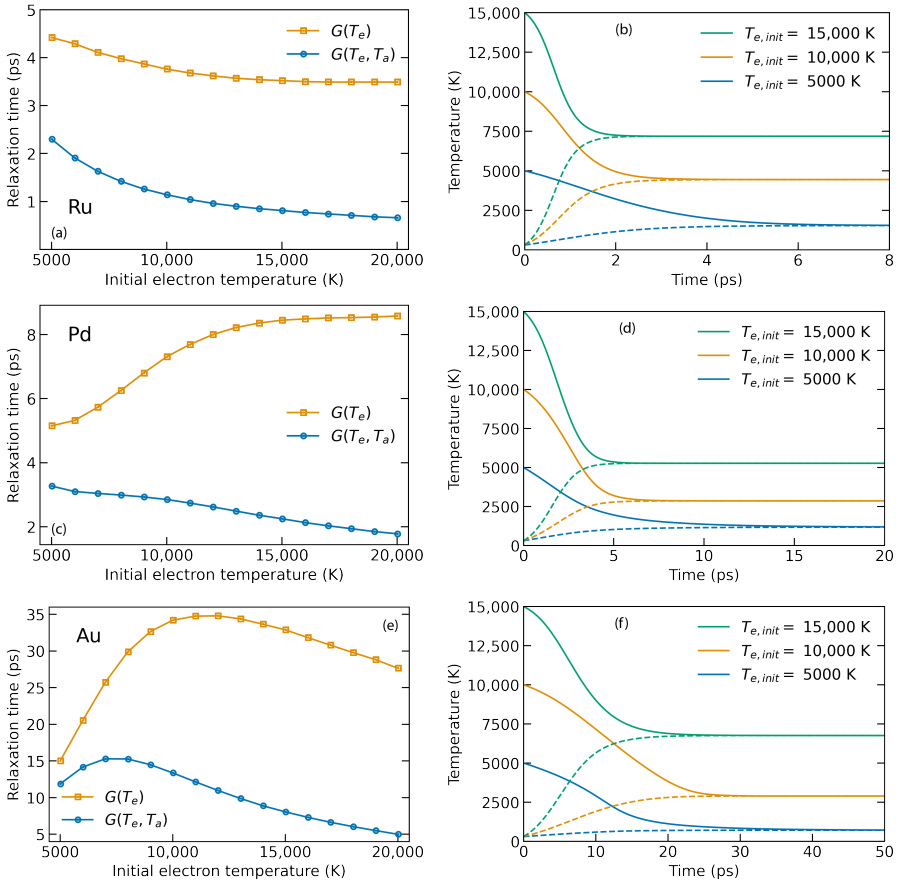

Figure 3.4: (a, c, e) Electron–ion relaxation times, calculated using both electronic- and atomic-temperature-dependent coupling (blue) and only electronic-temperature-dependent coupling (orange). (b, d, f) Examples of T_e- and T_a-profiles calculated using $G(T_e, T_a)$ for different starting electronic temperatures; solid lines are the electronic temperatures, and dashed lines are the ionic ones. (a,b) correspond to Ru, (c,d) to Pd, (e,f) to Au.

discussed minimum of $G(T_e)$ in gold, but still can be found in a comparison of profiles corresponding to $T_{e,init} = 10\,\mathrm{kK}$ (orange lines) and $T_{e,init} = 15\,\mathrm{kK}$ (green lines). Such a nonlinear effect is only observed if the dependence of the coupling parameter on the phonon temperature is taken into account. It indicates its importance for modeling materials' response to ultrafast irradiation, as was also recently noted in ref. [38].

It Is expected that a fast phase transition from solid to a molten state should ensue, which can be directly measured in, e.g., ultrafast diffraction experiments. This result suggests that electron–ion coupling relaxation time should be observable, which could elucidate the role of the atomic temperature dependence of the coupling parameter and validate our calculations in future dedicated experiments.

3.3.3 The Role of Parameterization

Now, let us consider the effect of the chosen TB parameterization on the temperature kinetics on the example of homogeneously heated ruthenium and gold films.

Fig. 3.5 (a) shows electron–ion relaxation times in ruthenium with atomic-temperature-dependent coupling parameter $G = G(T_e, T_a)$ calculated with NRL and DFTB parameterizations. In this case, relaxation times weakly depend on the chosen parameterization. One could expect a divergence between parameterizations at $T_{e,init} > 10\,\text{kK}$ as follows from Fig. 3.1 (a), but the difference in T_e-dependent coupling parameters is suppressed by the dependence on T_a, which is stronger for NRL parameterization. At the initial electron temperatures around 19 kK (this temperature is equivalent to the absorbed energy density of $E_{abs} = 3.46$ eV/atom via the relation $E_{abs} = \int C_e dT_e$) the relaxation time reaches values as small as 0.5 ps.

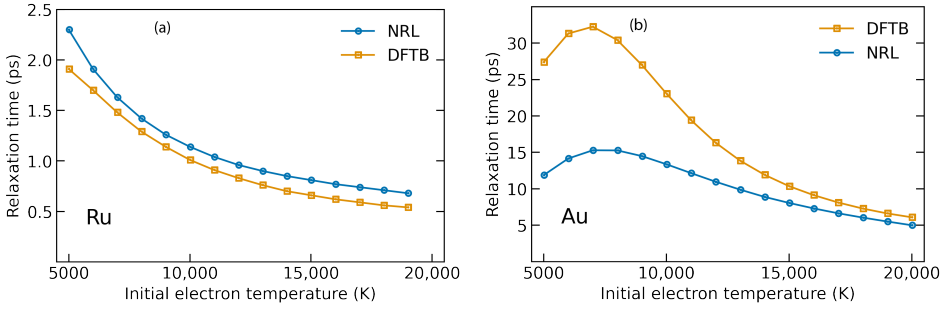

Figure 3.5: (a) Electron–ion relaxation times in ruthenium (a) and gold (b), calculated using two different TB parameterizations: NRL (blue) and DFTB (orange).

Electron–ion relaxation times in gold (Fig. 3.5 (b)) demonstrate a strong dependence on the parameterization at low and intermediate values of $T_{e,init}$. At high $T_{e,init} > 15\,\text{kK}$, the choice of the parameterization has a smaller impact on the relaxation times. This follows from two factors. First, the overall difference between the coupling parameters decreases with the increasing electronic temperature as soon as hot electrons behave like a free-electron gas (high T_e). Second, the larger value of α for DFTB parameterization results in the approaching of DFTB-calculated coupling to NRL-calculated one with the increasing atomic temperature. Both effects lead to similar values of the coupling parameters at high electronic and atomic temperatures.

The results show that the electron–phonon relaxation times in Ru are almost independent of the chosen parameterization. In contrast, the relaxation times in Au are rather sensitive to the tight-binding parameterization used for the calculation of the coupling parameter in the regime of low and intermediate electron temperatures. A similar conclusion was recently drawn from the analysis of electroconductivity in warm dense aluminum [39].

The electron–ion relaxation time in elemental gold may vary by a factor of two in certain cases, proportionally to the differences in the coupling parameter. This strong difference may be detectable in well-controlled experiments, which should

allow for validating the parameterization applicability to calculations of the coupling parameter. We will discuss possible experiments that could provide access to the coupling parameter in the next section.

3.4 Discussion

Direct experimental measurement of the electron–phonon coupling parameter in the highly-excited matter is a very complex task. Unambiguous measurements would require a simultaneous tracing of the electronic and atomic temperatures with femtosecond resolution, which so far has not been achieved. The most advanced techniques at present measure only the transient atomic temperature with the help of the ultrafast electron or X-ray diffraction [13, 40, 41]. Such methods require state-of-the-art large-scale facilities and are thus extremely rare. Alternative simpler methods of accessing electron–phonon coupling at high electronic temperatures are in high demand.

One of the possible ways to measure electron–phonon coupling in laser-excited materials is based on transient thermoreflectance experiments [42]. In such experiments, the ultrashort pump beam brings a target into a highly nonequilibrium state between the electronic and the phononic systems. The probe beam comes to the target with a variable delay and generates a transient thermoreflectance signal providing information about heat dynamics in a studied target. This signal is then fitted by the temperature profiles taken from the TTM simulations with a variable electron–ion coupling (see e.g., [43, 44]). In such a fitting procedure, usually, the reflectance dependence on temperatures is either taken in a model approximation, e.g., Drude model, or assumed to be linearly dependent on T_e and T_a [45]:

$$R(T_e, T_a) = a\Delta T_e + b\Delta T_a. \tag{3.4}$$

In the case of transition metal Ru with a half-occupied d-band that we consider in this section, the Drude model is not able to provide reliable temperature-dependent optical properties because it does not account for the interband optical transitions between d- and s-bands. Possible extensions of the Drude model that account for interband transitions, e.g., the multi oscillator Drude–Lorenz model [46], require a priori unknown parameters, usually extracted from the fitting of a model to optical constants calculated via the computationally demanding DFT-MD approach. Thus, in this work, we use the second methodology, applying Eq. (3.4). We perform an inverse analysis: having various parameterizations for the electron–ion coupling, we calculated T_e and T_a profiles in TTM (3.1) with electron thermal conductivity taken from [23] and fitted the thermoreflectance signal from our recent pump-probe experiment on Ru thin films [19] by varying the coefficients a and b in Eq. (3.4).

We compared three parameterizations for the electron–ion coupling in Ru: T_e- and (T_e, T_a)-dependent couplings as presented in this work, and T_e-dependent coupling calculated by Petrov et al. [23]. Petrov et al.'s work uses a different methodology than ours, which relies on the Eliashberg formalism of the electron–phonon coupling parameter calculation. Their required parameters—the band structure and equilibrium phonon spectrum (spectral function)—are extracted from the density

functional theory calculations. As was discussed in ref. [11], Eliashberg formalism was developed for low-temperature, superconducting conditions, and its extension to high electronic temperatures proposed in ref. [47] and now used in many works including ref. [23] is questionable.

We took a thermoreflectance signal measured on a 30 nm Ru/Si sample irradiated by 85 fs 800 nm laser pulse with 31 mJ/cm2 incident fluence [19]. Under our experimental conditions, the electron temperature change exceeds 4000 K and the atomic temperature change is $\sim 1000\,\mathrm{K}$. Although linear dependence between the reflectance and temperatures, Eq. (3.4), strictly speaking, is only valid at small temperature changes, on the order of a few hundreds of Kelvins, we could still achieve a satisfactory fit to our data in our qualitative analysis using such linear dependence.

The experimental data demonstrated in Fig. 3.6 allow for distinguishing three different processes: (i) The initial rapid increase within 0.5 ps is expected to be associated with the excitation of the electronic system; (ii) The slow increase from $\sim 0.5\,\mathrm{ps}$ up to the maximum at $\sim 3\,\mathrm{ps}$ is the result of the atomic heating via the electron–ion coupling; (iii) The decrease after $\sim 3\,\mathrm{ps}$ is associated with cooling due to heat transport out of the laser-irradiated spot.

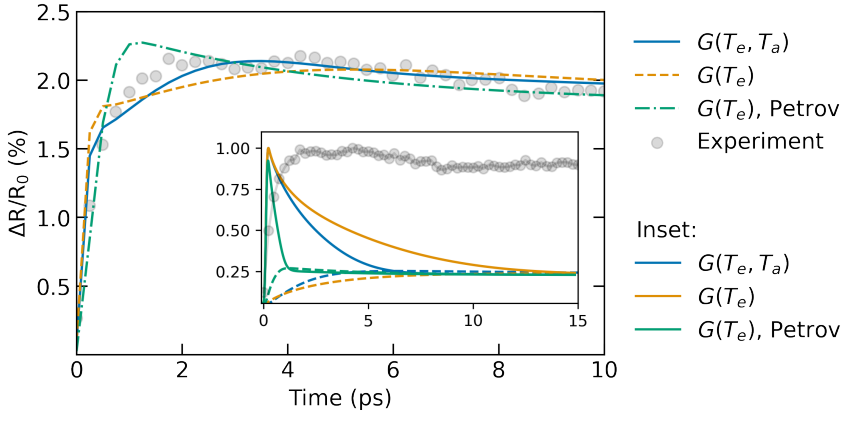

Figure 3.6: Thermoreflectance data fitted by Eq. (3.4). Temperature profiles were calculated using three electron–ion coupling parameterizations: coupling with linear T_a-dependence (3.3) (blue solid line), the same coupling without linear to T_a term (orange dashed line), and T_e-dependent coupling provided by Petrov et al. [23] (green dash-dotted line). The inset shows normalized electronic and atomic temperature profiles calculated with TTM vs thermoreflectance data. Solid lines correspond to T_e, dashed ones to T_a.

Let us point out that the rapid change in the reflectance at $t < 0.5\,\mathrm{ps}$ may be strongly affected by nonequilibrium within the electronic system. In a nonequilibrium state, the electronic system does not adhere to the Fermi–Dirac distribution, and the electronic temperature is ill-defined. This limits the applicability of the TTM and the analysis with the help of Eq. (3.4). We thus focus our analysis on the time window from $\sim 0.5\,\mathrm{ps}$ to 3 ps, where the thermoreflectance change is mainly affected by the atomic temperature and thus the electron–ion coupling.

The results of fitting show that the available couplings do not describe the entire

heat dynamics at the same level of accuracy. Petrov et al.'s coupling can reproduce heat dynamics at timescales ≤ 1 ps due to the very fast equilibration of electronic and atomic temperatures, making fitting insensitive to T_e. In contrast, the coupling $G(T_e, T_a)$ reported in the present work provides a better agreement at longer timescales, from ~ 0.5 ps onwards, during the essential electron–phonon coupling and later cooling. We thus conclude that the calculated electron–phonon coupling $G(T_e, T_a)$ provides the best fitting to the experimental data in the region where TTM is expected to be applicable, which may serve as its qualitative validation.

Unfortunately, the pump-probe thermoreflectance measurements do not allow us to unambiguously conclude which coupling parameterization is more accurate. Although Petrov et al.'s coupling is in good agreement with the experimental coupling measured at room temperature [23], it does not fit well with the data in Fig. 5.6. In contrast, XTANT simulations seem to underestimate coupling at low electronic and atomic temperatures, but, as follows from the provided results, provide a better agreement with the experiment under intermediate excitation. We think this discrepancy is a result of the limited sensitivity of thermoreflectance to the dynamics of the electronic and atomic systems: at the very first ps after the excitation, the probe cannot discriminate a contribution of each system into the signal. We also note here that Petrov et al.'s coupling was previously used to calculate the ablation of Ru in good agreement with the experiment [48].

The definitive answer to the question of which coupling is better may be addressed in experiments probing the dynamics of excited electrons and atoms separately. Such an experiment could be, e.g., a combination of ultrafast electron/X-ray diffraction (probing the atomic system) and optical thermoreflectance spectroscopy or more sensitive EUV absorption spectroscopy (probing the electronic system independently) [49].

3.5 Conclusions

We present calculated electron–phonon coupling parameters in Ru, Pd, and Au as a function of both electronic and atomic temperatures. For all of the considered materials, we demonstrated that the atomic-temperature-dependent coupling has a great impact on the electron–ion relaxation time for equilibrium at intermediate and high absorbed doses. It is, thus, important to take into account the dependence of the coupling parameter on the atomic temperature for reliable simulations.

We also provide a comparison of the electron–phonon coupling in Au and Ru calculated with two different transferrable tight-binding parameterizations. We find that in Au the choice of parameterization plays an important role in electron temperatures below ~ 15 kK, which has implications for the analysis of ultrafast laser–matter interaction experiments.

Finally, we present the analysis of transient thermoreflectance from Ru thin films using different electron–phonon coupling parameterizations and demonstrate that our calculations, with atomic-temperature dependence included, provide a good agreement with the experimental data available. It further emphasizes the importance of accounting for the atomic temperature in calculations of the coupling parameter.

Acknowledgments

Computational resources were supplied by the project "e-Infrastruktura CZ" (e-INFRA LM2018140) provided within the program Projects of Large Research, Development and Innovations Infrastructures.

References

[1] A. Ng, *Outstanding questions in electron–ion energy relaxation, lattice stability, and dielectric function of warm dense matter,* International Journal of Quantum Chemistry **112**, 150 (2012).

[2] B. Rethfeld, D. S. Ivanov, M. E. Garcia, and S. I. Anisimov, *Modelling ultrafast laser ablation,* Journal of Physics D: Applied Physics **50** (2017), 10.1088/1361-6463/50/19/193001.

[3] A. P. Caricato, A. Luches, and M. Martino, *Laser Fabrication of Nanoparticles,* in *Handbook of Nanoparticles* (Springer International Publishing, Cham, 2016) pp. 407–428.

[4] S. I. Ashitkov, N. A. Inogamov, V. V. Zhakhovskii, Y. N. Emirov, M. B. Agranat, I. I. Oleinik, S. I. Anisimov, and V. E. Fortov, *Formation of nanocavities in the surface layer of an aluminum target irradiated by a femtosecond laser pulse,* JETP Letters **95**, 176 (2012).

[5] K. Sugioka and Y. Cheng, *Ultrafast lasers—reliable tools for advanced materials processing,* Light: Science & Applications **3**, e149 (2014).

[6] W. S. Fann, R. Storz, H. W. K. Tom, and J. Bokor, *Electron thermalization in gold,* Physical Review B **46**, 13592 (1992).

[7] B. Rethfeld, A. Kaiser, M. Vicanek, and G. Simon, *Ultrafast dynamics of nonequilibrium electrons in metals under femtosecond laser irradiation,* Physical Review B **65** (2002), 10.1103/PhysRevB.65.214303.

[8] P. Maldonado, T. Chase, A. H. Reid, X. Shen, R. K. Li, K. Carva, T. Payer, M. Horn von Hoegen, K. Sokolowski-Tinten, X. J. Wang, P. M. Oppeneer, and H. A. Dürr, *Tracking the ultrafast nonequilibrium energy flow between electronic and lattice degrees of freedom in crystalline nickel,* Physical Review B **101**, 100302 (2020).

[9] Z. Lin, L. Zhigilei, and V. Celli, *Electron-phonon coupling and electron heat capacity of metals under conditions of strong electron-phonon nonequilibrium,* Physical Review B **77**, 075133 (2008).

[10] Y. V. Petrov, N. A. Inogamov, and K. P. Migdal, *Thermal conductivity and the electron-ion heat transfer coefficient in condensed media with a strongly excited electron subsystem,* JETP Letters **97**, 20 (2013).

[11] N. Medvedev and I. Milov, *Electron-phonon coupling in metals at high electronic temperatures,* Physical Review B **102**, 1 (2020).

[12] S. Anisimov, B. Kapeliovich, and T. Perel-man, *Electron emission from metal surfaces exposed to ultrashort laser pulses,* Journal of Experimental and Theoretical Physics (1974).

[13] L. Waldecker, R. Bertoni, R. Ernstorfer, and J. Vorberger, *Electron-Phonon Coupling and Energy Flow in a Simple Metal beyond the Two-Temperature Approximation,* Physical Review X **6**, 021003 (2016).

[14] P. E. Hopkins, *Influence of inter- and intraband transitions to electron temperature decay in noble metals after short-pulsed laser heating,* Journal of Heat Transfer **132** (2010), 10.1115/1.4002295.

[15] N. Medvedev and I. Milov, *Contribution of inter- and intraband transitions into electron–phonon coupling in metals,* The European Physical Journal D **75**, 212 (2021).

[16] G. Sciaini and R. J. Miller, *Femtosecond electron diffraction: Heralding the era of atomically resolved dynamics,* Reports on Progress in Physics **74** (2011), 10.1088/0034-4885/74/9/096101.

[17] P. M. Kraus, M. Zürch, S. K. Cushing, D. M. Neumark, and S. R. Leone, *The ultrafast X-ray spectroscopic revolution in chemical dynamics,* Nature Reviews Chemistry **2**, 82 (2018).

[18] M. Mo, Z. Chen, and S. Glenzer, *Ultrafast visualization of phase transitions in nonequilibrium warm dense matter,* MRS Bulletin **46**, 694 (2021).

[19] F. Akhmetov, I. Milov, S. Semin, F. Formisano, N. Medvedev, J. M. Sturm, V. V. Zhakhovsky, I. A. Makhotkin, A. Kimel, and M. Ackermann, *Laser-induced electron dynamics and surface modification in ruthenium thin films,* Vacuum **212**, 112045 (2023).

[20] I. Lifshits, M. Kaganov, and L. Tanatarov, *On the theory of radiation-induced changes in metals,* Journal of Nuclear Energy. Part A. Reactor Science **12**, 69 (1960).

[21] W. M. Haynes, *CRC Handbook of Chemistry and Physics, 97th Edition.* (CRC Press LLC Taylor & Francis Group [distributor], Boca Raton; Florence, 2016).

[22] Y. V. Petrov, N. A. Inogamov, K. P. Migdal, and L. D. Landau, *Two-temperature Heat Conductivity of Gold*, Tech. Rep. (L.D. Landau Institute for Theoretical Physics RAS, 2015).

[23] Y. Petrov, K. Migdal, N. Inogamov, V. Khokhlov, D. Ilnitsky, I. Milov, N. Medvedev, V. Lipp, and V. Zhakhovsky, *Ruthenium under ultrafast laser excitation: Model and dataset for equation of state, conductivity, and electron-ion coupling,* Data in Brief **28**, 104980 (2020).

[24] N. Medvedev, V. Tkachenko, V. Lipp, Z. Li, and B. Ziaja, *Various damage mechanisms in carbon and silicon materials under femtosecond X-ray irradiation,* 4open **1**, 3 (2018).

[25] J. C. Tully, *Molecular dynamics with electronic transitions,* The Journal of Chemical Physics **93**, 1061 (1990).

[26] J. C. Tully, *Perspective: Nonadiabatic dynamics theory,* The Journal of Chemical Physics **137** (2012), 10.1063/1.4757762.

[27] M. Mehl and D. Papaconstantopoulos, *NRL Transferable Tight-Binding Parameters Periodic Table,* .

[28] D. A. Papaconstantopoulos and M. J. Mehl, *The Slater Koster tight-binding method: a computationally efficient and accurate approach,* Journal of Physics: Condensed Matter **15**, R413 (2003).

[29] P. Koskinen and V. Mäkinen, *Density-functional tight-binding for beginners,* Computational Materials Science **47**, 237 (2009).

[30] M. J. Mehl, D. A. Papaconstantopoulos, I. I. Mazin, N. C. Bacalis, and W. E. Pickett, *Applications of the NRL tight-binding method to magnetic systems,* Journal of Applied Physics **89**, 6880 (2001).

[31] H. Shi, P. Koskinen, and A. Ramasubramaniam, *Self-Consistent Charge Density-Functional Tight-Binding Parametrization for Pt–Ru Alloys,* The Journal of Physical Chemistry A **121**, 2497 (2017).

[32] J. Frenzel, A. F. Oliveira, N. Jardillier, T. Heine, and G. Seifert, *Semi-relativistic, self-consistent charge Slater-Koster tables for density-functional based tight-binding (DFTB) for materials science simulations,* Zeolites **2**, 2009 (2004).

[33] N. Medvedev, I. Milov, and B. Ziaja, *Structural stability and electron-phonon coupling in two-dimensional carbon allotropes at high electronic and atomic temperatures,* Carbon Trends **5**, 100121 (2021).

[34] W. L. McMillan, *Transition Temperature of Strong-Coupled Superconductors,* Physical Review **167**, 331 (1968).

[35] S. I. Anisimov and B. Rethfeld, *Theory of ultrashort laser pulse interaction with a metal,* (1997) pp. 192–203.

[36] V. Recoules, J. Clérouin, G. Zérah, P. M. Anglade, and S. Mazevet, *Effect of Intense Laser Irradiation on the Lattice Stability of Semiconductors and Metals,* Physical Review Letters **96**, 055503 (2006).

[37] N. Medvedev and I. Milov, *Nonthermal phase transitions in metals,* Scientific Reports **10** (2020), 10.1038/s41598-020-69604-9.

[38] J. M. Molina and T. G. White, *A molecular dynamics study of laser-excited gold,* Matter and Radiation at Extremes **7** (2022), 10.1063/5.0073217.

[39] N. Wetta and J.-C. Pain, *Consistent approach for electrical resistivity within Ziman's theory from solid state to hot dense plasma: Application to aluminum,* Physical Review E **102**, 053209 (2020).

[40] M. Z. Mo, Z. Chen, R. K. Li, M. Dunning, B. B. L. Witte, J. K. Baldwin, L. B. Fletcher, J. B. Kim, A. Ng, R. Redmer, A. H. Reid, P. Shekhar, X. Z. Shen, M. Shen, K. Sokolowski-Tinten, Y. Y. Tsui, Y. Q. Wang, Q. Zheng, X. J. Wang, and S. H. Glenzer, *Heterogeneous to homogeneous melting transition visualized with ultrafast electron diffraction,* Science **360**, 1451 (2018).

[41] M. Z. Mo, Z. Chen, R. K. Li, M. Dunning, B. B. L. Witte, J. K. Baldwin, L. B. Fletcher, J. B. Kim, A. Ng, R. Redmer, A. H. Reid, P. Shekhar, X. Z. Shen, M. Shen, K. Sokolowski-Tinten, Y. Y. Tsui, Y. Q. Wang, Q. Zheng, X. J. Wang, and S. H. Glenzer, *Heterogeneous to homogeneous melting transition visualized with ultrafast electron diffraction.* Science **360**, 1451 (2018).

[42] P. M. Norris, A. P. Caffrey, R. J. Stevens, J. M. Klopf, J. T. McLeskey, and A. N. Smith, *Femtosecond pump-probe nondestructive examination of materials (invited),* Review of Scientific Instruments **74**, 400 (2003).

[43] J. Hohlfeld, S.-S. Wellershoff, J. Güdde, U. Conrad, V. Jähnke, and E. Matthias, *Electron and lattice dynamics following optical excitation of metals,* Chemical Physics **251**, 237 (2000).

[44] J. L. Hostetler, A. N. Smith, D. M. Czajkowsky, and P. M. Norris, *Measurement of the electron-phonon coupling factor dependence on film thickness and grain size in Au, Cr, and Al,* Applied Optics **38**, 3614 (1999).

[45] P. E. Hopkins, J. L. Kassebaum, and P. M. Norris, *Effects of electron scattering at metal-nonmetal interfaces on electron-phonon equilibration in gold films,* Journal of Applied Physics **105** (2009), 10.1063/1.3068476.

[46] E. Silaeva, L. Saddier, and J.-P. Colombier, *Drude–Lorentz Model for Optical Properties of Photoexcited Transition Metals under Electron–Phonon Nonequilibrium,* Applied Sciences **11**, 9902 (2021).

[47] X. Y. Wang, D. M. Riffe, Y.-S. Lee, and M. C. Downer, *Time-resolved electron-temperature measurement in a highly excited gold target using femtosecond thermionic emission,* Physical Review B **50**, 8016 (1994).

[48] I. Milov, V. Zhakhovsky, D. Ilnitsky, K. Migdal, V. Khokhlov, Y. Petrov, N. Inogamov, V. Lipp, N. Medvedev, B. Ziaja, V. Medvedev, I. A. Makhotkin, E. Louis, and F. Bijkerk, *Two-level ablation and damage morphology of Ru films under femtosecond extreme UV irradiation,* Applied Surface Science **528**, 146952 (2020).

[49] M. Volkov, S. A. Sato, F. Schlaepfer, L. Kasmi, N. Hartmann, M. Lucchini, L. Gallmann, A. Rubio, and U. Keller, *Attosecond screening dynamics mediated by electron localization in transition metals,* Nature Physics **15**, 1145 (2019).

4

Electron-phonon coupling in transition metals beyond Wang's approximation

The electron-phonon coupling is the primary mechanism responsible for material relaxation after ultrafast laser irradiation. However, it remains an elusive variable that is extremely challenging to extract experimentally, especially at high electron temperatures. Various previous theoretical approaches to determine electron-phonon coupling demonstrated large degree of inconsistency. In this study, we present a first-principles framework for simulating the electron-phonon coupling parameter based on the electron-phonon spectral function, going beyond the approximation introduced by Wang et al. *[Phys. Rev. B* ***50****, 8016 (1994)]. Our simulations provide electron-temperature-dependent electron-phonon coupling values for transition metals Ru, Pd, and Au. Our findings reveal significant differences between the values obtained from the 'exact' and 'approximated' spectral functions, thus highlighting the limitations of Wang's approximation at elevated electron temperatures.*

4.1 Introduction

Ultrafast laser irradiation has become a standard technique in numerous fields, encompassing various spectroscopy techniques [1, 2], laser structuring [3, 4], medical treatment [5, 6], and more. Despite the routine utilization of ultrafast high-power lasers in fundamental research and industrial applications, the underlying physics of ultrafast light-matter interaction is yet to be fully revealed.

When metal absorbs laser irradiation on a femtosecond timescale, electrons transition to high-energy unoccupied states and subsequently undergo transient relaxation toward a thermal distribution. This gives rise to a highly nonequilibrium situation, where the electron temperature significantly exceeds that of the lattice. That occurs within timescales shorter than the electron-lattice relaxation time, typically ranging from 1 to 10 ps, depending on the material under consideration. The process of electron-lattice relaxation is driven by the electron-phonon interaction.[7, 8].

The simplest yet highly successful model used to describe the evolution of a coupled electron-lattice system under out-of-equilibrium conditions is the famous two-temperature model (TTM). This model was developed by Kaganov *et al.* [9] and later adopted by Anisimov *et al.* [10] for the problems of the ultrafast light-matter interaction. Despite the universally accepted success of TTM in qualitatively describing temperature dynamics in highly excited materials, it may lack quantitative strength, even in the simplest case of ultrafast-heated aluminum [11]. To address the weaknesses of TTM, several different extensions of TTM have been proposed. These include the so-called nonthermal lattice model (NLM) [11], which accounts for the independent coupling of electrons to different phonon modes; nTTM (density + TTM) [12], allowing the tracing of charge carrier generation in semiconductors; and two-temperature molecular dynamics (TTM-MD) [13, 14], which enables the description of possible material transformations on the atomistic level.

At the level of TTM and its successors, the electron-phonon interaction is introduced through the electron-phonon coupling parameter, which establishes the connection between energy exchange and the temperatures of the electrons and lattice. This parameter remains to a large extent unknown, which complicates accurate prediction of the dynamics of ultrafast light-matter interaction. Unfortunately, there is no direct method to measure the electron-phonon coupling at elevated electron and phonon temperatures. State-of-the-art experiments, such as transient optical reflectance measurements [15–18] and ultrafast diffraction techniques [11, 19–21], provide information about either integrated electron or lattice response. However, extracting electron-phonon coupling values from these experiments always involves a certain level of approximation.

From a theoretical perspective, there are several models available to determine the electron-phonon coupling parameter. These models include the nonadiabatic tight-binding approach [22], semi-analytical methods [23], and *ab initio* approaches [24–26] based on the electron-phonon spectral function (Eliashberg function). Among these, the *ab initio* approach has gained significant attention. However, it is important to note that all of these methods often yield noticeably different values for the electron-phonon coupling parameter. For instance, Ref. [24] reports electron-phonon coupling values in aluminum and gold that are approximately one

order of magnitude larger than those derived from the non-adiabatic tight-binding model [22]. Furthermore, no clear evidence exists in favor of one model over the others.

Authors of many studies investigating the electron-phonon coupling at a density functional theory (DFT) level [11, 24], employ an approximation for the Eliashberg function that was introduced by Wang *et al.* [27]. It neglects the dependence of the Eliashberg function on the electronic eigenstates. However, this approximation is rather artificial and is valid primarily at relatively low electron temperatures, potentially leading to an overestimation of the electron-phonon coupling at higher levels of electron excitation. Despite the convenience of the exact formalism and its unified formulation for the interaction of ultrafast laser pulses with metals and materials with a band gap, only a few attempts [25, 26, 28] have been made to go beyond such an approximation.

In this work we follow the formalism of Smirnov [26] and calculate the *ab initio* electron-phonon coupling without relying on the assumptions introduced in Wang's approximation. Unlike Smirnov [26], we do not study thermodynamic properties imposed by the electron-phonon coupling parameter, but we focus more on the analysis of Eliashberg function. Furthermore, our method does not require any custom modifications of the existing DFT codes as it is already implemented within the ABINIT [29] software.

In the following sections, we present the theoretical framework underlying our calculations and emphasize the limitations of Wang's approximation. Next, we report the electron-phonon coupling values for gold as well as two other d-band metals that have received less attention in previous studies: ruthenium and palladium. Through a thorough analysis of the obtained results, we discuss the implications and highlight the reasons why Wang's approximation should be avoided in future research.

4.2 Model

4.2.1 Theory of the electron-phonon coupling

A good starting point for investigating the electron-phonon coupling parameter in solids is the expression for the electron-phonon energy transfer rate. This was derived by Allen [30] from the set of Bloch-Boltzmann-Peierls kinetic equations for electron and phonon distributions:

$$\left(\frac{\partial E_e}{\partial t}\right)_{e-ph} = 4\pi \sum_{k,q,\nu} |g^{\nu}_{k,q}|^2 \omega_{\nu,q} S(k,q,T_e,T_{ph}) \delta(\varepsilon_k - \varepsilon_{k+q} + \omega_q). \tag{4.1}$$

Here, $g^{\nu}_{k,q}$ is the electron-phonon matrix element corresponding to the scattering of a Bloch state with energy ε_k to state ε_{k+q} with the absorption of a phonon with energy ω_q and polarization ν. Also, $S(k,q,T_e,T_{ph})$ is a thermal factor with the form:

$$S(k,q,T_e,T_{ph}) = \left[f(\varepsilon_k,T_e) - f(\varepsilon_{k+q},T_e)\right]\left[n(\omega_q,T_{ph}) - n(\omega_q,T_e)\right],$$

where $f(\varepsilon, T)$ and $n(\omega, T)$ are Fermi and Bose distribution functions, respectively. Hereafter, we use $\hbar = k_B = 1$.

The electron-phonon coupling parameter G_{e-ph} represents the energy transfer rate within the well-known TTM [10]:

$$\left(\frac{\partial E_e}{\partial t}\right)_{e-ph} = G_{e-ph} \cdot (T_{ph} - T_e).$$

Here, G_{e-ph} can be elegantly rewritten in terms of the electron-phonon spectral function, also known as the Eliashberg function α^2F, initially introduced in the Migdal-Eliashberg theory of superconductivity. It demonstrates the effectiveness of phonons in scattering from Bloch state $|\mathbf{k}\rangle$ to $|\mathbf{k}+\mathbf{q}\rangle$ [31]:

$$\alpha^2F(\varepsilon, \varepsilon', \omega) = 2\sum_{k,q,\nu} |g^{\nu}_{k,q}|^2 \delta(\omega - \omega_{\nu,q})\delta(\varepsilon - \varepsilon_k)\delta(\varepsilon - \varepsilon_{k+q}). \tag{4.2}$$

This expression differs from those commonly found in the literature by a factor of $1/N(\varepsilon_F)$, where $N(\varepsilon_F)$ is the electronic density of states (DOS) at the Fermi level. This allows for the application of the Eliashberg function in Eq. (4.2) to the problem of electron-phonon coupling in metals, semiconductors, and insulators. By inserting Eq. (4.2) into Eq. (4.1), we obtain the electron-phonon coupling parameter in the form:

$$G_{e-ph} = \frac{2\pi}{(T_{ph} - T_e)} \int \omega S(\varepsilon, \omega, T_e, T_{ph})\alpha^2F(\varepsilon, \varepsilon+\omega, \omega)d\omega d\varepsilon, \tag{4.3}$$

This reduces the problem to the calculation of the Eliashberg function. Eq. (4.3) does not imply any assumptions about the character of scattering, such as scattering in the close vicinity of the Fermi level, which is valid for metals at low temperatures. Therefore, Eq. (4.3) is rather general and can be used for solids within a wide range of electron temperatures. The only assumptions made are the harmonic nature of ionic motion (phonons) and the Born-Oppenheimer approximation [32].

For the sake of simplicity, authors often apply two approximations for the Eliashberg function. Leveraging the significant difference in the characteristic energy scales of phonons $\omega \sim \omega_D \lesssim 100\,\text{meV}$, and of electrons $\varepsilon \sim \varepsilon_F \sim 1 - 10\,\text{eV}$, one treats ω as a small addition to ε and expands $S(\varepsilon, \omega, T_e, T_{ph})$, $\alpha^2F(\varepsilon, \varepsilon+\omega, \omega)$ up to the first non-vanishing term

$$\begin{aligned} \alpha^2F(\varepsilon, \varepsilon+\omega, \omega) &\approx \alpha^2F(\varepsilon, \varepsilon, \omega), \\ f(\varepsilon+\omega, T_e) &\approx f(\varepsilon, T_e) + \frac{\partial f}{\partial \varepsilon}\omega, \\ S(\varepsilon, \omega, T_e, T_{ph}) &\approx [n(\omega, T_{ph}) - n(\omega, T_e)]\left(-\frac{\partial f}{\partial \varepsilon}\right)\omega. \end{aligned} \tag{4.4}$$

This approximation is rather general and appears to be valid for a wide range of materials. Following Wang *et al.* [27], a further approximation can be made for the Eliashberg function by considering the electron-phonon matrix element to be constant over Bloch states

$$\alpha^2F(\varepsilon, \varepsilon, \omega) \approx \frac{N^2(\varepsilon)}{N^2(\varepsilon_F)}\alpha^2F(\varepsilon_F, \varepsilon_F, \omega) \equiv \frac{N^2(\varepsilon)}{N^2(\varepsilon_F)}\alpha^2F(\omega). \tag{4.5}$$

At high temperatures, the Fermi level must be replaced by the chemical potential $\mu(T_e)$, cf. Eq. (6) in Ref. [33]. Since this approximation assumes a nonzero DOS at the Fermi level $N(\varepsilon_F)$, it can only be applied to metals. Furthermore, its validity should be carefully checked for each metal under consideration.

Eqs. (4.4) and (4.5) yield the well-known expression for the electron-phonon coupling [11, 33, 34], which we will refer as Wang's approximation

$$G_{e-ph} = \frac{2\pi}{(T_{ph} - T_e)} \int \omega^2 \alpha^2 F(\omega) \left[n(\omega, T_{ph}) - n(\omega, T_e) \right] d\omega \times \int \frac{N^2(\varepsilon)}{N^2(\varepsilon_F)} \left(-\frac{\partial f}{\partial \varepsilon} \right) d\varepsilon \tag{4.6}$$

Following Allen [30], this approximation can be further simplified if one considers $\omega_D \ll T_e, T_{ph}$ and expands the Bose distributions inside the integral over ω

$$G_{e-ph} = \pi \lambda \langle \omega^2 \rangle \int \frac{N^2(\varepsilon)}{N(\varepsilon_F)} \left(-\frac{\partial f}{\partial \varepsilon} \right) d\varepsilon \tag{4.7}$$

Here, $\lambda\langle\omega^2\rangle = 2\int \omega\alpha^2F(\omega)/N(\varepsilon_F)d\omega$ is the second moment of the Eliashberg function (we restored $1/N(\varepsilon_F)$ factor to recover proper energy^2 dimensions), and λ is the (dimensionless) electron-phonon coupling strength from the McMillan formula [35]. This value can be extracted from experiments, and hence the electron-phonon coupling parameter can be approximately evaluated with only the knowledge of the electron-temperature-dependent DOS. We provide the latter expression as it is widely used in the community [24, 27, 34].

The Eliashberg functions $\alpha^2F(\varepsilon, \varepsilon', \omega)$ and $\alpha^2F(\omega)$ can be obtained as the output from *ab initio* simulations for every electron temperature T_e and the corresponding electron and phonon band structures. In this work, we calculate the electron-phonon couplings in three different d-band metals, namely, Ru, Pd, and Au, using the exact expression Eq. (4.3). We then compare them to the approximated formula in Eq. (4.6) under conditions typical for ultrafast laser experiments: $T_e \approx 10 - 20\,\mathrm{kK}$. Our calculations reveal that Wang's approximation can deviate significantly from the result obtained with Eq. (4.3) and even lead to nonphysical behavior of G_{e-ph} under certain conditions, as demonstrated below.

4.2.2 Computational details

All *ab initio* calculations were performed using the ABINIT package [29]. The electronic structures of Ru, Pd, and Au were obtained within the PBE parameterization of the generalized gradient approximation for the exchange-correlation functional [36]. We used the scalar-relativistic version of the norm-conserving Vanderbilt pseudopotential [37] taken from the Pseudo Dojo database [38]. The plane wave cutoff was selected to ensure the convergence of electron and phonon DOS values, using the following criterion: the residual DOS values change by less than 1% with further increases in the cutoff value. For the simulations, we used an hcp unit cell for Ru, and fcc unit cells for Pd and Au. The lattice parameters of Ru and Pd were taken from the geometry optimization procedure, whereas for Au we used

the experimental value, which provides better agreement of phonon properties with experimental data. The cutoff and lattice parameter values are provided in Table 4.1. We set the k-point grid to $32 \times 32 \times 32$ points for the self-consistent electron density calculation, and $64 \times 64 \times 64$ for the non-self-consistent calculation of the electron wavefunctions and electron-phonon matrix elements. The self-consistency thresholds were chosen based on the squared wavefunction residual criterion and were $10^{-14}\,\mathrm{Ha}^2$ for electron properties and $10^{-16}\,\mathrm{Ha}^2$ for phonon properties calculation.

Material	E_{cut}(Ha)	Lattice parameter (Bohr)
Ru	40	$a = 5.144$, $c = 8.119$
Pd	40	7.262
Au	80	7.706

Table 4.1: Parameters used in *ab initio* simulations

To obtain the temperature-dependent electron DOS and chemical potential required for Eq. (4.6), we set the Fermi-Dirac smearing for electron populations and ran several simulations for T_e up to 20 kK.

The phonon frequencies and electron-phonon matrix elements were computed within the density functional perturbation theory (DFPT) on an $8 \times 8 \times 8$ q-point grid. The EPH postprocessing tool [39] enabled us to obtain accurate phonon DOS and the Eliashberg function $\alpha^2F(\omega)$ via Fourier interpolation of phonon dynamical matrices and DFPT potentials on a dense q-point grid of $32 \times 32 \times 32$, followed by tetrahedron integration over the Brillouin zone.

The current EPH implementation has several restrictions for the $\alpha^2F(\varepsilon, \varepsilon', \omega)$ calculation: (1) it cannot interpolate matrix elements on a dense q-point grid, (2) it allows only for the Gaussian smearing scheme for Brillouin zone summation, and (3) it supports fixed ϵ, ϵ' grids in a rather narrow window around the Fermi level. The combination of (2) and (3) limits the maximal T_e values for which Eq. (4.3) can be applied because high T_e results in smearing of the Fermi distribution over large energy windows. Stretching the energy window while keeping a fixed number of grid points means that information about some of the Bloch states will be either completely lost (small Gaussian broadening, states are between grid points) or partially yet inaccurately accounted for (large Gaussian broadening, wings of Gaussians are on grid points). To keep the calculation as accurate as possible, we restricted ourselves to a $\pm 12\,\mathrm{eV}$ energy window and a broadening value of $0.272\,\mathrm{eV}$. The chosen energy window is more than sufficient to account for all of the contributing states at $T_e \leq 20\,\mathrm{kK}$.

In the following section, we present the first-principles electron and phonon DOS, phonon band structures, Eliashberg functions, and corresponding electron-phonon coupling parameters. We compare them with available experimental data as well as other theoretical estimations.

4.3 Results

4.3.1 Ru

The calculated electron and phonon properties of Ru are presented in Fig. 4.1. The total electron DOS for different values of T_e agrees well with other calculations [40, 41]. It features a pronounced pseudogap in the vicinity of the Fermi level. As discussed in more detail below, this pseudogap feature explains the weaker values of G_{e-ph} at low T_e than those at high T_e, when more energy levels are involved in scattering on phonons. The thermal excitation of electrons from high DOS below the Fermi level to a lower one results in a positive shift of the chemical potential with increasing T_e (Fig. 4.1(b)).

The calculated phonon band structure and phonon DOS (Fig. 4.1(c)) are in a very good agreement with the experimental data [42], validating the parameters chosen for the DFPT simulations. The shape of Eliashberg function $\alpha^2F(\omega)$ is very similar to the shape of the phonon DOS, with slightly higher peaks $\leq\sim 25$ meV. From the phonon dispersion curve in Fig. 4.1(c), one can see that this energy range corresponds to acoustic branches. From this, we conclude that electrons tend to couple more strongly to acoustic phonons in Ru.

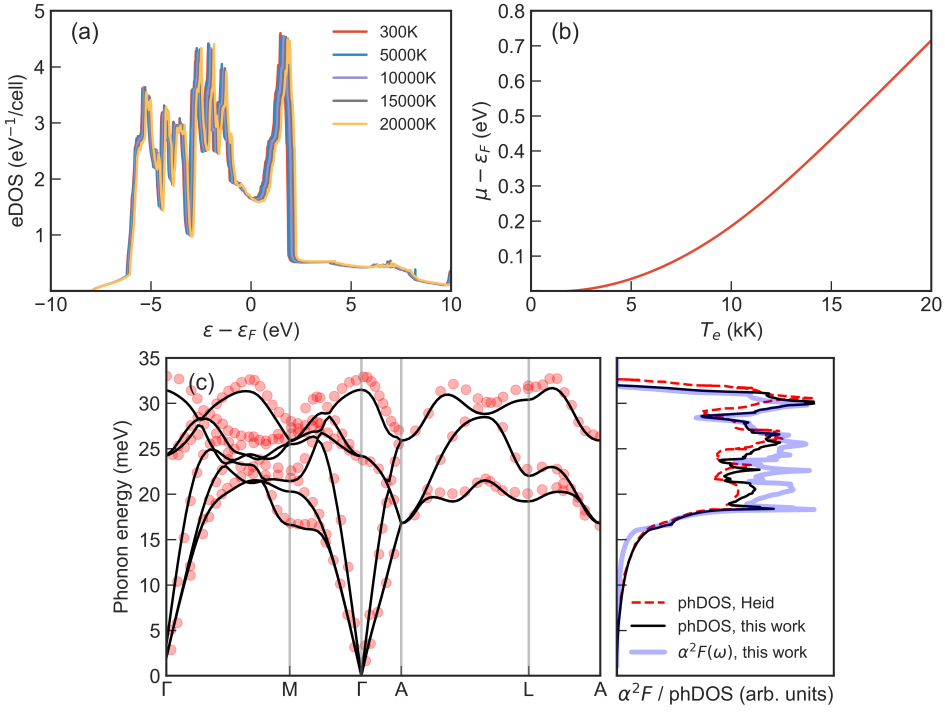

Figure 4.1: (a) The electron DOS of Ru obtained for different values of T_e. (b) The chemical potential of Ru as a function of T_e. (c) The phonon band structure, phonon DOS and the Eliashberg function $\alpha^2F(\omega)$ of Ru. The red dots are neutron scattering data, and the red dashed line is the theoretical DOS taken from Ref. [42].

The full energy-dependent Eliashberg function $\alpha^2F(\varepsilon,\varepsilon',\omega)$ is presented in Fig. 4.2. In the case of Ru, it qualitatively resembles a direct product of the electron DOS and $\alpha^2F(\omega)$, which confirms the assumptions of Wang's approximation. However, contrary to the shape of $N(\varepsilon)$, there is a pronounced asymmetry in the peak intensity below and above the Fermi level. The scattering to or from energy states above the Fermi level contributes considerably less to G_{e-ph} than expected in Wang's approximation.

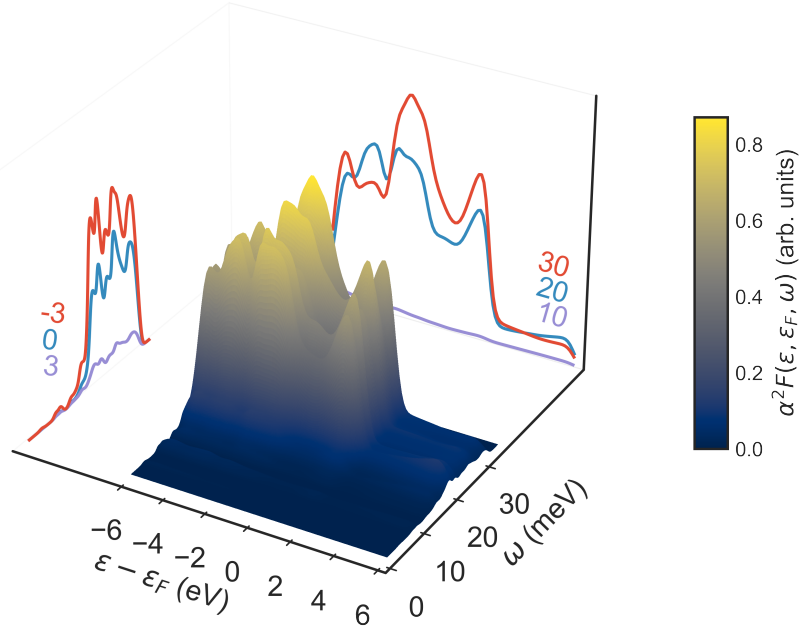

Figure 4.2: The electron-energy-resolved Eliashberg function $\alpha^2F(\varepsilon,\varepsilon_F,\omega)$ of Ru. The contour projections on ω and ϵ axes are drawn for clarity (red, blue and purple lines), numbers indicate $\varepsilon-\varepsilon_F$ or ω values at which projections were made.

Using the calculated Eliashberg functions, we obtained G_{e-ph} values using Eqs.(4.3) and (4.6) and compared them with various theoretical and experimental results (see Fig.4.3). At low T_e, Eqs. (4.3) and (4.6) yield identical coupling, as expected, since only the Bloch states very close to the Fermi level scatter on phonons. With increasing T_e, the smearing Fermi distribution involves more and more Bloch states above ε_F in electron-phonon scattering. As we have already pointed out, due to the weaker coupling of those states to phonons compared with Wang's approximation of a constant matrix element (cf. Fig. 4.1(a) and projections to the ε axis in Fig. 4.2), the exact expression in Eq. (4.3) provides noticeably lower G_{e-ph} values at high T_e.

The low-temperature limit of our G_{e-ph} values is in qualitative agreement with available experimental data. The work of Petrov *et al.* [41] uses a two-parabolic

approximation for the electron DOS as well as Lindhard screening for the electron-ion interaction, assuming free-electron-gas-like behavior. These assumptions seem to be valid at high T_e, providing satisfactory agreement with G_{e-ph} calculated via the exact expression in Eq. (4.3). However, the low-temperature values reported inRef. [41] may be overestimated. Finally, the recently published G_{e-ph} values calculated within the nonadiabatic tight-binding – molecular dynamic (TBMD) formalism [22, 43] are an order of magnitude lower. We anticipated such a discrepancy due to: (i) the known lack of TBMD's predictive power at low electron temperatures, and (ii) the overall divergence between TBMD- and DFT-based approaches for transition metals with half-filled d bands, the origin of which is yet to be analyzed [22].

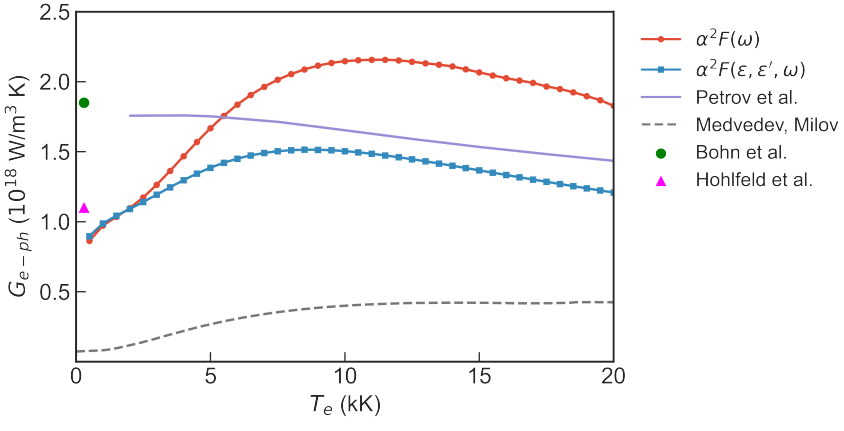

Figure 4.3: Electron-phonon coupling parameter G_{e-ph} in Ru as a function of electron temperature T_e obtained via the exact expression in Eq. (4.3) (blue) and within the Wang's approximation in Eq. (4.6) (red). The results are compared with other theoretical data of Petrov *et al.* [41] and Medvedev and Milov [22] as well as experimental estimates by Bohn *et al.* [44] and Hohlfeld *et al.* [15].

4.3.2 Pd

Fig. 4.4 presents the electron and phonon properties of Pd. The major difference compared with Ru is that the electrons occupy almost the entire d band, and the Fermi level lies on the sharp edge of the d-band DOS. This means that the electrons can be easily thermally excited, leading to a quite significant positive shift of the chemical potential. The phonon band structure and DOS agree less with available neutron scattering data [45] than those of Ru, but they are still sufficiently accurate. The spectral function has a noticeably higher intensity in the range 10-20 meV than the phonon DOS. In this region, DOS and Eliashberg function are formed by both longitudinal and transverse mode contributions as follows from Fig. 4.4(c) (transverse modes in Pd have a small slope around the Γ-point). On the contrary, the peak-like region in the range $25 - 30$ meV belongs only to longitudinal modes. This asymmetry of the spectral function may suggest that the electrons in Pd prefer

to couple with transverse acoustic phonons rather than longitudinal ones.

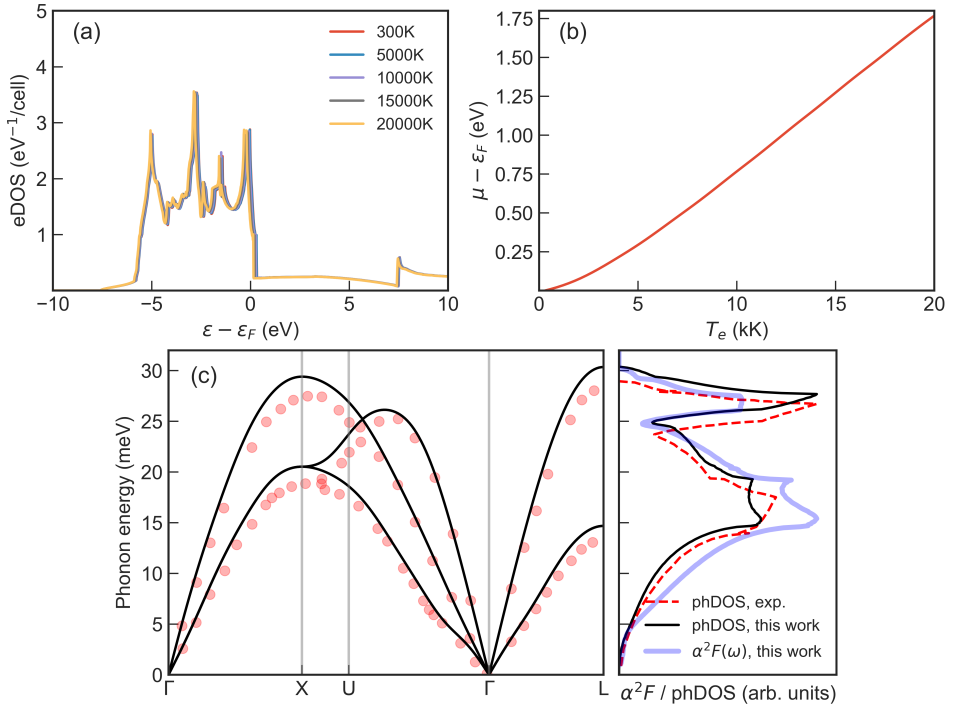

Figure 4.4: Same as Fig. 4.1 but for Pd. The experimental data in (c) are taken from Refs. [45, 46].

The electron-energy-dependent spectral function of Pd, shown in Fig. 4.5, differs quite significantly from the case of Ru, cf. Fig. 4.2. It no longer resembles a direct product of $N(\varepsilon)$ and $\alpha^2F(\omega)$, indicating that the underlying assumptions of Wang's approximation are not applicable for Pd. A careful investigation of the (ε, ω) surface reveals that the Bloch states below the Fermi level are primarily coupled to transverse modes ($\omega \lesssim 20\,\text{meV}$), while the states around the Fermi level tend to couple to longitudinal modes (peak at $\omega \approx 30\,\text{meV}$).

The comparative analysis of the electron-phonon coupling parameter in Pd calculated via Eqs.(4.3) and (4.6) and presented in Fig. 4.6(a) requires careful attention. First, as it has been pointed out by Smirnov [26], for a Pt metal having very similar band structure, the G_{e-ph} within Wang's approximation decays faster than the exact expression due to the drastic decrease of contribution of d-band electrons with increasing T_e (cf. Fig. 11 in Ref. [26]). Second, many authors [24, 34] calculate the coupling via the expression in Eq. (4.7), placing DOS values at the Fermi level in the denominator in the integral over ε. However, the use of $N(\varepsilon_F)$ at high T_e is somewhat questionable since the electron-phonon scattering involves states around μ. Hence, one should replace $N^2(\varepsilon_F)$ with $N^2(\mu)$ in the denominator of Eq. (4.6). In many metals with flat DOS in the vicinity of the Fermi level, such a replacement causes only minor changes. In contrast, in Ni, Pd, and Pt, the Fermi level is lo-

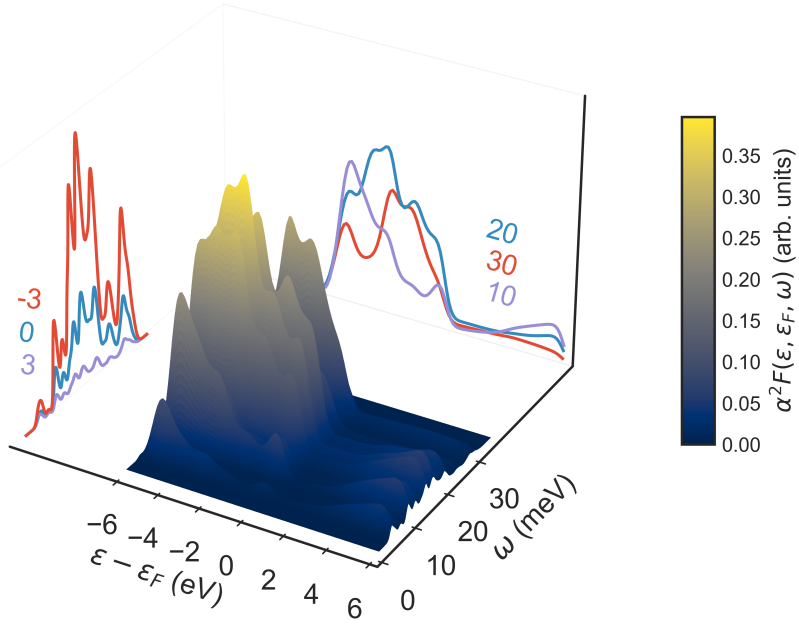

Figure 4.5: Same as Fig. 4.2 but for Pd.

cated on the sharp edge of the d-band, and even a minor increase of T_e yields a dramatic increase of inverse DOS $N^{-1}(\mu)$, see Fig. 4.6(b). As a direct consequence, G_{e-ph} has a similar increase, which we consider to be nonphysical (Fig. 4.6(a), red line). The exact expression in Eq. (4.3) is free from ambiguity in the choice of the "proper" denominator. The calculated coupling parameter behaves smoothly and qualitatively resembles the coupling of Smirnov [26] for Pt.

One may note that the anticipated agreement of our G_{e-ph} values at low T_e does not hold in Pd. This is due to the use of the Gaussian smearing scheme for $\alpha^2F(\varepsilon, \varepsilon', \omega)$, which weakens the contribution from scattering around the d-band edge more than it should.

The G_{e-ph} values calculated with $N^2(\varepsilon_F)$ in Eq. (4.6) align very well with Ref. [34], as they use the same underlying approximations. At high T_e, when the contribution of d-electrons decreases, they overlap with the TBMD-obtained coupling parameter [22, 43]. Based on this observation, we could speculate that either TBMD underestimates the contribution of d-band states to the coupling, or DFT overestimates it.

4.3.3 Au

The electron and phonon properties of gold used in the calculations of the electron-phonon coupling parameter are presented in Fig. 4.7. The behavior of the T_e-

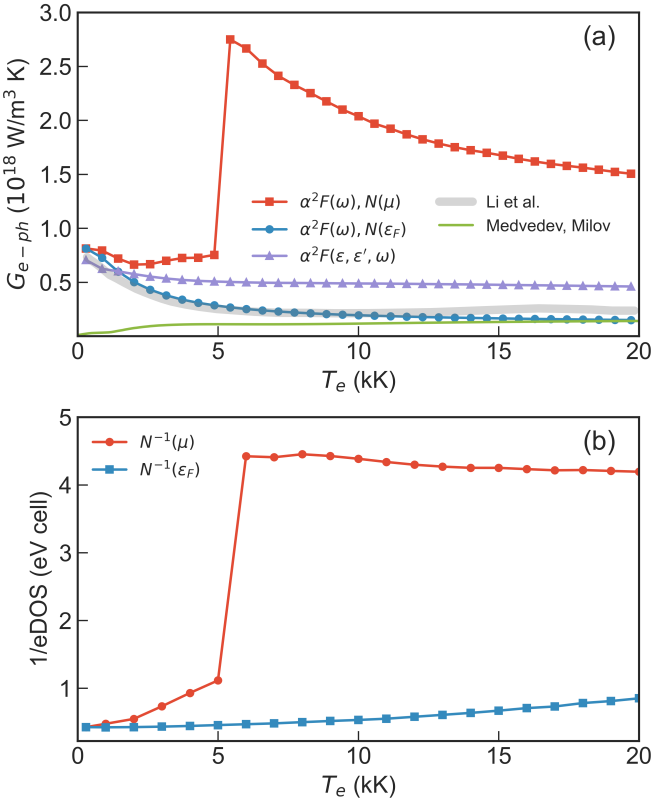

Figure 4.6: (a) Electron-phonon coupling parameter G_{e-ph} in Pd as a function of electron temperature T_e obtained via the exact expression in Eq. (4.3) (purple) and within the Wang's approximation in Eq. (4.6) with electron DOS values taken at the Fermi level $N(\varepsilon_F)$ (blue) and the temperature-dependent chemical potential $N(\mu)$ (red). The results are compared with simulations of Li *et al.* [34] and Medvedev and Milov [22]. (b) The dependence of $N^{-1}(\varepsilon_F)$ (blue) and $N^{-1}(\mu)$ (red) on T_e.

dependent electron DOS and chemical potential is typical for noble metals and aligns well with previous reports [24, 47]. The obtained phonon band structure agrees well with available neutron scattering data. Like in Pd, another fcc metal, electrons in Au tend to couple more strongly to transverse phonons (cf. Fig. 4.7 (c), black and blue lines).

With the full $\alpha^2F(\varepsilon, \varepsilon', \omega)$ surface, we can assess the applicability of Wang's approximation in gold. Like Section 4.3.1, the spectral function is overall close to the direct product of $N(\varepsilon)$ and $\alpha^2F(\omega)$. However, electron states below the Fermi level seem to couple more weakly to several phonon modes, smearing out the peak-like shape (see, e.g., region $\omega \approx 5\,\text{meV}$, $-6\,\text{eV} \geq \varepsilon - \varepsilon_F \leq -4\,\text{eV}$). Therefore, with increasing T_e and smearing of the Fermi distribution, these states start to contribute to G_{e-ph}, and we expect a deviation between the exact coupling parameter and Wang's approximation (see Fig.4.8).

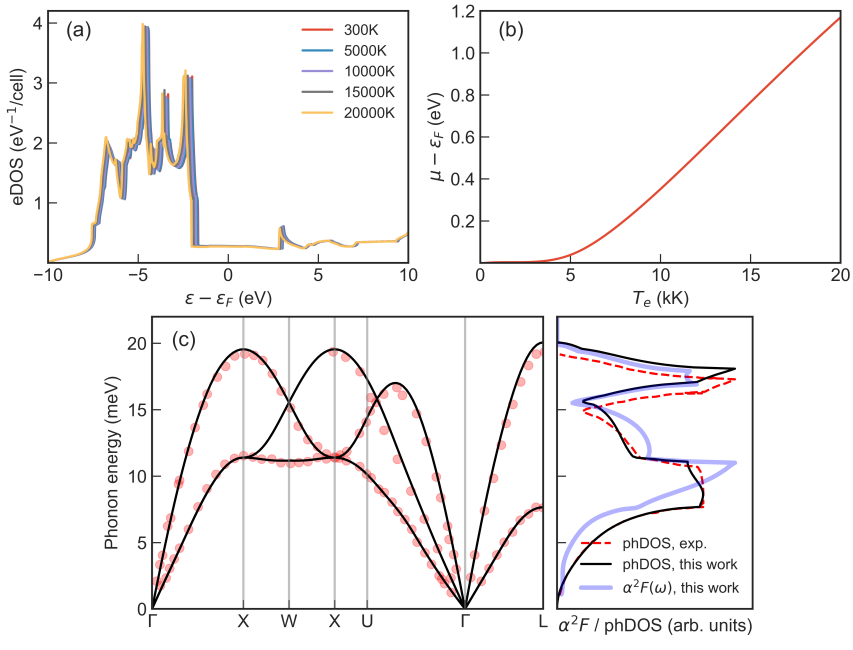

Figure 4.7: Same as Fig. 4.1 but for Au. The experimental data in (c) are taken from Ref. [45].

Fig. 4.9 displays the electron-phonon coupling parameter in Au, compared with numerous other theoretical works as well as several experimental data at low T_e. Although many other low-temperature experimental values for G_{e-ph} exist (cf. Refs. [22, 51–55]), they are very close to each other and to the shown points of Hohlfeld [15] and Sokolowski-Tinten [49], and hence, we decided not to depict them explicitly. The G_{e-ph} values obtained within Wang's approximation in Eq. (4.6) agree satisfactorily with the results of Li *et al.* [34], calculated via Eq. (4.7). The slight difference may stem from different coupling strengths: $\lambda\langle\omega^2\rangle = 21.5\,\mathrm{meV}^2$ by Li *et al.* [34] and $\lambda\langle\omega^2\rangle = 19.2\,\mathrm{meV}^2$ in this work.

As discussed above, although $\alpha^2F(\varepsilon,\varepsilon',\omega)$ in Au is close to Wang's approximation, the electron-phonon coupling parameter calculated with the exact expression increases more slowly with temperature. The G_{e-ph} based on $\alpha^2F(\varepsilon,\varepsilon',\omega)$ largely reproduces the results of Smirnov [26] and Brown *et al.* [25], who also use the exact formula in Eq. (4.3), which validates our results as well as the $\alpha^2F(\varepsilon,\varepsilon',\omega)$ produced by the EPH postprocessor for the ABINIT package.

The low-T_e G_{e-ph} data obtained from TBMD simulations [43] are in satisfactory agreement with present simulations in the case of NRL parameterization yet noticeably lower in the case of DFTB parameterization. When T_e increases, a situation directly opposite to Pd is observed: d-band states start to contribute in electron-phonon scattering resulting in a significant deviation of TBMD data from *ab initio* results. This is an additional confirmation of the speculation made above: the TBMD approach seems to underestimate the contribution of d-band electrons

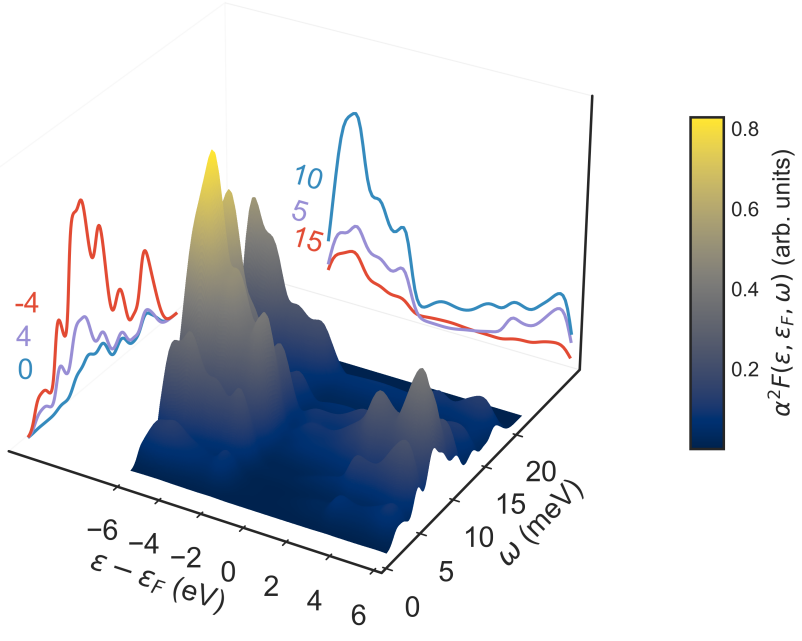

Figure 4.8: Same as Fig. 4.2 but for Au.

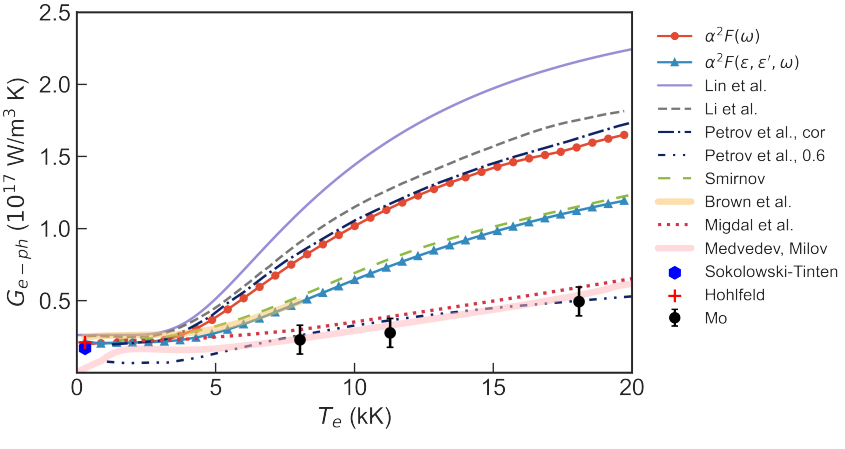

Figure 4.9: Electron-phonon coupling parameter G_{e-ph} in Au as a function of electron temperature T_e obtained via the exact expression in Eq. (4.3) (blue) and within the Wang's approximation in Eq. (4.6) (red). Theoretical results to compare with are taken from Lin *et al.* [24], Li *et al.* [34], Petrov *et al.* [23] (both cor and 0.6, see Fig. 6 there), Smirnov [26], Brown *et al.* [25], Migdal *et al.* [48], Medvedev and Milov [22]; experimental points are from Sokolowski-Tinten *et al.* [49], Hohlfeld *et al.* [15], and Mo *et al.* [50].

to G_{e-ph} in respect to DFT. However, we shall make a point that the results of Petrov *et al.* (Petrov et al., 0.6) [23] and Migdal *et al.* [48], both based on two-parabolic approximation and Lindhard dielectric screening, agree with the TBMD data. Let us discuss this agreement in detail.

The electron-phonon matrix elements, $g^{\nu}_{k,q}$, represent matrix elements of the electron-ion potential. Naturally, the most suitable form for this potential is the bare electron-nucleus Coulomb interaction screened by the dielectric function. It is very difficult to obtain an accurate dielectric function; one usually restricts oneself to lowest order of perturbation theory and uses the dielectric function within the random-phase approximation (RPA). That is exactly how the electron-phonon matrix elements were calculated in Refs. [23, 48] since the Lindhard function they have used is the simplest kind of RPA, and it is known to overestimate dielectric screening, resulting in weaker electron-phonon coupling.

In contrast, the electron-phonon matrix elements in DFPT involve derivatives of the self-consistent Kohn-Sham potential with respect to phonon wavevector $\mathbf{q}$. As discussed by Giustino [32], the DFPT scheme is equivalent to screening the Coulomb interaction using a RPA + xc level dielectric function, which incorporates local-field corrections originating from exchange and correlation (xc) effects. It is widely accepted that such an RPA + xc dielectric function provides a more accurate approximation.

Surprisingly, a simple rescaling of Petrov's coupling to the experimental electron-phonon coupling constant (Petrov et al., cor) yields the same values as our DFPT-based simulations. This suggests that the rescaling can be interpreted as the renormalization of the dielectric function to incorporate band structure as well as local-field effects. The noble nature of gold (electron-gas-like behavior of conduction band electrons) may be the reason why such a simple rescaling recovers proper RPA + xc based on Bloch states obtained from DFT.

We also highlight the recent experiment by Mo *et al.* [50] on ultrafast electron diffraction measurement of melting in thin gold films. The observed melting dynamics and energy threshold for the transition between heterogeneous and homogeneous melting regimes suggest a T_e-dependent G_{e-ph}, like those reported in [22, 43, 48]. However, the measurements of the experiment were fitted using constant G_{e-ph} values corresponding to different absorbed energy density regimes, which do not fully reflect the dynamics of electron-lattice energy exchange. Therefore, the values of electron-phonon coupling extracted from this experiment should be considered as an effective coupling parameter for each absorbed energy density, and not as T_e-dependent G_{e-ph}. A more rigorous two-temperature analysis by Smirnov [26] was able to reproduce the dynamics of homogeneous melting but struggled with partial or heterogeneous melting regimes. Furthermore, a more advanced TTM-MD analysis [56] suggested that the experimentally observed dynamics cannot be reproduced using any reasonable model for the electron-phonon coupling parameter. Therefore, the high-T_e experimental points should be used for validation of theoretical models only with great caution.

4.4 Conclusion

We conducted first-principles simulations of the electron-phonon coupling parameter G_{e-ph} in transition metals based on Allen's [30] theory of thermal relaxation in the coupled electron-phonon system. We calculated the electron-energy-dependent Eliashberg functions entering the exact expression for G_{e-ph}. However, the accuracy of the underlying theory is limited by (i) the formal accuracy of the Boltzmann equation, (ii) the Born-Oppenheimer approximation and the phonon picture, and (iii) certain approximations imposed by the DFT framework, such as the accuracy of the chosen exchange-correlation functional and numerical parameters. We evaluated these Eliashberg functions in the low-temperature limit, as they show minor temperature dependence in the range of $T_e \leq 20\,\mathrm{kK}$ considered here. Nonetheless, for higher T_e values, the evaluation of the Eliashberg functions for each temperature is necessary, as follows from Ref. [33].

The obtained Eliashberg functions for d-band metals, specifically Ru, Pd, and Au, were analyzed in detail to determine the materials and conditions under which they can be approximated by Wang's expression in Eq. (4.5). The values of G_{e-ph} for Ru, Pd, and Au were compared with experimental data as well as previous theoretical simulations that employed various approximations. These approximations included semi-analytical expressions, the non-adiabatic tight-binding molecular dynamics (TBMD) approach, the standard Wang's approximation and the variations of the exact theory that do not involve any approximations for the Eliashberg function.

Our findings indicate that the DFT-based electron-phonon coupling values are consistently higher than TBMD values. Based on the analysis of the high-T_e behavior of coupling, we attribute this divergence to the underestimation of the contribution of d-band states to the electron-phonon coupling in TBMD. We also showed that Wang's approximation does not accurately account for the coupling between different electron states and different phonon modes, resulting in larger G_{e-ph} values in the case of Ru and Au, and weaker in the case of Pd.

The agreement of our results obtained for Au with previous works [25, 26] validates the method of the Eliashberg function calculation provided by the EPH tool (part of the ABINIT simulation package [29]). This means that specialists in material science and condensed matter physics have a ready-to-use tool for accurate simulations of the electron-phonon coupling parameter, which is seamlessly applicable for metals, semiconductors, and dielectrics.

Acknowledgments

Author thanks SURF (www.surf.nl) for the support in using the National Supercomputer Snellius.

References

[1] M. Maiuri, M. Garavelli, and G. Cerullo, *Ultrafast Spectroscopy: State of the Art and Open Challenges,* Journal of the American Chemical Society **142**, 3 (2020).

[2] A. Kirilyuk, A. V. Kimel, and T. Rasing, *Ultrafast optical manipulation of magnetic order,* Reviews of Modern Physics **82**, 2731 (2010).

[3] A. P. Caricato, A. Luches, and M. Martino, *Laser Fabrication of Nanoparticles,* in *Handbook of Nanoparticles* (Springer International Publishing, Cham, 2016) pp. 407–428.

[4] K. Sugioka and Y. Cheng, *Ultrafast lasers—reliable tools for advanced materials processing,* Light: Science & Applications **3**, e149 (2014).

[5] H. Lubatschowski, A. Heisterkamp, F. Will, A. I. Singh, J. Serbin, A. Ostendorf, O. Kermani, R. Heermann, H. Welling, and W. Ertmer, *Medical and biological applications for ultrafast laser pulses,* Third International Symposium on Laser Precision Microfabrication **4830**, 537 (2003).

[6] C. L. Hoy, O. Ferhanoğlu, M. Yildirim, K. H. Kim, S. S. Karajanagi, K. M. C. Chan, J. B. Kobler, S. M. Zeitels, and A. Ben-Yakar, *Clinical ultrafast laser surgery: Recent advances and future directions,* IEEE Journal on Selected Topics in Quantum Electronics **20** (2014), 10.1109/JSTQE.2013.2287098.

[7] B. Rethfeld, K. Sokolowski-Tinten, D. Von Der Linde, and S. I. Anisimov, *Timescales in the response of materials to femtosecond laser excitation,* Applied Physics A: Materials Science and Processing **79**, 767 (2004).

[8] B. Rethfeld, D. S. Ivanov, M. E. Garcia, and S. I. Anisimov, *Modelling ultrafast laser ablation,* Journal of Physics D: Applied Physics **50**, 193001 (2017).

[9] M. I. Kaganov, I. M. Lifshitz, and L. V. Tanatarov, *Relaxation between electrons and crystalline lattice,* Sov. Phys. JETP **4**, 173 (1957).

[10] S. Anisimov, B. Kapeliovich, and T. Perel'man, *Electron emission from metal surfaces exposed to ultrashort laser pulses,* Journal of Experimental and Theoretical Physics **66**, 375 (1974).

[11] L. Waldecker, R. Bertoni, R. Ernstorfer, and J. Vorberger, *Electron-Phonon Coupling and Energy Flow in a Simple Metal beyond the Two-Temperature Approximation,* Physical Review X **6**, 021003 (2016).

[12] H. M. van Driel, *Kinetics of high-density plasmas generated in Si by 1.06- and 0.53- μ picosecond laser pulses,* Physical Review B **35**, 8166 (1987).

[13] D. Ivanov and L. Zhigilei, *Combined atomistic-continuum modeling of short-pulse laser melting and disintegration of metal films,* Physical Review B - Condensed Matter and Materials Physics **68** (2003), 10.1103/PhysRevB.68.064114.

[14] D. M. Duffy and A. M. Rutherford, *Including the effects of electronic stopping and electron-ion interactions in radiation damage simulations,* Journal of Physics Condensed Matter **19** (2007), 10.1088/0953-8984/19/1/016207.

[15] J. Hohlfeld, S.-S. Wellershoff, J. Güdde, U. Conrad, V. Jähnke, and E. Matthias, *Electron and lattice dynamics following optical excitation of metals,* Chemical Physics **251**, 237 (2000).

[16] P. M. Norris, A. P. Caffrey, R. J. Stevens, J. M. Klopf, J. T. McLeskey, and A. N. Smith, *Femtosecond pump-probe nondestructive examination of materials (invited),* Review of Scientific Instruments **74**, 400 (2003).

[17] P. E. Hopkins and P. M. Norris, *Substrate influence in electron-phonon coupling measurements in thin Au films,* Applied Surface Science **253**, 6289 (2007).

[18] J. L. Hostetler, A. N. Smith, D. M. Czajkowsky, and P. M. Norris, *Measurement of the electron-phonon coupling factor dependence on film thickness and grain size in Au, Cr, and Al,* Applied Optics **38**, 3614 (1999).

[19] G. Sciaini and R. J. Miller, *Femtosecond electron diffraction: Heralding the era of atomically resolved dynamics,* Reports on Progress in Physics **74** (2011), 10.1088/0034-4885/74/9/096101.

[20] P. M. Kraus, M. Zürch, S. K. Cushing, D. M. Neumark, and S. R. Leone, *The ultrafast X-ray spectroscopic revolution in chemical dynamics,* Nature Reviews Chemistry **2**, 82 (2018).

[21] M. Mo, Z. Chen, and S. Glenzer, *Ultrafast visualization of phase transitions in nonequilibrium warm dense matter,* MRS Bulletin **46**, 694 (2021).

[22] N. Medvedev and I. Milov, *Electron-phonon coupling in metals at high electronic temperatures,* Physical Review B **102**, 064302 (2020).

[23] V. Y. Petrov, N. A. Inogamov, and K. P. Migdal, *Thermal conductivity and the electron-ion heat transfer coefficient in condensed media with a strongly excited electron subsystem,* JETP Letters **97**, 20 (2013).

[24] Z. Lin, L. Zhigilei, and V. Celli, *Electron-phonon coupling and electron heat capacity of metals under conditions of strong electron-phonon nonequilibrium,* Physical Review B **77**, 075133 (2008).

[25] A. M. Brown, R. Sundararaman, P. Narang, W. A. Goddard, and H. A. Atwater, *Ab initio phonon coupling and optical response of hot electrons in plasmonic metals,* Physical Review B **94**, 075120 (2016).

[26] N. A. Smirnov, *Copper, gold, and platinum under femtosecond irradiation: Results of first-principles calculations,* Physical Review B **101**, 1 (2020).

[27] X. Y. Wang, D. M. Riffe, Y.-S. Lee, and M. C. Downer, *Time-resolved electron-temperature measurement in a highly excited gold target using femtosecond thermionic emission,* Physical Review B **50**, 8016 (1994).

[28] B. Arnaud and Y. Giret, *Electron Cooling and Debye-Waller Effect in Photoexcited Bismuth,* Physical Review Letters **110**, 16405 (2013).

[29] X. Gonze, B. Amadon, G. Antonius, F. Arnardi, L. Baguet, J. M. Beuken, J. Bieder, F. Bottin, J. Bouchet, E. Bousquet, N. Brouwer, F. Bruneval, G. Brunin, T. Cavignac, J. B. Charraud, W. Chen, M. Côté, S. Cottenier, J. Denier, G. Geneste, P. Ghosez, M. Giantomassi, Y. Gillet, O. Gingras, D. R. Hamann, G. Hautier, X. He, N. Helbig, N. Holzwarth, Y. Jia, F. Jollet, W. Lafargue-Dit-Hauret, K. Lejaeghere, M. A. Marques, A. Martin, C. Martins, H. P. Miranda, F. Naccarato, K. Persson, G. Petretto, V. Planes, Y. Pouillon, S. Prokhorenko, F. Ricci, G. M. Rignanese, A. H. Romero, M. M. Schmitt, M. Torrent, M. J. van Setten, B. Van Troeye, M. J. Verstraete, G. Zérah, and J. W. Zwanziger, *The ABINITproject: Impact, environment and recent developments,* Computer Physics Communications **248** (2020), 10.1016/j.cpc.2019.107042.

[30] P. B. Allen, *Theory of thermal relaxation of electrons in metals,* Physical Review Letters **59**, 1460 (1987).

[31] P. B. Allen and B. Mitrović, *Theory of Superconducting Tc,* Solid State Physics - Advances in Research and Applications **37**, 1 (1983).

[32] F. Giustino, *Electron-phonon interactions from first principles,* Reviews of Modern Physics **89**, 15003 (2017).

[33] J. Zhang, R. Qin, W. Zhu, and J. Vorberger, *Energy Relaxation and Electron–Phonon Coupling in Laser-Excited Metals,* Materials **15**, 1 (2022).

[34] Y. Li and P. Ji, *Ab initio calculation of electron temperature dependent electron heat capacity and electron-phonon coupling factor of noble metals,* Computational Materials Science **202**, 1 (2022).

[35] W. L. McMillan, *Transition Temperature of Strong-Coupled Superconductors,* Physical Review **167**, 331 (1968).

[36] J. P. Perdew, K. Burke, and M. Ernzerhof, *Generalized Gradient Approximation Made Simple,* Physical Review Letters **77**, 3865 (1996).

[37] D. R. Hamann, *Optimized norm-conserving Vanderbilt pseudopotentials,* Physical Review B - Condensed Matter and Materials Physics **88**, 1 (2013).

[38] M. J. van Setten, M. Giantomassi, E. Bousquet, M. J. Verstraete, D. R. Hamann, X. Gonze, and G. M. Rignanese, *The PSEUDODOJO: Training and grading a 85 element optimized norm-conserving pseudopotential table,* Computer Physics Communications **226**, 39 (2018).

[39] G. Brunin, H. P. C. Miranda, M. Giantomassi, M. Royo, M. Stengel, M. J. Verstraete, X. Gonze, G. M. Rignanese, and G. Hautier, *Phonon-limited electron mobility in Si, GaAs, and GaP with exact treatment of dynamical quadrupoles,* Physical Review B **102**, 94308 (2020).

[40] A. V. Lugovskoy, M. P. Belov, O. M. Krasilnikov, and Y. K. Vekilov, *Stability of the hcp Ruthenium at high pressures from first principles,* Journal of Applied Physics **116** (2014), 10.1063/1.4894167.

[41] Y. Petrov, K. Migdal, N. Inogamov, V. Khokhlov, D. Ilnitsky, I. Milov, N. Medvedev, V. Lipp, and V. Zhakhovsky, *Ruthenium under ultrafast laser excitation: Model and dataset for equation of state, conductivity, and electron-ion coupling,* Data in Brief **28**, 104980 (2020).

[42] R. Heid and L. Pintschovius, *Anomalous lattice dynamics of ruthenium,* Physical Review B - Condensed Matter and Materials Physics **61**, 12059 (2000).

[43] F. Akhmetov, N. Medvedev, I. Makhotkin, M. Ackermann, and I. Milov, *Effect of Atomic-Temperature Dependence of the Electron–Phonon Coupling in Two-Temperature Model,* Materials **15**, 5193 (2022).

[44] M. Bonn, D. N. Denzler, S. Funk, M. Wolf, S.-S. Wellershoff, and J. Hohlfeld, *Ultrafast electron dynamics at metal surfaces: Competition between electron-phonon coupling and hot-electron transport,* Physical Review B **61**, 1101 (2000).

[45] P. H. Dederichs, H. Schober, and D. J. Sellmyer, *Phonon States of Elements. Electron States and Fermi Surfaces of Alloys / Phononenzustände von Elementen. Elektronenzustände und Fermiflächen von Legierungen*, Landolt-Börnstein: Numerical Data and Functional Relationships in Science and Technology - New Series (Springer Berlin Heidelberg, 1981).

[46] S. S. Setayandeh, C. J. Webb, and E. M. Gray, *Progress in Solid State Chemistry Electron and phonon band structures of palladium and palladium hydride : A review,* Progress in Solid State Chemistry **60**, 100285 (2020).

[47] E. Bévillon, J. P. Colombier, V. Recoules, and R. Stoian, *Free-electron properties of metals under ultrafast laser-induced electron-phonon nonequilibrium: A first-principles study,* Physical Review B - Condensed Matter and Materials Physics **89**, 1 (2014).

[48] K. P. Migdal, D. K. Il'Nitsky, Y. V. Petrov, and N. A. Inogamov, *Equations of state, energy transport and two-temperature hydrodynamic simulations for femtosecond laser irradiated copper and gold,* Journal of Physics: Conference Series **653** (2015), 10.1088/1742-6596/653/1/012086.

[49] K. Sokolowski-Tinten, X. Shen, Q. Zheng, T. Chase, R. Coffee, M. Jerman, R. K. Li, M. Ligges, I. Makasyuk, M. Mo, A. H. Reid, B. Rethfeld, T. Vecchione, S. P. Weathersby, H. A. Dürr, and X. J. Wang, *Electron-lattice energy relaxation in laser-excited thin-film Au-insulator heterostructures studied by ultrafast MeV electron diffraction,* Structural Dynamics **4**, 054501 (2017).

[50] M. Z. Mo, Z. Chen, R. K. Li, M. Dunning, B. B. L. Witte, J. K. Baldwin, L. B. Fletcher, J. B. Kim, A. Ng, R. Redmer, A. H. Reid, P. Shekhar, X. Z. Shen, M. Shen, K. Sokolowski-Tinten, Y. Y. Tsui, Y. Q. Wang, Q. Zheng, X. J. Wang, and S. H. Glenzer, *Heterogeneous to homogeneous melting transition visualized with ultrafast electron diffraction,* Science **360**, 1451 (2018).

[51] S. D. Brorson, A. Kazeroonian, J. S. Moodera, D. W. Face, T. K. Cheng, E. P. Ippen, M. S. Dresselhaus, and G. Dresselhaus, *Femtosecond room-temperature measurement of the electron-phonon coupling constant in metallic superconductors,* Physical Review Letters **64**, 2172 (1990).

[52] L. Guo and X. Xu, *Ultrafast spectroscopy of electron-phonon coupling in gold,* Journal of Heat Transfer **136** (2014), 10.1115/1.4028543.

[53] T. G. White, P. Mabey, D. O. Gericke, N. J. Hartley, H. W. Doyle, D. McGonegle, D. S. Rackstraw, A. Higginbotham, and G. Gregori, *Electron-phonon equilibration in laser-heated gold films,* Physical Review B **90**, 14305 (2014).

[54] A. Nakamura, T. Shimojima, M. Nakano, Y. Iwasa, and K. Ishizaka, *Electron and lattice dynamics of transition metal thin films observed by ultrafast electron diffraction and transient optical measurements,* Structural Dynamics **3** (2016), 10.1063/1.4971210.

[55] Q. Zheng, X. Shen, K. Sokolowski-Tinten, R. K. Li, Z. Chen, M. Z. Mo, Z. L. Wang, S. P. Weathersby, J. Yang, M. W. Chen, and X. J. Wang, *Dynamics of Electron-Phonon Coupling in Bicontinuous Nanoporous Gold,* Journal of Physical Chemistry C **122**, 16368 (2018).

[56] M. I. Arefev, M. V. Shugaev, and L. V. Zhigilei, *Kinetics of laser-induced melting of thin gold film: How slow can it get?* Science Advances **8**, 1 (2022).

5

Ab initio-simulated optical response of hot electrons in gold and ruthenium

Optical femtosecond pump-probe experiments allow to measure the dynamics of ultrafast heating of metals with high accuracy. However, the theoretical analysis of such experiments is often complicated because of the indirect connection of the measured signal and the desired temperature transients. Establishing such a connection requires an accurate model of the optical constants of a metal, depending on both the electron temperature T_e and the lattice temperature T_l. In this chapter, we present first-principles simulations of the two-temperature scenario with $T_e \gg T_l$, illustrating the optical response of hot electrons to laser irradiation in gold and ruthenium. Comparing our simulations with the Kubo-Greenwood approach, we discuss the influence of electron-phonon and electron-electron scattering on the intraband contribution to optical constants. Applying the simulated optical constants to the analysis of ultrafast heating of ruthenium thin films we highlight the importance of the latter scattering channel to understand the measured heating dynamics.

5.1 Introduction

Femtosecond optical pump-probe measurements have become a standard technique for accessing the ultrafast dynamics of quasiparticle excitation and relaxation in the solid state [1–3], correlated systems [4, 5], and warm dense matter [6–10]. The way in which a measured transient optical response reflects the relaxation dynamics of excited matter is often indirect. The state-of-the-art approach for acquiring this knowledge is by performing direct quantum mechanical simulations of a pump-probe experiment using time-dependent density functional theory (TD-DFT) [11, 12]. However, due to the significant complexity of this method, researchers often employ the two-temperature model (TTM) [13, 14] or its extensions [15–18] for studying temperature dynamics, and model the optical response as a function of transient temperatures.

At low excitation energies, a linear relation between the measured signal and electron and lattice temperatures is often assumed [2]. However, in a general case of arbitrarily strong excitation, such an assumption does not necessarily hold, and a detailed understanding of how optical properties evolve with temperature is required. Analytical models allow for the treatment of simple [19, 20] and noble metals [21, 22], but most materials require DFT simulations at finite temperatures. The temperature-dependent optical response of systems with a bandgap is modeled via the Bethe-Salpeter equation approach, allowing for electron-hole interaction [23]. Density functional molecular dynamics (DFT-MD) combined with the Kubo-Greenwood theory has proven to be highly successful in describing systems where single-particle excitations dominate, such as metals [19, 20, 24] and dense plasmas [25–27].

In this work, we investigate the electron-temperature-dependent optical dielectric function of gold and ruthenium through DFT-MD simulations and the independent-particle approximation for the dielectric function. While gold has been extensively studied in this regard [7, 24, 28, 29], to the best of our knowledge, we are the first to conduct first-principles simulations for the dielectric function in ruthenium. In the example of gold we demonstrate that, although the employed approach is equivalent to the Kubo-Greenwood theory, it offers a significant advantage: an accurate description of the real part of the dielectric function without the necessity to simulate large systems of atoms, thanks to the explicit consideration of the Drude contribution to the dielectric function. It also offers an explicit treatment of electron-electron scattering, which becomes important at high temperatures. The trade-off, however, is the requirement for *a priori* knowledge of the damping parameter entering the Drude part. The resulting dielectric function of ruthenium, in combination with the aforementioned TTM, enables us to explore the transient optical response in ruthenium and compare it to recent measurements of ultrafast-laser-heated ruthenium thin films [30].

5.2 Model

5.2.1 Simulation technique

We performed first-principles simulations of the optical properties of gold and ruthenium using the Quantum Espresso package [31]. We employed the Perdew-Burke-Ernzerhof (PBE) exchange-correlation functional [32] and scalar-relativistic norm-conserving pseudopotentials from the PSEUDODOJO database [33] explicitly treating 19 electrons in Au and 16 in Ru. The simulation workflow was following. First, we performed a geometry optimization procedure to get relaxed cell parameters. Next, we set up a molecular dynamics (MD) simulation of an orthogonal $2 \times 2 \times 2$ supercell containing 32 atoms at an ion temperature of 300 K on a coarse $2 \times 2 \times 2$ k-point grid. We extracted several independent ionic configurations from the MD trajectory and performed accurate simulations of their optical properties using the SIMPLE code [34], which is based on the Shirley interpolation scheme and specifically designed for simulating optical properties.

The simulation of optical properties was performed in four stages: (i) self-consistent simulation of the electron density on a $16 \times 16 \times 16$ k-point grid for Au, and a $24 \times 16 \times 16$ k-point grid for orthogonalized Ru supercells, (ii) non-self-consistent simulation of the electron wavefunctions at the Γ-point and its seven periodic images at the corners of the unit cube (see more details in [35]), (iii) construction of the optimal basis set and calculation of velocity matrix elements on the k-point grid used in step (i), (iv) interpolation of matrix elements onto a fine k-point grid twice larger in every dimension than the grid used in steps (i), (iii), and calculation of the optical dielectric function. We used 80 Ry plane wave cutoff in steps (i) and (ii), 720 bands for Au and 500 bands for Ru in step (ii). To take into account the finite electron temperature, Fermi-Dirac smearing was applied.

Additionally, we performed density functional perturbation theory (DFPT) simulations of the electron-phonon (Fan-Migdal) self-energy within the ABINIT package [36, 37] using the same parameters as in our previous work [38], and used it as an intraband damping parameter in step (iv).

5.2.2 Dielectric function

The target quantity of our first-principles simulations is the electron-temperature-dependent complex dielectric function $\varepsilon(\omega)$, which defines optical properties such as complex refraction index $n + ik$, absorption coefficient α, and reflectivity R of a given material [39]:

$$\begin{aligned} n(\omega) + ik(\omega) &= \sqrt{\varepsilon(\omega)} \\ \alpha(\omega) &= \frac{2k\omega}{c} \\ R(\omega) &= \left| \frac{n(\omega) + ik(\omega) - 1}{n(\omega) + ik(\omega) + 1} \right|^2 \end{aligned} \tag{5.1}$$

here ω is an energy of incident photons, and c is the speed of light in vacuum. Hereinafter, we use atomic system of units $\hbar = e = m_e = 1$.

For a metal, the dielectric function can be conveniently written in terms of

interband and intraband (Drude) contributions [39]:

$$\varepsilon(\omega) = \varepsilon_{\text{inter}}(\omega) + \varepsilon_{\text{intra}}(\omega) \tag{5.2}$$

Within the Kohn-Sham quasiparticle picture and the independent-particle approximation, they are represented as follows [34]:

$$\varepsilon_{\text{inter}}(\omega) = 1 - \frac{4\pi}{\Omega} \sum_{\mathbf{k}, n \neq n'} \frac{|\langle n'\mathbf{k}| \mathbf{v} |n\mathbf{k}\rangle|^2}{\omega - \epsilon_{n'\mathbf{k}} + \epsilon_{n\mathbf{k}} + i0} \frac{f_{n\mathbf{k}} - f_{n'\mathbf{k}}}{(\epsilon_{n'\mathbf{k}} - \epsilon_{n\mathbf{k}})^2} \tag{5.3}$$

$$\varepsilon_{\text{intra}}(\omega) = -\frac{\omega_p^2}{\omega(\omega + i\gamma)} \tag{5.4}$$

where $|n\mathbf{k}\rangle$ is the Bloch state described by band number n and momentum $\mathbf{k}$ and having energy $\epsilon_{n\mathbf{k}}$, $f_{n\mathbf{k}}$ is the Fermi occupation number for the given state, Ω is the volume of a system, $\mathbf{v} = -i[\mathbf{r}, H_{KS}]$ is the velocity operator, and γ is a small broadening parameter that allows us to account for a finite quasiparticle lifetime. The plasma frequency of conduction electrons is given by [34]:

$$\omega_p^2 = \frac{4\pi}{\Omega} \sum_{\mathbf{k}, n} |\langle n\mathbf{k}| \mathbf{v} |n\mathbf{k}\rangle|^2 (-\partial_\epsilon f_{n\mathbf{k}}) \tag{5.5}$$

The dielectric function $\varepsilon(\omega)$ given by Eqs.(5.2)-(5.4) includes the dependence on electron temperature T_e in several ways: energies $\epsilon_{n\mathbf{k}}$ experience a slight shift with increasing T_e, Fermi occupations and their derivative are functions of T_e, and γ may vary with T_e. We consider electron-phonon (eph) and electron-electron (ee) scattering channels as the main contribution to the finite broadening of conduction electrons, $\gamma = \gamma^{\text{eph}} + \gamma^{\text{ee}}$.

The broadening arising from electron-phonon scattering can be extracted from the imaginary part of the Fan-Migdal self-energy Σ^{FM} [40]:

$$\gamma_{n\mathbf{k}}^{\text{eph}} = 2\,\text{Im}\{\Sigma_{n\mathbf{k}}^{\text{FM}}(\epsilon_{n\mathbf{k}})\} = 2\pi \sum_{\mathbf{q}, n', \nu} |g_{nn'}^{\nu}(\mathbf{k}, \mathbf{q})|^2 [(n_{\mathbf{q}\nu} + f_{n'\mathbf{k}+\mathbf{q}})\delta(\epsilon_{n\mathbf{k}} - \epsilon_{n'\mathbf{k}+\mathbf{q}} + \omega_{\mathbf{q}\nu}) + (n_{\mathbf{q}\nu} + 1 - f_{n'\mathbf{k}+\mathbf{q}})\delta(\epsilon_{n\mathbf{k}} - \epsilon_{n'\mathbf{k}+\mathbf{q}} - \omega_{\mathbf{q}\nu})] \tag{5.6}$$

here, $g_{nn'}^{\nu}(\mathbf{k}, \mathbf{q})$ is the electron-phonon matrix element, $\omega_{\mathbf{q}\nu}$ and $n_{\mathbf{q}\nu}$ are frequency and Bose occupation number of phonon mode ν with momentum $\mathbf{q}$. Isotropic γ^{eph} is obtained by averaging of $\gamma_{n\mathbf{k}}^{\text{eph}}$ over Fermi surface.

Eq. (5.6) is written assuming thermal equilibrium between electrons and lattice. Formally, in the two-temperature case of interest $T_e \gg T_l$, one must extend the Fan-Migdal self-energy to nonequilibrium regime [41] and evaluate it for several electron temperatures, which is a computationally expensive task. In practice, the self-energy is often weakly dependent on T_e [28, 42], and thus can be computed once for normal conditions.

However, for electron-electron scattering, one must account for its dependence on the electron temperature. This can be done, similar to the electron-phonon contribution, by calculating the imaginary part of the GW self-energy over a wide range

of electron temperatures, which again requires significant computational resources. Instead, we use temperature-dependent γ^{ee} values obtained from the kinetic theory for Au [43], and Ru [44].

5.3 Optical and electronic properties at normal conditions

In this section, we present the simulated dielectric function at normal conditions $T_e = T_l = 300\,\mathrm{K}$ and compare it to available experimental data. We also discuss the electron transport properties such as electron relaxation time, DC conductivity, and resistivity, since they can be easily obtained from our simulations. Additionally, using the example of gold, we discuss the advantages of the method we used compared to the Kubo-Greenwood (KG) formalism (see, e.g., [24, 45, 46]) – another popular method for the first-principles simulation of optical properties derived from the real part of dynamical conductivity. While it considers the electron-ion scattering contribution without the manual inclusion of a damping parameter γ, there is a continuous discussion in the community whether the electron-electron scattering is taken into account or not [26, 47–49]. The recent conclusion is that, although Kubo-Greenwood includes effects of electron-electron correlations through an exchange-correlational functional, it does not directly account for electron-electron scattering [27].

Fig. 5.1 shows the real and imaginary parts of the optical dielectric function in gold. In the region of photon energies up to 1.5 eV, where the intraband part makes a significant contribution, our simulations are in very good agreement with experimental data. At higher energies, when *d-s* interband transitions contribute, we see a larger deviation between simulations and experiment. We associate this with an underestimation of the gap between the *d*-band and the Fermi level at the PBE level, resulting in the appearance of an interband hill in the $\mathrm{Im}\,\varepsilon$ at lower energies than in the experiment (see Fig. 5.1(b)). The more narrow and intense shape of this hill is also arguably due to inaccuracies of the *d*-band form imposed by the use of pure PBE. The usage of hybrid functionals or GW corrections for obtaining accurate band structure is beyond the scope of this work, particularly since at high electron temperatures errors associated with a choice of exchange-correlational functional become smaller.

Surprisingly, the refractive index n and the extinction coefficient k, appear to be in better agreement with the experimental values (see Fig. 5.1(c)-(d)). Indeed, the interband transition threshold in n remains unchanged, but the absolute values of n and k are in much better agreement with the experiment. We believe this is due to the mutual error cancellation in the real and imaginary parts of the dielectric function.

The real and imaginary parts of the dielectric function in ruthenium are shown in Fig. 5.2(a)-(b). Our simulations demonstrate qualitatively the same behavior of $\mathrm{Im}\,\varepsilon(\omega)$ in Ru as in Au: there is a region of dominating intraband contribution below 0.5 eV followed by a strong interband transition peak around 2 eV. However, the valley in $\mathrm{Im}\,\varepsilon(\omega)$ separating these two regions is less pronounced in Ru due

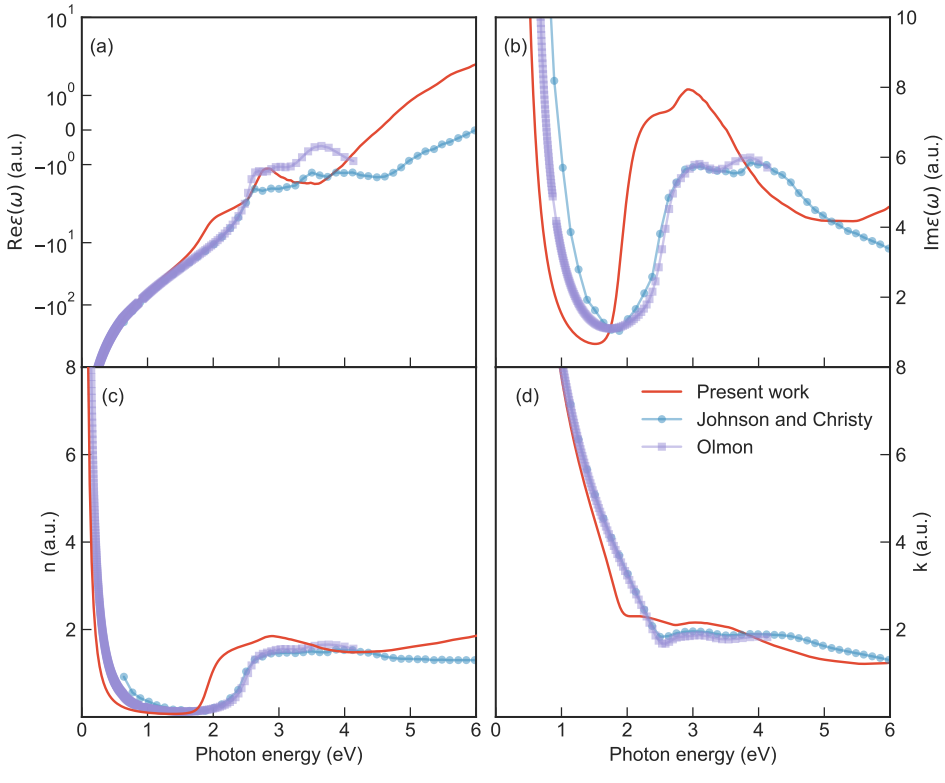

Figure 5.1: Real (a) and imaginary (b) parts of the dielectric function, real (c) and imaginary (d) parts of complex refractive index in gold. Red line corresponds to the results of the present simulations, blue line with circles is the experimental data of Johnson and Christy [50], purple line with squares is the measurements of Olmon *et al.* for a single-crystal gold sample [51].

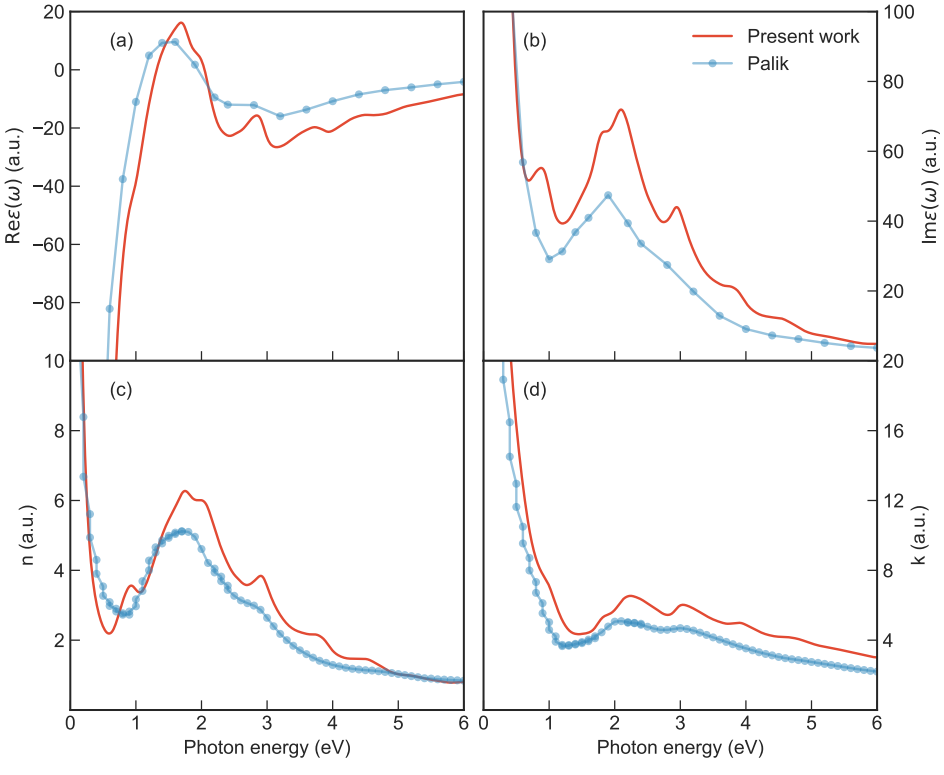

Figure 5.2: Real (a) and imaginary (b) parts of the dielectric function, real (c) and imaginary (d) part of complex refractive index in ruthenium. Red line corresponds to the results of the present simulations, blue line with circles is the data taken from Palik's handbook [52].

Material	γ^{eph} (meV)	τ (fs)	σ_0 (eV)	ρ ($\mu\Omega$ cm)	ρ_{exp} ($\mu\Omega$ cm)
Au	23.6	27.9 (27.3)	215.6	2.74 (2.16)	2.27 (at 300 K)
Ru	70.3	9.36 (8.2)	75.2	7.86 (5.13)	7.1 (at 273 K)

Table 5.1: Electron-phonon γ^{eph} broadening, carrier relaxation time τ, DC conductivity σ_0 and resistivity ρ at normal conditions $T_e = T_l = 300$ K for Au and Ru. τ values in brackets are obtained from first-principles simulations [53] (for Ru, $\tau = (2\tau_\perp + \tau_\parallel)/3$), ρ values in brackets are from the free-electron gas plasma frequency. Experimental resistivity ρ_{exp} is taken from [54].

to the presence of *d*-*s* interband transitions in this region. Simulations suggest several minor interband peaks below 1 eV and above 3 eV, which do not appear in the experiment. Unfortunately, we cannot unambiguously answer if these minor peaks are the simulation artifact or not, because the available experimental optical spectrum of Ru is quite outdated and there is no other data to compare with to the best of our knowledge. Similarly to the gold case, in Fig. 5.2(c) we see that the shape of refractive index n is determined by the shape of $\mathrm{Im}\,\varepsilon(\omega)$ and hence also has minor interband peaks not resolved by the experiment. The amplitudes of n and k agree well with the experimental ones.

Having obtained ω_p as an output of the SIMPLE simulations, we could easily calculate the DC conductivity $\sigma_0 = \tau\omega_p^2/4\pi$ and resistivity $\rho = 1/\sigma_0$, where the electron relaxation time within SERTA – self-energy relaxation time approximation – is simply $\tau = 1/\gamma^{\mathrm{eph}}$. We consider that at normal conditions, the electron-electron contribution to the relaxation time is negligible. The results are shown in Table 5.1. The room-temperature resistivity is slightly overestimated compared to the experiment. Assuming that relaxation times are correct, we deduce that ω_p values provided by our simulations might be underestimated.

On the other hand, the plasma frequency of a metal can be simply estimated according to the free-electron gas treatment of metals,

$$\omega_p = \sqrt{\frac{4\pi n_e}{m*}} \tag{5.7}$$

where n_e is an electron density taken as a number of conduction band electron per atom, $m*$ is an effective mass in units of m_e. Assuming that only *s*-electrons contribute to charge transfer and taking $m* = m_e$, we have $\omega_p^{\mathrm{Au}} = 9.02$ eV and $\omega_p^{\mathrm{Ru}} = 10.09$ eV. Using these values, we found that the resistivity in Au is about 3% lower than the experimental value, whereas the difference is about 27% in Ru. The larger error in Ru is rather expected, since the contribution of *d*-band electrons to resistivity cannot be completely neglected. Overall, we found the agreement between first-principles transport properties and experimental data to be reasonably accurate, validating our approach.

We benchmarked our simulations to KG-based simulations performed by Silaeva *et al.* [55]. The target quantity of the simulations in the KG formalism is the real part of dynamical conductivity $\sigma(\omega)$, which is directly proportional to the imaginary

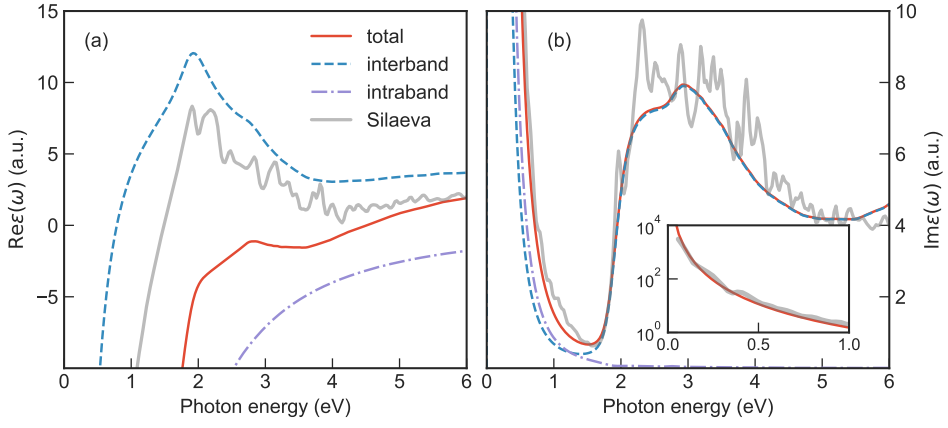

Figure 5.3: Total dielectric function, its interband and intraband contributions, and Kubo-Greenwood-based dielectric function taken from Silaeva *et al.* [55]. (a) is the real part, and (b) is the imaginary part of dielectric function. Inset in (b) shows the low-energy shoulder of $\mathrm{Im}\,\varepsilon(\omega)$.

part of the dielectric function [56]:

$$\mathrm{Im}\,\varepsilon(\omega) = \frac{4\pi}{\omega}\,\mathrm{Re}\,\sigma(\omega) \tag{5.8}$$

The real part of the dielectric function is then restored from Kramers-Kronig (KK) relations [56]:

$$\mathrm{Re}\,\varepsilon(\omega) = 1 + \frac{4\pi}{\omega}\frac{2}{\pi}\fint_0^\infty \frac{\mathrm{Re}\,\sigma(\omega')\omega}{\omega'^2 - \omega^2}d\omega' \tag{5.9}$$

Fig. 5.3 shows the comparison between our simulations and KG ones. The very good agreement of the imaginary parts of the dielectric function, shown in Fig. 5.3(b), confirms that both approaches yield identical $\mathrm{Im}\,\varepsilon(\omega)$ / $\mathrm{Re}\,\sigma(\omega)$ if one uses similar simulation parameters. However, that is not the case for the real part of the dielectric function shown in Fig. 5.3(a): the results reported by Silaeva differ quite significantly from ours. The KG-based $\mathrm{Re}\,\varepsilon(\omega)$ has a shape closer to the interband contribution, not the total one. At first glance, we found this to be controversial: why, with $\mathrm{Im}\,\varepsilon(\omega)$ being essentially the same, does the KG $\mathrm{Re}\,\varepsilon$ capture mostly interband transitions?

The following reasoning can answer this question. While the KG approach formally includes both intra- and interband contributions to dynamic conductivity, the intraband part converges very slowly with an increase in supercell size and may require simulating up to several thousand atoms [57]. However, the usage of KK relations in Eq. (5.9) requires highly accurate values of the dynamical conductivity in the DC limit ($\omega \to 0$) [24], where the intraband contribution dominates. Consequently, although the Kubo-Greenwood formalism provides reasonable optical conductivity data without any *a priori* knowledge of the broadening parameter γ, in most cases, it necessitates a significant computational effort to obtain an accurate real part of the dielectric function for materials with a non-vanishing intraband

contribution. It follows from all of the above that Silaeva *et al.* could not reach converged values of DC conductivity, and hence were not able to produce an accurate real part of the optical dielectric function. In contrast, the explicit inclusion of the Drude term in the dielectric function allowed us to achieve reasonably accurate $\varepsilon(\omega)$. However, the price we paid is the need for additional simulations of the γ value.

5.4 Optical properties at high T_e

5.4.1 Influence of electron-electron scattering

Before presenting the optical properties of gold and ruthenium at high electron temperatures, we will discuss the influence of the temperature-dependent damping parameter $\gamma^{\mathrm{ee}}(T_e)$ on the dielectric function. To do so, we compare $\operatorname{Im}\varepsilon(\omega)$ of gold at several electron temperatures obtained from our simulations with those extracted from the KG conductivity [55]. As we discussed above, the statement of whether the KG approach accounts for electron-electron scattering or not is highly debatable. Contributing to the discussion, we will consider both scenarios below. The results of the comparison are depicted in Fig. 5.4.

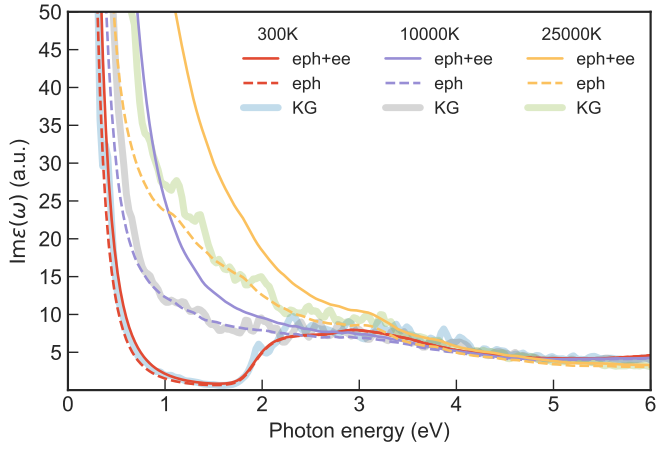

Figure 5.4: Imaginary part of the dielectric function in gold, calculated for $T_e = 300\,\mathrm{K}, 10000\,\mathrm{K}, 25000\,\mathrm{K}$. Solid lines correspond to T_e-dependent $\gamma = \gamma^{\mathrm{eph}} + \gamma^{\mathrm{ee}}$, dashed lines to constant $\gamma = \gamma^{\mathrm{eph}}$, and thick semi-transparent lines are the KG simulations of Silaeva *et al.* [55].

When electron-electron scattering is disabled, the intraband shoulder aligns well with KG results, especially at not-too-high electron temperatures. At $T_e = 25\,\mathrm{kK}$, the intraband shoulder obtained using constant damping becomes noticeably narrower than the KG one. The overall good agreement between our simulations and KG approach validates our approximation of constant γ^{eph} in a wide range of T_e considering that the KG approach does not include electron-electron scattering as well.

It is interesting to see how the inclusion of the T_e-dependent electron-electron

scattering affects the shape of $\mathrm{Im}\,\varepsilon(\omega)$. As expected, under normal conditions with $T_e = 300\,\mathrm{K}$, electron-electron scattering contributes only insignificantly. However, as the temperature increases, its influence becomes considerable. The low-energy intraband shoulder is roughly twice as wide for $T_e = 10$ and $25\,\mathrm{kK}$ compared to the predictions of KG.

If we come back to the previous arguments stating that the KG *includes* the electron-electron scattering, then we must admit that the $\gamma^{\mathrm{ee}}(T_e)$ obtained from kinetic theory significantly overestimates the intraband contribution. There is an argument that the Lindhard screening used by Petrov *et al.*[43] might lead to an order of magnitude overestimation of electron-electron damping [58]. Additionally, there could be a double-counting error: coming back to Fig. 5.3(b), it is apparent that the low-energy shoulder is formed equally by both intra- and interband parts. We speculate that, similarly to KG approach, an interband contribution could solely capture the effect of electron-electron scattering, making its inclusion in the intraband part unnecessary.

For the sake of scientific objectivity, below we present optical properties obtained both *with* and *without* $\gamma^{\mathrm{ee}}(T_e)$ and discuss the implications of this particular choice in comparison to the experimental results for femtosecond-laser-heated Ru in Section 5.5.

5.4.2 Optical properties of Au and Ru

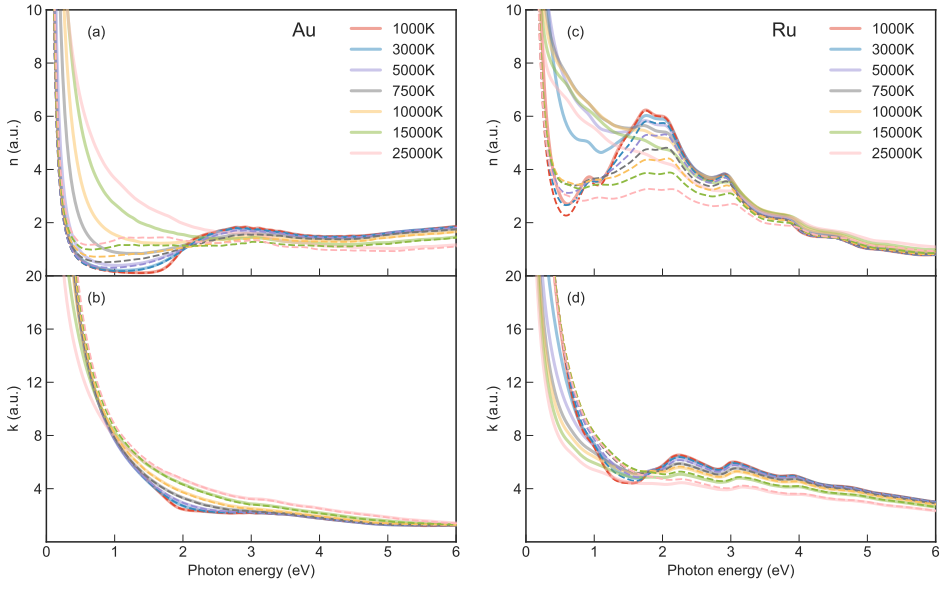

Figure 5.5: Refractive index n and extinction coefficient k in gold (a),(b), and ruthenium (c),(d) for different values of T_e. Lattice temperature is fixed at normal conditions $T_l = 300\,\mathrm{K}$. Solid semi-transparent lines correspond to temperature-dependent damping $\gamma = \gamma^{\mathrm{eph}} + \gamma^{\mathrm{ee}}$, dashed lines – to constant damping $\gamma = \gamma^{\mathrm{eph}}$.

Fig. 5.5 (a) and (b) presents the electron-temperature-dependent n and k values in gold. The refractive index n is notably influenced by the specific choice of broadening. With constant $\gamma = \gamma^{\text{eph}}$ broadening, the infrared intraband shoulder ($\omega \leq 0.5\,\text{eV}$) remains unchanged with an increase in T_e. Changes primarily manifest in the 0.5 – 3 eV region due to the smearing of the Fermi distribution. This smearing opens previously forbidden interband transitions at lower energies ($\omega \lesssim 2\,\text{eV}$) but reduces the probability of interband transitions at energies above 2 eV. In contrast, for the T_e-dependent $\gamma = \gamma^{\text{eph}} + \gamma^{\text{ee}}$ broadening, the intraband shoulder intensifies with an increase in T_e, causing a notable relative decrease in the d-band contribution in the 0.5-3 eV region. The extinction coefficient k (Fig. 5.5(b)) exhibits weak dependence on γ. The T_e-dependent broadening results in a slightly narrower shape of the intraband shoulder compared to the constant one only in the infrared region below 1 eV.

The qualitative picture remains the same for ruthenium, but the dominance of the intraband contribution in the T_e-dependent case in the region $\omega \lesssim 2\,\text{eV}$ is more pronounced for both n and k, as depicted in Fig. 5.5(c) and (d). This is a direct consequence of the overlap between s- and d-band states, resulting in non-vanishing electron-electron scattering of s-electrons even at low temperatures and high γ^{ee}. Such a strong intraband contribution blurs the valley of weak d-s interband transitions within the 0.5-1.5 eV range.

5.5 Comparison with experiment for femtosecond-irradiated Ru

5.5.1 Fermi smearing mechanism in Ru

In our recent work [30], we investigated the mechanism of heating and degradation of ruthenium thin films irradiated by a $\omega = 1.55\,\text{eV}$ femtosecond laser pulse. We discovered that the optical response of heated Ru can be qualitatively described by the Fermi smearing mechanism [59, 60], where the peak thermoreflectance signal is proportional to the change of electron occupations with increasing T_e:

$$R(\omega, T_e) - R(\omega, T_0) \sim \frac{1}{\exp\left(\frac{\omega+\Delta\epsilon}{k_B T_e}\right) + 1} - \frac{1}{\exp\left(\frac{\omega+\Delta\epsilon}{k_B T_0}\right) + 1} \tag{5.10}$$

Here, $T_0 = 300\,\text{K}$, and $\Delta\epsilon$ is the difference between the energy level experiencing the optical transition and the Fermi level of Ru. We treated $\Delta\varepsilon$ as the fitting parameter, independent of electron temperature, and thus having the meaning of an averaged energy level from which electrons are excited. By fitting experimental peak thermoreflectance values, we obtained $\Delta\epsilon = -1.2\,\text{eV}$.

Now, with the simulated T_e-dependent optical constants in ruthenium, we can assess the validity of the Fermi smearing mechanism. We calculated the relative reflectivity change using Eq. (5.1) and compared it to the change in the Fermi distribution given by Eq. (5.10). The results of the comparison are presented in Fig. 5.6. The Fermi smearing theory, with $\Delta\epsilon = -1.2\,\text{eV}$, suggests a steeper growth of reflectivity change with an increase in T_e compared to our simulations, both

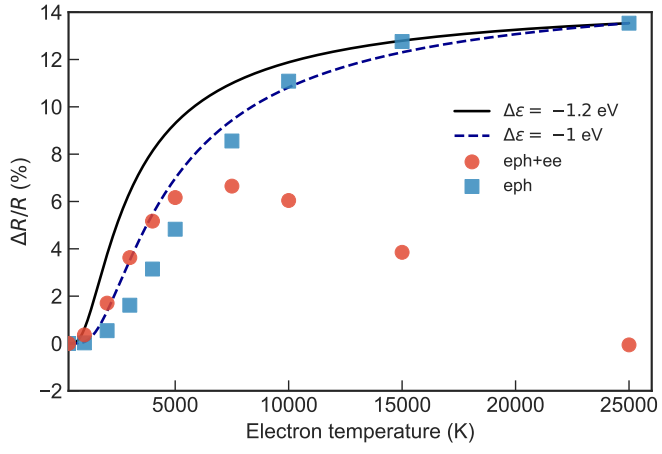

Figure 5.6: Change of optical reflectivity with an increasing T_e. Orange circles are the results of simulation with T_e-dependent 'eph+ee' damping, blue squares – with constant 'eph' damping. Solid and dashed lines represent Fermi smearing given by Eq. (5.10) for two different $\Delta\epsilon$.

accounting for and neglecting electron-electron damping. If a smaller $\Delta\epsilon = -1$ eV is applied, our 'eph+ee' simulations agree well with the Fermi smearing curve up to $T_e = 5$ kK. Constant 'eph' damping, on the contrary, suggests slower growth at low temperatures but has the same high-temperature asymptotic and overall increasing-saturation behavior as the change in the Fermi distribution.

At higher temperatures, the reflectivity change obtained from simulations with enabled T_e-dependent electron-electron damping has a peak around $T_e = 7.5$ kK and then decays with further temperature increase. Although this increasing-saturating-decreasing behavior contradicts the simple Fermi smearing theory, it might accurately reflect the experimental observations. In our experiments, we observed a similar behavior in peak thermoreflectance values for a 125 nm thick film (cf. Fig 2.3). We initially attributed a drop in reflectivity to film damage, but in the light of current simulations, it may be associated purely with the response of hot electrons before damage occurred.

5.5.2 Time-resolved optical response

Another application of our optical constants is the estimation of transient thermoreflectance after ultrafast electron heating using the TTM. This model assumes that instantly thermalized electrons transfer energy to the cold lattice via the electron-phonon scattering mechanism and relax towards equilibrium. The evolution of electron and lattice temperatures is described by two coupled heat equations:

$$\begin{aligned} C_e(T_e)\frac{\partial T_e}{\partial t} &= \nabla(k_e \nabla T_e) - G(T_e - T_l) + S(t,x), \\ C_l \frac{\partial T_l}{\partial t} &= G(T_e - T_l). \end{aligned} \tag{5.11}$$

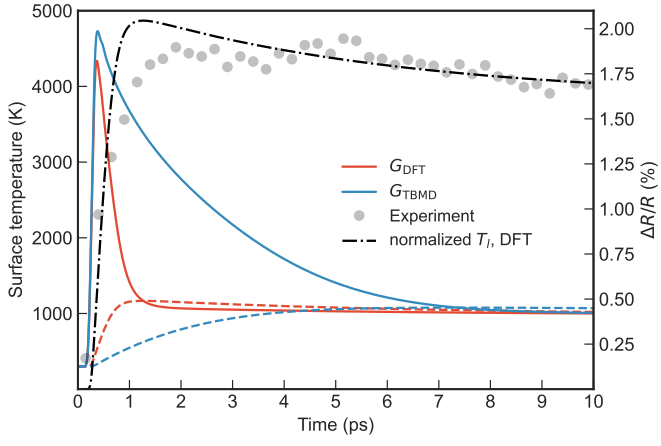

Figure 5.7: Evolution of electron (solid lines) and lattice (dashed lines) temperatures on surface of 30 nm Ru thin film for an incident laser fluence 24.5 mJ/cm^2 obtained from the TTM using two different models for electron-phonon coupling: DFT [38] and TBMD [61]. Black dash-dotted line represents the normalized lattice temperature for DFT-based electron-phonon coupling. Experimental transient thermoreflectance points are shown with gray dots.

The electron heat capacity $C_e(T_e) = \frac{\partial}{\partial T_e} \int g(\epsilon, T_e) f(\epsilon, T_e) \epsilon d\epsilon$ is calculated from the electron density of states $g(\epsilon, T_e)$ of Ru, as simulated in our recent work [38]. The lattice heat capacity C_l is constant in the temperature regime we are interested in, according to the Dulong-Petit law. We employed a model for the electron thermal conductivity $k_e = k_e(T_e, T_l)$ proposed by Petrov *et al.* [44]. Two models for the electron-phonon coupling parameter G were used: one obtained from first-principles simulations [38], and another taken from non-adiabatic tight-binding – molecular dynamics (TBMD) approach [61]. We considered a Gaussian laser pulse $S(t, x)$, taking into account the effect of multiple reflections at thin film interfaces.

Fig. 5.7 illustrates an example of two-temperature evolution in a 30 nm Ru thin film irradiated by an incident laser fluence $F = 24.5\,\mathrm{mJ/cm^2}$. Our model predicts a sharp peak in the electron temperature for both models of the electron-phonon coupling parameter. According to the theoretical dependence of R on T_e (Fig. 5.6), one might expect to observe a similar sharp peak in thermoreflectance values in the experiment. However, experimental values exhibit a noticeably different behavior: an initial sharp increase due to ultrafast energy deposition is followed by a rather flat or slowly decaying trend. We found that the experimental trend closely aligns with the evolution of lattice temperature when the DFT-based G is considered.

Such a good agreement between simulated lattice temperature and experimentally measured thermoreflectance trends, along with the absence of an electron temperature peak in the experiment, could be attributed to several scenarios or a combination of them. First, the experimental setup may not have allowed for the resolution of the electron temperature peak due to a timestep of 250 fs, while the pump pulse duration was about 85 fs. Second, the electron-phonon coupling might be even stronger than *ab initio* predictions, and with the pump-probe mea-

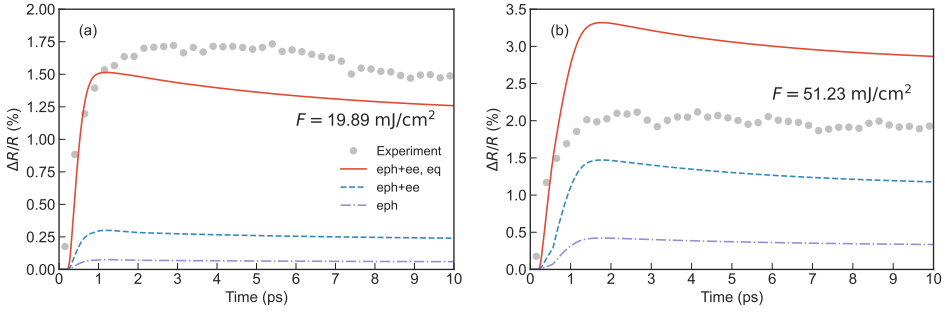

Figure 5.8: Time-resolved thermoreflectance values in 30 nm Ru thin film for incident fluence of 19.89 mJ/cm^2 (a) and 51.23 mJ/cm^2 (b). Red solid line corresponds to R obtained with an account for equilibrium temperature dependence for both 'eph' and 'ee' damping, blue dashed line to constant 'eph' and temperature-dependent 'ee' damping, lilac dash-dotted line to constant 'eph' damping. Experimental data are shown in gray dots.

surements, we may have accessed an already equilibrated electron-lattice system. Finally, in the range of excitation energies and temperatures reached, the optical properties could depend mostly on the lattice temperature. Below, we will evaluate the second and third scenarios and see if transient thermoreflectance can be successfully modeled by our first-principles optical properties depending on the *equilibrium lattice temperature*.

In the equilibrium case $T_e = T_l \equiv T$, we cannot ignore the influence of the lattice temperature on optical properties. To account for this, we performed several trial DFT-MD simulations at lattice temperatures up to 1500 K and did not find any significant changes in optical constants compared to $T_l = 300$ K. However, at equilibrium and not-too-high temperatures, the electron-phonon damping γ^{eph} should vary linearly with T. We performed simulations of the Fan-Migdal self-energy for $T = 100 - 300$ K and extracted a linear slope for this dependence, $a = 2.1517 \times 10^{-4}$ eV/K.

Fig. 5.8 illustrates the temporal evolution of R in two limits of low and high incident laser fluences. In Fig. 5.8(a), at a low level of excitation corresponding to peak $T \simeq 1000$ K in our TTM simulations, our temperature-dependent optical constants successfully overlapped with the experimental points when considering the temperature dependence of all damping channels. The agreement between the experimental data and the simulations becomes unsatisfactory if we neglect the T-dependence of γ^{eph}. Contrarily, in the case of high laser fluence (Fig. 5.8(b)), the scenario changes: optical constants simulated with a constant γ^{eph} and temperature-dependent γ^{ee} provide a better match with the experimental points. This discrepancy is attributed to the fact that at high excitation levels (and, consequently, high lattice temperatures, peak $T \simeq 2000$ K), a linear temperature dependence of γ^{eph} does not hold. Assuming a linear relation between γ^{eph} and T at high T values results in an overestimation of changes in optical properties. At elevated temperatures, γ^{ee} becomes dominant, and disregarding the temperature dependence of γ^{eph} only introduces a minor discrepancy.

From the analysis provided, it becomes clear that the accurate first-principles

description of ultrafast pump-probe experiments in transition metals with very large electron-phonon coupling strength $G \geq 10^{18}\,\mathrm{W/m^3K}$ is a challenging task. It seems that the two-temperature state occurs only at very short timescales, often inaccessible in pump-probe experiments, or nonequilibrium electrons start to exchange energy with the lattice, completely missing the two-temperature regime. Accounting for the T_e-dependent electron-electron damping parameter γ^{ee} is crucial for an accurate description of optical properties at high levels of excitation, whereas at low levels of excitation, knowledge of the temperature-dependent γ^{eph} is needed. Overall, a complete understanding of the dynamics of optical properties requires their dependence on *both* electron and lattice temperatures. Such type of simulations are possible yet extremely demanding, as one needs to span the (T_e, T_l) space using any of first-principles approaches accounting for both electron-electron and electron-phonon scattering.

5.6 Conclusions

We presented the simulated optical properties of gold and ruthenium in the two-temperature regime $T_e \gg T_l$, which is achievable in ultrafast laser irradiation experiments. Our calculations are carried out within the DFT framework and the independent-particle approximation for the optical dielectric function.

First, to validate our approach, we compared the simulated optical constants and derived resistivity values with experimental data available at normal conditions ($T_e = T_l = 300\,\mathrm{K}$). We discussed the similarities and differences between the method we used and the Kubo-Greenwood theory. While the imaginary parts of the optical dielectric function are essentially identical in both methods, our approach provides a more accurate real part without the necessity to simulate huge supercells due to an explicit account for intraband (Drude) contribution. Second, at elevated electron temperatures, We demonstrated that the Kubo-Greenwood approach appears to be incapable of describing electron-electron scattering. In our approach, the accuracy of simulated optical properties at high T_e in the low-energy region ($\lesssim 2\,\mathrm{eV}$) is determined by the accuracy of the chosen electron-electron damping parameter.

We compared simulated optical properties to experimental time-resolved thermoreflectance in Ru thin films [30]. We could reasonably match experimental data with our two-temperature optical constants at high levels of initial electron excitation, whereas at low levels, simulations with equilibrium $T_e = T_l$ were necessary. We attribute this to the very fast thermalization between electrons and lattice in Ru, requiring knowledge of optical properties at elevated lattice temperatures.

Acknowledgments

Author thanks Kirill Migdal for the provided values of electron-electron damping in Ru, and for the fruitful discussion about the choice of a particular screening model in the kinetic theory approach. Author also thanks SURF (www.surf.nl) for the support in using the National Supercomputer Snellius.

References

[1] A. J. Sabbah and D. M. Riffe, *Femtosecond pump-probe reflectivity study of silicon carrier dynamics,* Physical Review B **66**, 165217 (2002).

[2] P. M. Norris, A. P. Caffrey, R. J. Stevens, J. M. Klopf, J. T. McLeskey, and A. N. Smith, *Femtosecond pump–probe nondestructive examination of materials (invited),* Review of Scientific Instruments **74**, 400 (2003).

[3] M. Zürch, H.-T. Chang, L. J. Borja, P. M. Kraus, S. K. Cushing, A. Gandman, C. J. Kaplan, M. H. Oh, J. S. Prell, D. Prendergast, C. D. Pemmaraju, D. M. Neumark, and S. R. Leone, *Direct and simultaneous observation of ultrafast electron and hole dynamics in germanium,* Nature Communications **8**, 15734 (2017).

[4] A. Kirilyuk, A. V. Kimel, and T. Rasing, *Ultrafast optical manipulation of magnetic order,* Reviews of Modern Physics **82**, 2731 (2010).

[5] M. F. Jager, C. Ott, P. M. Kraus, C. J. Kaplan, W. Pouse, R. E. Marvel, R. F. Haglund, D. M. Neumark, and S. R. Leone, *Tracking the insulator-to-metal phase transition in VO_2 with few-femtosecond extreme UV transient absorption spectroscopy,* Proceedings of the National Academy of Sciences **114**, 9558 (2017).

[6] H. Yoneda, H. Morikami, K.-i. Ueda, and R. M. More, *Ultra-short pulse laser pump-probe experiments for investigation of warm dense plasmas,* Journal of Quantitative Spectroscopy and Radiative Transfer **99**, 690 (2006).

[7] Y. Ping, D. Hanson, I. Koslow, T. Ogitsu, D. Prendergast, E. Schwegler, G. Collins, and A. Ng, *Dielectric function of warm dense gold,* Physics of Plasmas **15** (2008), 10.1063/1.2844365.

[8] Y. Ping, A. Correa, T. Ogitsu, E. Draeger, E. Schwegler, T. Ao, K. Widmann, D. Price, E. Lee, H. Tam, P. Springer, D. Hanson, I. Koslow, D. Prendergast, G. Collins, and A. Ng, *Warm dense matter created by isochoric laser heating,* High Energy Density Physics **6**, 246 (2010).

[9] Z. Chen, B. Holst, S. E. Kirkwood, V. Sametoglu, M. Reid, Y. Y. Tsui, V. Recoules, and A. Ng, *Evolution of ac Conductivity in Nonequilibrium Warm Dense Gold,* Physical Review Letters **110**, 135001 (2013).

[10] Z. Chen, X. Na, C. B. Curry, S. Liang, M. French, A. Descamps, D. P. DePonte, J. D. Koralek, J. B. Kim, S. Lebovitz, M. Nakatsutsumi, B. K. Ofori-Okai, R. Redmer, C. Roedel, M. Schörner, S. Skruszewicz, P. Sperling, S. Toleikis, M. Z. Mo, and S. H. Glenzer, *Observation of a highly conductive warm dense state of water with ultrafast pump–probe free-electron-laser measurements,* Matter and Radiation at Extremes **6** (2021), 10.1063/5.0043726.

[11] M. Volkov, S. A. Sato, F. Schlaepfer, L. Kasmi, N. Hartmann, M. Lucchini, L. Gallmann, A. Rubio, and U. Keller, *Attosecond screening dynamics mediated by electron localization in transition metals,* Nature Physics **15**, 1145 (2019).

[12] J. Lloyd-Hughes, P. M. Oppeneer, T. Pereira dos Santos, A. Schleife, S. Meng, M. A. Sentef, M. Ruggenthaler, A. Rubio, I. Radu, M. Murnane, X. Shi, H. Kapteyn, B. Stadtmüller, K. M. Dani, F. H. da Jornada, E. Prinz, M. Aeschlimann, R. L. Milot, M. Burdanova, J. Boland, T. Cocker, and F. Hegmann, *The 2021 ultrafast spectroscopic probes of condensed matter roadmap,* Journal of Physics: Condensed Matter **33**, 353001 (2021).

[13] M. I. Kaganov, I. M. Lifshitz, and L. V. Tanatarov, *Relaxation between electrons and crystalline lattice,* Sov. Phys. JETP **4**, 173 (1957).

[14] S. Anisimov, B. Kapeliovich, and T. Perel'man, *Electron emission from metal surfaces exposed to ultrashort laser pulses,* Journal of Experimental and Theoretical Physics **66**, 375 (1974).

[15] H. M. van Driel, *Kinetics of high-density plasmas generated in Si by 1.06- and 0.53- μm picosecond laser pulses,* Physical Review B **35**, 8166 (1987).

[16] D. S. Ivanov and L. V. Zhigilei, *Combined atomistic-continuum modeling of short-pulse laser melting and disintegration of metal films,* Physical Review B **68**, 064114 (2003).

[17] L. Waldecker, R. Bertoni, R. Ernstorfer, and J. Vorberger, *Electron-Phonon Coupling and Energy Flow in a Simple Metal beyond the Two-Temperature Approximation,* Physical Review X **6**, 021003 (2016).

[18] L. Alber, V. Scalera, V. Unikandanunni, D. Schick, and S. Bonetti, *NTMpy: An open source package for solving coupled parabolic differential equations in the framework of the three-temperature model,* Computer Physics Communications **265**, 107990 (2021).

[19] M. E. Povarnitsyn, D. V. Knyazev, and P. R. Levashov, *Ab Initio Simulation of Complex Dielectric Function for Dense Aluminum Plasma,* Contributions to Plasma Physics **52**, 145 (2012).

[20] D. V. Knyazev and P. R. Levashov, *Transport and optical properties of warm dense aluminum in the two-temperature regime: Ab initio calculation and semiempirical approximation,* Physics of Plasmas **21** (2014), 10.1063/1.4891341.

[21] K. C. Rustagi, *Bilinear optical polarizability of silver,* Il Nuovo Cimento B Series 10 **53**, 346 (1968).

[22] J. Hohlfeld, D. Grosenick, U. Conrad, and E. Matthias, *Femtosecond time-resolved reflection second-harmonic generation on polycrystalline copper,* Applied Physics A Materials Science and Processing **60**, 137 (1995).

[23] K. Ramakrishna and J. Vorberger, *Ab initio dielectric response function of diamond and other relevant high pressure phases of carbon,* Journal of Physics: Condensed Matter **32**, 095401 (2020).

[24] B. Holst, V. Recoules, S. Mazevet, M. Torrent, A. Ng, Z. Chen, S. E. Kirkwood, V. Sametoglu, M. Reid, and Y. Y. Tsui, *Ab initio model of optical properties of two-temperature warm dense matter,* Physical Review B **90**, 035121 (2014).

[25] B. B. L. Witte, P. Sperling, M. French, V. Recoules, S. H. Glenzer, and R. Redmer, *Observations of non-linear plasmon damping in dense plasmas,* Physics of Plasmas **25**, 56901 (2018).

[26] H. Reinholz, G. Röpke, S. Rosmej, and R. Redmer, *Conductivity of warm dense matter including electron-electron collisions,* Physical Review E **91**, 043105 (2015).

[27] M. French, G. Röpke, M. Schörner, M. Bethkenhagen, M. P. Desjarlais, and R. Redmer, *Electronic transport coefficients from density functional theory across the plasma plane,* Physical Review E **105**, 065204 (2022).

[28] A. M. Brown, R. Sundararaman, P. Narang, W. A. Goddard, and H. A. Atwater, *Ab initio phonon coupling and optical response of hot electrons in plasmonic metals,* Physical Review B **94**, 075120 (2016).

[29] A. Blumenstein, E. S. Zijlstra, D. S. Ivanov, S. T. Weber, T. Zier, F. Kleinwort, B. Rethfeld, J. Ihlemann, P. Simon, and M. E. Garcia, *Transient optics of gold during laser irradiation: From first principles to experiment,* Physical Review B **101**, 165140 (2020).

[30] F. Akhmetov, I. Milov, S. Semin, F. Formisano, N. Medvedev, J. M. Sturm, V. V. Zhakhovsky, I. A. Makhotkin, A. Kimel, and M. Ackermann, *Laser-induced electron dynamics and surface modification in ruthenium thin films,* Vacuum **212**, 112045 (2023).

[31] P. Giannozzi, S. Baroni, N. Bonini, M. Calandra, R. Car, C. Cavazzoni, D. Ceresoli, G. L. Chiarotti, M. Cococcioni, I. Dabo, A. Dal Corso, S. de Gironcoli, S. Fabris, G. Fratesi, R. Gebauer, U. Gerstmann, C. Gougoussis, A. Kokalj, M. Lazzeri, L. Martin-Samos, N. Marzari, F. Mauri, R. Mazzarello, S. Paolini, A. Pasquarello, L. Paulatto, C. Sbraccia, S. Scandolo, G. Sclauzero, A. P. Seitsonen, A. Smogunov, P. Umari, and R. M. Wentzcovitch, *QUANTUM ESPRESSO: a modular and open-source software project for quantum simulations of materials,* Journal of Physics: Condensed Matter **21**, 395502 (2009).

[32] J. P. Perdew, K. Burke, and M. Ernzerhof, *Generalized Gradient Approximation Made Simple,* Physical Review Letters **77**, 3865 (1996).

[33] M. van Setten, M. Giantomassi, E. Bousquet, M. Verstraete, D. Hamann, X. Gonze, and G.-M. Rignanese, *The PseudoDojo: Training and grading a 85 element optimized norm-conserving pseudopotential table,* Computer Physics Communications **226**, 39 (2018).

[34] G. Prandini, M. Galante, N. Marzari, and P. Umari, *SIMPLE code: Optical properties with optimal basis functions,* Computer Physics Communications **240**, 106 (2019).

[35] D. Prendergast and S. G. Louie, *Bloch-state-based interpolation: An efficient generalization of the Shirley approach to interpolating electronic structure,* Physical Review B **80**, 235126 (2009).

[36] X. Gonze, B. Amadon, G. Antonius, F. Arnardi, L. Baguet, J.-M. Beuken, J. Bieder, F. Bottin, J. Bouchet, E. Bousquet, N. Brouwer, F. Bruneval, G. Brunin, T. Cavignac, J.-B. Charraud, W. Chen, M. Côté, S. Cottenier, J. Denier, G. Geneste, P. Ghosez, M. Giantomassi, Y. Gillet, O. Gingras, D. R. Hamann, G. Hautier, X. He, N. Helbig, N. Holzwarth, Y. Jia, F. Jollet, W. Lafargue-Dit-Hauret, K. Lejaeghere, M. A. Marques, A. Martin, C. Martins, H. P. Miranda, F. Naccarato, K. Persson, G. Petretto, V. Planes, Y. Pouillon, S. Prokhorenko, F. Ricci, G.-M. Rignanese, A. H. Romero, M. M. Schmitt, M. Torrent, M. J. van Setten, B. Van Troeye, M. J. Verstraete, G. Zérah, and J. W. Zwanziger, *The Abinitproject: Impact, environment and recent developments,* Computer Physics Communications **248**, 107042 (2020).

[37] A. H. Romero, D. C. Allan, B. Amadon, G. Antonius, T. Applencourt, L. Baguet, J. Bieder, F. Bottin, J. Bouchet, E. Bousquet, F. Bruneval, G. Brunin, D. Caliste, M. Côté, J. Denier, C. Dreyer, P. Ghosez, M. Giantomassi, Y. Gillet, O. Gingras, D. R. Hamann, G. Hautier, F. Jollet, G. Jomard, A. Martin, H. P. C. Miranda, F. Naccarato, G. Petretto, N. A. Pike, V. Planes, S. Prokhorenko, T. Rangel, F. Ricci, G.-M. Rignanese, M. Royo, M. Stengel, M. Torrent, M. J. van Setten, B. Van Troeye, M. J. Verstraete, J. Wiktor, J. W. Zwanziger, and X. Gonze, *ABINIT: Overview and focus on selected capabilities,* The Journal of Chemical Physics **152** (2020), 10.1063/1.5144261.

[38] F. Akhmetov, I. Milov, I. A. Makhotkin, M. Ackermann, and J. Vorberger, *Electron-phonon coupling in transition metals beyond Wang's approximation,* Physical Review B **108**, 214301 (2023).

[39] J. M. Ziman, *Principles of the Theory of Solids* (Cambridge university press, 1972).

[40] F. Giustino, *Electron-phonon interactions from first principles,* Reviews of Modern Physics **89**, 015003 (2017).

[41] G. Stefanucci, R. van Leeuwen, and E. Perfetto, *In and Out-of-Equilibrium Ab Initio Theory of Electrons and Phonons,* Physical Review X **13**, 031026 (2023).

[42] A. Ng, P. Sterne, S. Hansen, V. Recoules, Z. Chen, Y. Y. Tsui, and B. Wilson, *dc conductivity of two-temperature warm dense gold,* Physical Review E **94**, 033213 (2016).

[43] Y. V. Petrov, N. A. Inogamov, and K. P. Migdal, *Thermal conductivity and the electron-ion heat transfer coefficient in condensed media with a strongly excited electron subsystem,* JETP Letters **97**, 20 (2013).

[44] Y. Petrov, K. Migdal, N. Inogamov, V. Khokhlov, D. Ilnitsky, I. Milov, N. Medvedev, V. Lipp, and V. Zhakhovsky, *Ruthenium under ultrafast laser excitation: Model and dataset for equation of state, conductivity, and electron-ion coupling,* Data in Brief **28**, 104980 (2020).

[45] L. Calderín, V. Karasiev, and S. Trickey, *Kubo–Greenwood electrical conductivity formulation and implementation for projector augmented wave datasets,* Computer Physics Communications **221**, 118 (2017).

[46] G. S. Demyanov, D. V. Knyazev, and P. R. Levashov, *Continuous Kubo-Greenwood formula: Theory and numerical implementation,* Physical Review E **105**, 035307 (2022).

[47] M. P. Desjarlais, J. D. Kress, and L. A. Collins, *Electrical conductivity for warm, dense aluminum plasmas and liquids,* Physical Review E **66**, 025401 (2002).

[48] N. R. Shaffer and C. E. Starrett, *Model of electron transport in dense plasmas spanning temperature regimes,* Physical Review E **101**, 053204 (2020).

[49] G. Röpke, M. Schörner, R. Redmer, and M. Bethkenhagen, *Virial expansion of the electrical conductivity of hydrogen plasmas,* Physical Review E **104**, 045204 (2021).

[50] P. B. Johnson and R. W. Christy, *Optical Constant of the Nobel Metals,* Physical Review B **6**, 4370 (1972).

[51] R. L. Olmon, B. Slovick, T. W. Johnson, D. Shelton, S.-H. Oh, G. D. Boreman, and M. B. Raschke, *Optical dielectric function of gold,* Physical Review B **86**, 235147 (2012).

[52] E. D. Palik, *Handbook of Optical Constants of Solids*, Academic Press handbook series, Vol. 3 (Elsevier Science, 1998).

[53] D. Gall, *Electron mean free path in elemental metals,* Journal of Applied Physics **119**, 1 (2016).

[54] D. R. Lide, *CRC handbook of chemistry and physics*, Vol. 85 (CRC press, 2004).

[55] E. Silaeva, L. Saddier, and J.-P. Colombier, *Drude-Lorentz Model for Optical Properties of Photoexcited Transition Metals under Electron-Phonon Nonequilibrium,* Applied Sciences **11**, 9902 (2021).

[56] M. J. Kearsley, L. P. Pitaevskii, E. M. Lifshitz, and J. B. Sykes, *Electrodynamics of continuous media*, Vol. 8 (elsevier, 2013).

[57] M. Pozzo, M. P. Desjarlais, and D. Alfè, *Electrical and thermal conductivity of liquid sodium from first-principles calculations,* Physical Review B **84**, 054203 (2011).

[58] K. P. Migdal, D. K. Il'nitsky, Y. V. Petrov, and N. A. Inogamov, *Equations of state, energy transport and two-temperature hydrodynamic simulations for femtosecond laser irradiated copper and gold,* Journal of Physics: Conference Series **653**, 012086 (2015).

[59] R. W. Schoenlein, W. Z. Lin, J. G. Fujimoto, and G. L. Eesley, *Femtosecond studies of nonequilibrium electronic processes in metals,* Physical Review Letters **58**, 1680 (1987).

[60] C.-K. Sun, F. Vallée, L. H. Acioli, E. P. Ippen, and J. G. Fujimoto, *Femtosecond-tunable measurement of electron thermalization in gold,* Physical Review B **50**, 15337 (1994).

[61] N. Medvedev and I. Milov, *Electron-phonon coupling in metals at high electronic temperatures,* Physical Review B **102**, 064302 (2020).

Summary

The work presented in this thesis focuses on deepening and expanding our understanding of the physics behind the interaction of light with metals on ultrashort timescales. It specifically covers the region of moderate radiation intensities, where matter experiences pronounced excitation and eventual heating but does not undergo phase transitions or severe damage. On the experimental side, pump-probe measurements of ultrafast heating dynamics in ruthenium (Ru) thin films are conducted, combined with in-depth analysis of the exposed Ru surface. Meanwhile, on the theoretical side, significant effort has been devoted to understanding the separate processes that occur following ultrafast light absorption by transition metals. These processes include the dielectric response of hot conduction band electrons and the coupling of electrons to lattice vibrations. These insights are crucial for comprehending the observable heating dynamics within the two-temperature framework.

The study of heating in Ru thin films induced by femtosecond near-infrared laser irradiation serves as a cornerstone of this thesis. The time-domain thermoreflectance technique is employed to trace the transient evolution of electron and lattice temperatures, depending on the laser fluence. Surprisingly, the recorded temporal thermoreflectance profiles contradict our expectations, making it challenging to resolve the separate stages of two-temperature relaxation in Ru. Consequently, the rest of this thesis is dedicated to unraveling the mysteries of ultrafast dynamics in Ru using various theoretical approaches. Additionally, extensive post-mortem analysis of surface modifications in Ru provides insights into degradation processes occurring under multi-shot, low-intensity irradiation below the melting threshold. This thesis reveals that the primary degradation process in this regime is heat-induced film cracking. Unfortunately, this significantly limits the operational conditions for potential applications of Ru thin films in short-wavelength optics and semiconductor industry. However, the proposed mechanism for crack generation still requires comprehensive theoretical and experimental confirmation.

The investigation of the electron-phonon coupling mechanism in laser-excited transition metals constitutes a significant part of this thesis. A tight relationship between the strength of electron-phonon coupling and the transient dynamics pathways has been established, suggesting that any peculiarities in the thermoreflectance signal must be attributed to a specific form of electron-phonon coupling, which varies as a function of electron and lattice temperatures. To derive this form for a particular metal, extensive first-principles simulations are employed based on the principles of Boltzmann transport theory and density functional perturbation theory. Notably, the importance of coupling different electron states with phonons – an effect that is often neglected – is highlighted. Our findings reveal that accounting for this effect changes coupling values by up to a factor of two, depending on temperature, for the considered transition metals. The first key component for understanding ultrafast heat dynamics in Ru – fine electron-phonon coupling

parameterization – has been derived.

When, with an obtained in-depth understanding of electron-phonon relaxation, the limitations of previous simulation methods were revealed, the study shifted to the problem of the optical response of excited matter, which, in turn, defines the observable thermoreflectance. The scattering of conduction band electrons is a key mechanism explaining the behavior of optical properties of metals in the near-infrared regime. While electron-phonon scattering dominates in the low-temperature limit, electron-electron scattering becomes more pronounced as the temperature rises. Therefore, both channels should be taken into account when studying fluence-dependent heating dynamics in metals. By employing methods of density functional theory, the optical properties of Ru were obtained over a broad range of temperatures and photon energies. In this way, the second key ingredient was derived.

With electron-phonon coupling and optical properties at hand, it finally became possible to test the extent to which the measured heating dynamics in Ru aligns with the two-temperature framework. Theoretical optical reflectance suggested the presence of a narrow peak in the experimental thermoreflectance curve associated with ultrafast electron thermalization, yet this peak was not observed. Addressing this contradiction, exceptionally fast electron-lattice equilibration in Ru was assumed, stemming from a significant electron-phonon coupling parameter. Under this assumption, the experimental thermoreflectance dynamics could be reproduced by considering only the lattice temperature dynamics and equilibrium-temperature-dependent optical properties. Consequently, the mystery of ultrafast heating dynamics in Ru was unraveled: the experiment captures the lattice response but misses the process of electron heating and two-temperature relaxation. However, further research is needed to understand why the two-temperature picture in Ru is absent and whether it truly is missing.

Samenvatting

Het werk dat in dit proefschrift wordt gepresenteerd richt zich op het verdiepen en uitbreiden van ons begrip van de natuurkunde achter de interactie van licht met metalen op ultrakorte tijdschalen. Het behandelt specifiek het gebied van gematigde stralingsintensiteiten, waar materie een geprononceerde excitatie en uiteindelijk verwarming ondergaat, maar geen faseovergangen of ernstige schade ondergaat. Aan de experimentele kant worden pomp-probe metingen van ultra-snelle verwarmingsdynamica in dunne ruthenium (Ru) films uitgevoerd, gecombineerd met een diepgaande analyse van het blootgestelde Ru-oppervlak. Ondertussen is aan de theoretische kant veel moeite gedaan om de afzonderlijke processen te begrijpen die optreden na ultra-snelle lichtabsorptie door overgangsmetalen. Deze processen omvatten de diëlektrische respons van hete geleidingsbandelektronen en de koppeling van elektronen aan roostertrillingen. Deze inzichten zijn cruciaal voor het begrijpen van de waarneembare verwarmingsdynamica binnen het tweetemperatuurkader.

De studie van verwarming in Ru dunne films geïnduceerd door femtoseconde nabij-infrarode laserbestraling dient als een hoeksteen van dit proefschrift. De tijd-domein thermoreflectietechniek wordt gebruikt om de vergankelijke evolutie van elektronen- en roostertemperaturen te traceren, afhankelijk van de laserflux. Verrassend genoeg spreken de opgenomen tijdelijke thermoreflectieprofielen onze verwachtingen tegen, waardoor het moeilijk is om de afzonderlijke stadia van tweetemperatuurontspanning in Ru op te lossen. Daarom is de rest van dit proefschrift gewijd aan het ontrafelen van de mysteries van ultra-snelle dynamica in Ru met behulp van verschillende theoretische benaderingen. Daarnaast biedt uitgebreide post-mortem analyse van oppervlakteveranderingen in Ru inzicht in degradatieprocessen die optreden onder multi-shot, lage-intensiteit bestraling onder de smeltgrens. Dit proefschrift onthult dat het primaire degradatieproces in dit regime warmtegeïnduceerde filmbarsting is. Helaas beperkt dit de operationele omstandigheden aanzienlijk voor potentiële toepassingen van Ru dunne films in kortegolfoptica en halfgeleiderindustrie. Echter, het voorgestelde mechanisme voor scheurvorming vereist nog steeds uitgebreide theoretische en experimentele bevestiging.

Het onderzoek naar het elektron-fonon koppelingsmechanisme in lasergeëxciteerde overgangsmetalen vormt een significant deel van dit proefschrift. Er is een nauwe relatie vastgesteld tussen de sterkte van de elektron-fonon koppeling en de vergankelijke dynamicapaden, wat suggereert dat eventuele eigenaardigheden in het thermoreflectiesignaal moeten worden toegeschreven aan een specifieke vorm van elektron-fonon koppeling, die varieert als een functie van elektronen- en roostertemperaturen. Om deze vorm voor een bepaald metaal af te leiden, worden uitgebreide eerste-principes simulaties gebruikt op basis van de principes van Boltzmanns transporttheorie en dichtheidsfunctionaalverstoringstheorie. Opmerkelijk is het belang van het koppelen van verschillende elektronenstaten met fononen - een effect dat vaak wordt verwaarloosd - benadrukt. Onze bevindingen onthullen

dat door rekening te houden met dit effect de koppelingswaarden veranderen met maximaal een factor twee voor de beschouwde overgangsmetalen, afhankelijk van de temperatuur. Het eerste sleutelcomponent voor het begrijpen van ultra-snelle warmtedynamica in Ru - fijne elektron-fonon koppeling parametrisatie - is afgeleid.

Toen, met behulp van een verkregen diepgaand begrip van elektron-fonon ontspanning de beperkingen van eerdere simulatiemethoden werden onthuld, verschoof de studie naar het probleem van de optische respons van geëxiteerde materie, die op zijn beurt de waarneembare thermoreflectie definieert. De verstrooiing van geleidingsbandelektronen is een sleutelmechanisme dat het gedrag van optische eigenschappen van metalen in het nabij-infrarode regime verklaart. Terwijl elektron-fononverstrooiing domineert in de lage temperatuurlimiet, wordt elektron-elektronverstrooiing meer uitgesproken naarmate de temperatuur stijgt. Daarom moeten beide kanalen in beschouwing worden genomen bij het bestuderen van fluxafhankelijke verwarmingsdynamica in metalen. Door methoden van dichtheidsfunctionaaltheorie te gebruiken, werden de optische eigenschappen van Ru verkregen over een breed bereik van temperaturen en fotonenergieën. Op deze manier werd het tweede sleutelingrediënt afgeleid.

Met elektron-fonon koppeling en de optische eigenschappen bij de hand werd het eindelijk mogelijk om te testen in hoeverre de gemeten verwarmingsdynamica in Ru overeenkomt met het tweetemperatuurkader. Theoretische optische reflectie suggereerde de aanwezigheid van een smalle piek in de experimentele thermoreflectiecurve geassocieerd met ultra-snelle elektron thermalisatie, maar deze piek werd niet waargenomen. Om deze tegenspraak aan te pakken, werd uitzonderlijk snelle elektronroosterequilibratie in Ru aangenomen, voortkomend uit een significante elektron-fonon koppelingsparameter. Onder deze aanname kon de experimentele thermoreflectiedynamica worden gereproduceerd door alleen de roostertemperatuurdynamica en evenwichtstemperatuur-afhankelijke optische eigenschappen te overwegen. Bijgevolg werd het mysterie van ultra-snelle verwarmingsdynamica in Ru ontrafeld: het experiment legt de roosterrespons vast maar mist het proces van elektronverwarming en tweetemperatuurontspanning. Echter, verder onderzoek is nodig om te begrijpen waarom het tweetemperatuurbeeld in Ru afwezig is en of het echt ontbreekt.

Valorization and Outlook

Ultrafast high-intensity laser technology is a vital component of contemporary high-tech production, influencing various aspects of life. It plays a crucial role in advanced manufacturing processes such as metallurgy and 3D printing, as well as in surface nanostructuring and nanoscale metrology for the semiconductor industry. Additionally, laser technology enables efficient and precise ophthalmological surgeries.

Yet, the comprehensive understanding of the mechanisms behind the interaction of ultrashort light pulses with matter has not been fully established. Practically, applications of high-power laser sources demand knowledge of light-induced surface modifications pathways, which is essential for establishing a simulation framework with predictive capabilities, crucial for the advancement of laser-based manufacturing technology, and for defining operational boundaries for optical elements of laser sources. On the fundamental side, it is not always clear which (often nonequilibrium) processes play a major role in observable dynamics or what the properties of a studied material are under extreme excitation conditions. This thesis sheds light on both sides of the problem in a truly ultrafast fashion, partially revealing these mechanisms while simultaneously outlining new directions for future research.

The problem of heating and temperature evolution in ultrafast light-matter interaction experiments is usually treated on the basis of TTM or its extensions. While TTM itself is well theoretically established and repeatedly experimentally proven, there is a lack of a direct connection between theoretically studied temperature dynamics and experimentally measured quantities. To the best of the author's knowledge, neither of the existing pump-probe techniques is able to resolve electron and lattice temperatures separately and provide comprehensive information about the material's heating. Any interpretation of such experiments heavily relies on the quality of thermal parameters entering Eq. (1.1) or the quality of model fitting. This work addresses the former challenge by providing recipes for the accurate simulation of temperature-dependent thermal and optical properties of transition metals via state-of-the-art first-principles approaches. In particular, the optical properties of ruthenium presented in this thesis for the first time helped us unravel that its optical response to femtosecond irradiation almost immediately becomes equilibrium due to exceptionally high electron-phonon coupling strength. Although this important finding makes our life easier by rendering the two-temperature description of ruthenium redundant, it remains unclear whether a one-temperature response is observed in other transition metals with similar electron properties. This finding also poses a new and very interesting question about the electron-phonon coupling mechanisms beyond the instantaneous electron thermalization approximation.

Reflecting on the questions raised in the previous paragraphs, at least three independent directions for future research are anticipated. The continuation of optics lifetime studies is straightforward in terms of practical realization and highly relevant in terms of industrial applications. Acquiring knowledge of a specific degrada-

tion mechanism under certain exposure conditions for different materials will enable the tailoring of parts of thin film devices that are sensitive to irradiation.

The second intriguing direction is the extension of theoretical studies of ultrafast processes beyond the two-temperature framework. This extension could be achieved on the relatively simple grounds of the Boltzmann transport equation combined with first-principles electron-phonon scattering [1], or by exploiting the full complexity and power of time-dependent density functional theory. Another promising but still quite exotic approach in the high-energy physics community is nonadiabatic Bohmian dynamics [2] , which allows treating coupled quantum electron-ion systems containing up to several thousand particles.

However, without direct simultaneous measurements of ultrafast electron and lattice dynamics in any system of interest, these beyond-TTM simulations are nothing more than using a sledgehammer to crack a nut. While it is stated above that such experiments have never been performed so far, it does not mean that they are virtually impossible to carry out. Lattice dynamics can be accessed via the ultrafast diffraction technique. Uncoupled electron dynamics might be accessed with time-resolved measurements of the dynamic structure factor [3] via X-ray Thomson scattering or via electron energy loss spectroscopy. If one were able to combine these techniques in one experiment, it would finally be possible to make the dream of high-energy density scientists come true. In the near future, such a sophisticated experiment is expected to be the scope of a proposal for an X-ray free electron laser (X-ray FEL) facility, but with the advent of tabletop FELs and compact femtosecond electron sources, it is believed to eventually become a widely accessible in-lab technique.

References

[1] M. Düvel, M. Merboldt, J. P. Bange, H. Strauch, M. Stellbrink, K. Pierz, H. W. Schumacher, D. Momeni, D. Steil, G. S. M. Jansen, S. Steil, D. Novko, S. Mathias, and M. Reutzel, *Far-from-equilibrium electron–phonon interactions in optically excited graphene,* Nano Letters **22**, 4897 (2022).

[2] B. Larder, D. O. Gericke, S. Richardson, P. Mabey, T. G. White, and G. Gregori, *Fast nonadiabatic dynamics of many-body quantum systems,* Science Advances **5** (2019), 10.1126/sciadv.aaw1634.

[3] J. Vorberger, T. R. Preston, N. Medvedev, M. P. Böhme, Z. A. Moldabekov, D. Kraus, and T. Dornheim, *Revealing non-equilibrium and relaxation in laser heated matter,* Physics Letters A **499**, 129362 (2024).

Acknowledgments

Firstly, I would like to thank Fred Bijkerk for the brave decision of taking me, a shy and barely speaking English student, to pursue a PhD in the XUV Optics group. I am very grateful to my promotor, Marcelo Ackermann, for giving me so much freedom in choosing the direction of research. Thank you for the encouragement in rough times, for your wise guidance in work- and career-related questions, and for being by my side in any situation. My huge thanks to my daily supervisors, Igor Makhotkin and Igor Milov. Due to your gentle and very personal supervision, I feel I turned into a confident and well-rounded scientist. I also acknowledge the support and valuable discussions with the rest of the XUV seniors, and especially to Marko Sturm for invaluable help with the experimental characterization of Ru films. Carin Krijnen, you are the true wizard channeling your magic for better processing of the group. I could not imagine my PhD project working out without you.

I would like to extend my thanks to the people who took on the responsibility of additional supervision during various moments of my PhD: Nikita Medvedev, Vasiliy Zhakhovskiy, and Jan Vorberger. Nikita, your deep expertise in radiation-matter interaction, your readiness to teach and help at any time, and your involvement in my research are things I am grateful for. Vasiliy, I feel like I missed many opportunities to learn from you, but our (unfortunately not so frequent!) discussions let me look at my research from a completely different angle. Jan, I'm so thankful to you for allowing me to be your intern at HZDR in Dresden. Your supervision during that time and beyond is something I will always remember with gratitude. Thank you for countless scientific discussions which made me recall that I am kind of a theoretician myself, and thank you for introducing me to German pie culture. Special thanks to Tobias Dornheim for your benevolent attitude towards my interference in your discussions with Jan.

I acknowledge the team of experimental scientists at Radboud University: Sergey Semin, Fabio Formisano, and Alexey Kimel. Without your willingness to design and carry out, your patience to improve and repeat pump-probe measurements, my PhD project would be missing its central and most important part. I also thank Vina Faramarzi for the project management from the ASML side and for your continuous interest in my research.

I owe a huge thanks to my first scientific supervisor, Alexander E. Volkov. Thank you for taking me under your wing, for supporting my scientific curiosity, and for lessons in fearlessness. Your guidance has led me to the path of pursuing a PhD at XUV. Also, I thank everyone on Volkov's team – Nikita Medvedev, Ruslan Rymzhanov, Sergey Gorbunov, Roman Voronkov, Pavel Babaev, and Danil Zainutdinov – it was a pleasure to collaborate with you and learn from you.

I would like to express infinite gratitude to my teachers from the Theoretical Physics department at MEPhI. You made me fall in love with theory, and this love has become a beacon of hope in the grimmest moments of my PhD. Most notably,

I thank Valeriy P. Yakovlev for showing me the beauty of quantum mechanics, for your patience and kindness; Dmitriy B. Rogozkin for many-body physics, for your ironic way of giving lectures, and for your unique approach to teaching that helped me develop my scientific independence.

During these four years at XUV, I've met many nice students and postdocs who made my daily life brighter and better. Parikshit, thank you for all the care you and Jainishka wrapped around me. I enjoyed our long talks and walks, and I hope we will have even more in the future. Igor, Cris, Airat, and Roma – thank you for our crazy cooking and mixing experiments during board game sessions. Arseniy, I am grateful for our everyday refreshing walks, which reminded me of my undergraduate era. My only regret is that you have not been around since the very start of my PhD. Ksenya, Adele, Ertug – our occasional cinema evenings made me feel at home in Twente.

I could not imagine having better officemates than Harm, Ilias, and Dmytro. Harm, I have always admired your dedication to routine work and your good judgment of things. Thank you for all the support you have shown me. Ilias, I feel sorry that I could not fully share your passion for Radiohead. I promise I will become their true fan eventually. Dmytro, thank you for your endless optimism and readiness to help in any matter that have made our office kinder and better.

I would not be the person I am now without my beloved school friends Sergey, Sadyk, and Sasha. We have known each other for more than 20 years, and it is a true miracle that I can still write to you at any time about anything, and you will immediately respond and help. To my university friends Vlad, Pasha, and Vanya – just thank you for what has been (so far) the best part of my life. Without you, I would not be the person I am now, nor would I be a scientist. Pasha, a huge shoutout to you for your continuous interest in my PhD and for your encyclopedic knowledge in every field of physics, which I could always rely on. I am also thankful to my dear Discord friends Anton, Gleb, and others who have preserved my sanity by playing and meming with me over these years.

I want to conclude with the main people in my life. My parents, Marina, Oleg and uncle Zhenya, as well as my brothers Borya and Yasha, thank you for your love, which I could feel despite the thousands of kilometers physically separating us. Thank you for being not just my family but also my loyal friends who trust in me far more than I trust in myself. Lina, my beloved wife, thank you for sharing every second of this journey with me. I cannot find enough words to express my appreciation for everything you have done for me; without your belief in me, none of this story would have been possible.